THE UNIVERSITY OF CHICAGO

CONTROLLED CHARGE TRANSPORT IN SINGLE-MOLECULE ELECTRONICS

A DISSERTATION SUBMITTED TO

THE FACULTY OF THE DIVISION OF THE PHYSICAL SCIENCES

IN CANDIDACY FOR THE DEGREE OF

DOCTOR OF PHILOSOPHY

DEPARTMENT OF CHEMISTRY

BY

WAI-YIP LO

CHICAGO, ILLINOIS

DECEMBER 2016

TABLE OF CONTENTS

LIST OF TABLES

LIST OF SCHEMES

LIST OF FIGURES

ACKNOWLEDGEMENT

I would like to thank Prof. Luping Yu for giving me the opportunity to work in his group. The advices he gave during my PhD career have been most valuable and have allowed me to overcome the difficulties encountered in my research. If there is one thing to take away from all his teachings, it would be to always look beyond the surface of an issue and think critically about it. It has been an honor working under Prof. Yu for my PhD degree.

I would also like to thank Prof. Michael Hopkins and Prof. Yossi Weizmann for agreeing to serve on my dissertation committee.

I want to thank the past and present Yu group members for their help in my research, in particular Dr. Lianwei Li, Dr. Zhengxu Cai, and Dr. Na Zhang for offering their advices and working with me on various projects. Thank you to my lab mates Alex, Donglin, Valerii, and Andriy. It has been a pleasure working with you all.

Also thank you to Dr. Qiti Guo and Dr. Justin Jureller for their help with various equipment and measurements.

Finally, I would like to thank my family for their unrelenting care and support. It would not be possible for me to complete this degree without them.

CHAPTER 1

INTRODUCTION

The famous "Moore's law" states that the density of transistor in an integrated circuit board would double about every two years. This trend has been religiously followed by the semiconductor industry for 50 years. As of this writing, Intel is working on processors with feature size of 14 nm.[1] Research in the 10 nm regime proves to be challenging due to quantum tunneling effect. As the size of the transistor unit decrease, we would ultimately reach the atomic limitation of the top-down approach.

The semiconductor industry has been relying on the top-down approach to fabricate electronic components in microprocessors, in which photolithography is used to develop circuits. However, the resolution of an image is limited by the wavelength of light being used, which determines the minimum feature size possible in the photoresist pattern. As a result, it will be a challenge to sustain the continuous shrinking of feature size in order to meet the expectations of the Moore's law. In addition, even when the small sizes can be achieved via innovative approaches, the control of current flow becomes more difficult due to quantum tunneling effect in the nano regime. Leakage occurs between the gate and the semiconductor channel when the dielectric layer is as thick as a few atomic layers, impairing the reliability of transistors. Both physical and economic reasons stimulated people to search for alternatives to traditional semiconductor fabrication.

Molecular electronics offer potential as an alternative approach by applying the smallest building units - single molecules as electronic components and thus allow the construction of electrical

circuits with stable structures at the molecular level. The control of electronic information by manipulation of charge transport through single molecules is important for both fundamental understanding of the charge-transfer mechanisms and the potential applications in single-molecule devices. Mulliken and Szent-Gyorgyi first introduced the concept of charge transfer in "donor-acceptor" complexes,[2, 3] which became the basis of molecular electronics. Mann and Kuhn demonstrated metal-molecule-metal junction with fatty acid Cd salts monolayer.[4] With the concept of molecular junction established, Aviram and Ratner (AR) showed theoretically that rectification effect is possible with donor acceptor systems.[5] Subsequently through experiments, Geddes et al. and other groups reported the asymmetric current-voltage characteristics with a device fabricated of Langmuir-Blodgett (LB) monolayer consist of donor-σ-acceptor system although their true mechanism for rectification is uncertain.[6-8]

Modern molecular junctions consist of the molecular core, the anchoring groups, and the electrodes. π-Conjugated molecules are commonly used as the molecular core due to their high conductance. Anchoring groups are either chemisorbed on or covalently bonded to the electrodes, effectively bridging between the molecular core and the electrodes. In particular, thiolate is commonly used as the anchoring group due to the strong sulfur-gold interaction.[9] The electrodes are usually precious or transition metals such as gold, platinum, or nickel. Recently, carbon electrodes are developed due to the strong coupling with organic core.[10] With the advance of atomic force microscopy (AFM) and scanning tunneling microscopy (STM) systems, direct measurements of the electrical properties of single molecule junctions become possible. Currently, single molecule junction techniques mostly involve break-junction (BJ) techniques including STM-BJ, mechanically controllable break junction (MCBJ), electromigration breakdown junction, electrochemical deposition junction, and surface-diffusion-mediated deposition junctions.[10] In the

past decades, advancement in these nano-technologies facilitated major research efforts directed towards understanding charge transport through molecular wires and other components.[10] With the flexibility of organic chemistry and the advancements of various cross-coupling reactions, molecular electronic components with various structures and functions can be achieved.

1.1 Development in Single-Molecule Electronics

Here I will give a brief introduction to the study of the structure-property relationship for the anchoring groups and the molecule core.

1.1.1 Anchoring Group

The anchoring groups connect the molecule core to the electrode in order to form a complete molecular junction. The mechanical stability and the electronic coupling strength with the electrodes are important properties to be considered when designing molecular electronics. Common anchoring groups include thiol,[11] thiol ether,[12] amine,[13] pyridine,[14] selenide,[12] cyanide,[15] isocyanide,[13] nitro,[16] carboxyl acid,[17] phosphide,[12] and π-donors such as fullerene and pyrene.[18, 19]

Thiol groups are one of the most effective functional group to be utilized as the anchoring group in single-molecule junction. Their high affinity to gold allows them to form the strong Au-S bond, which is even stronger than the Au-Au bond itself. Other anchoring groups coordinate with gold through dative interaction, which involves donation of lone pairs from the functional group (Lewis base) to gold (Lewis acid). Since the electronic structure of different anchoring groups are different, their electronic coupling to gold also varies. It was shown that contact resistance increases in the order Au-S < Au-NH_2 < Au-CO_2H as the electronic couple decreases.[17] Investigations of other properties, such as junction stability and formation probability, show that thiolate group persistently performs better than most other anchoring groups.[12, 20] However the free

aromatic thiols lack the chemical inertness of groups like pyridine and cyanide, and therefore need to be preserved by protecting groups under ambient conditions.

In addition to physical junction properties, the anchoring group can have profound impact on the charge transport mechanism. The orbital mixing between the anchoring group and the molecular core can determine whether the junction is hole transport (through the highest occupied molecular orbital (HOMO)) or electron transport (through the lowest unoccupied molecular orbital (LUMO)). While this property can be determined by thermoelectric measurements and theoretical calculations, we can predict the transport carrier by evaluating the orbital overlap of the functional group with the molecular core.[21] For example, anchoring groups like thiol and amine are mostly hole transporting due to the orientation of the lone pair aligning with the π orbital of the core. On the other hand, anchoring groups such as pyridine and cyanide with lone pairs along the σ direction have poor overlap with the HOMO. The electron withdrawing nature of these functional groups also contributes to the LUMO-dominated transport. Furthermore, electron deficient functionalities in the molecular core lower the overall HOMO-LUMO levels, bringing the LUMO closer to the Fermi level of the electrode. The anchoring group will have minimal effect on determining the transport orbital in this case.[22]

Recently, direct anchoring by covalent bonding between the molecule core and the electrode has been studied.[23] A direct Au-C anchor can be generated from transmetalation of alkyl tin,[24] trimethylsilyl alkyne desilylation with fluoride,[25] and electroreduction of diazonium salt.[26] Because of the instability of the Au-C bond under ambient condition, these Au-C anchors tend to oligomerize during break-junction experiment. More research is needed in this area to widely implement covalent contacts in single-molecule junction.

1.1.2 Molecular Core

While the anchoring groups can have significant effect on the electronic properties, the structure of molecular core largely determines the function of the single-molecule junction (e.g. diode, transistor, switch). The molecular core can be a π-conjugated structure such as oligophenylenes and oligothiophene or short alkyl chains. For short molecules (i.e. <3nm), it was shown that molecular conductance decays exponentially with molecular length.[27] At this length scale, transport can occur via non-resonant tunneling; electron can tunnel through the molecule even when the energy levels are not well-aligned. This is the reason why molecules with large HOMO-LUMO gaps such as alkanes can conduct in a molecular junction. As the molecular core becomes longer, the transport mechanism can change. Studies have shown that the transport mechanism will switch from non-resonant tunneling to a "hopping" mechanism after extending the molecular core to a certain length.[28, 29] It was also shown that a disruption of conjugation in longer molecular core dramatically reduces the conductance of the junction.[30] Conformation of the molecular core can affects the molecular conductance of the junction. The twisted structure in regular oligophenylenes reduces the delocalization length, which was shown to reduce the conductance.[13] Further studies on the effect of conjugation on conductance showed that cross-conjugated molecules have lower conductance than molecules with broken conjugation. This phenomenon was attributed to the quantum interference effect which will be discussed later.

The charge transport properties of a molecular wire system can be characterized by its length dependent conductance, featured with the tunneling decay constant, β. It was observed that electron conductance decreases exponentially as a function of the molecular length, $\sigma_M \propto e^{-\beta L}$, where σ_M is the single molecule conductance and L is molecular length.[31, 32] The lower the β value,

the better the molecule is able to mediate long range charge transport. It was shown that π-conjugated molecules typically have lower β value than aliphatic σ-bond molecules. The delocalization of orbitals and the small energy gap between the highest occupied molecular orbitals (HOMO) and the lowest unoccupied molecular orbitals (LUMO) allow π-conjugated molecules to function as highly conductive wires. The Fermi energy level of the metal electrodes typically aligned within the bandgap of these molecules with small offset relative to either the HOMO or the LUMO, resulting in efficient charge injection and transport. Numerous molecules were investigated and the length dependence of their conductance can usually fit with the equation above. For example, oligothiophenes are among the most studied materials in molecular electronics due to their highly conjugated π-orbitals and efficient charge transport.[33] The effect of other structural factors, such as effects of side chains and terminal groups, on charge transport in oligothiophenes have been studied.[34-38] The conductance indeed showed exponential decay as a function of length.

Rectification is an important physical phenomenon in electronics. To reproduce the diode behavior in molecular scale, the original AR model applies a donor-σ-acceptor structure,[5] in which the non-conjugated bridging σ component behaves as an electrically insulated spacer to introduce tunneling barrier in the molecule. The AR model has led to many experimental demonstrations of molecular rectification.[6-8] Because of the nature of the STM measurements, the tip electrode and the surface electrode often consist of different metals, which would induce rectifying effect due to the difference in the Fermi energy level. To confirm the rectification is originated from the molecular core, a study of a conjugated molecule with planarity controlled by protonation/deprotonation showed strong rectification effect when the molecular core is twisted

and weak to no rectification when that is planar.[39] The Yu group also extensively studied molecular rectification, which will be covered in details in a later section.

Apart from diodes, switches are an important functionality in an electronic circuit. Molecules that can switch between two or more conductance states via an external stimulant such as light, heat, or pH have been searched. Stable isomers with conformation changes can induced difference in conductance due to the difference in spatial arrangement of the atoms and/or change in electronic structure. The energy barrier between the two conformations needs to be high enough so that switching can be controlled. For example, a molecular switch based on the bianthrone structure exhibits the switching barrier between the two isomers on the order of 120 meV by a temperature dependent conductance study.[40] It is important to note that distance between the two electrodes should be similar between the two or more isomer states in order to ascertain that the change in conductance is originated from the molecular core and not the length dependent conductance. In addition, strong coupling between the molecule and the electrode can render the switching behavior irreversible in case of photoswitching. For example, many diarylethene molecules show irreversible switching behavior due to the strong coupling of the molecule to the electrode. However, a recent study showed that the graphene electrode coupled with an increased non-conjugated spacer length, robust reversible conductance switching can be observed in a diarylethene molecular switch.[41]

Recently, the concept of quantum interference (QI) has been the focus of research because it can be another way to introduce switching behavior in molecular electronics. This phenomenon occurs exclusively in molecular electronics with no equivalent in solid-state electronics. Study of a molecule with two parallel identical conductive pathway demonstrated constructive QI, in which

the double-backbone junction showed more than two times the conductance of the single-backbone junction.[42] QI effects can also be realized by the geometry of the transport pathway. For example, comparison between a stilbene with thiol end groups connected in para to each other and that in meta positions showed orders of magnitude difference in conductance even though the two structures contain the same molecular formula and length.[43] The cross-conjugated molecular wire mentioned previously is another example to manifest the QI effect.

1.2 The Scanning Tunneling Microscopy Break-Junction Technique

Pioneered by Tao and coworkers, the scanning tunneling microscopy break-junction technique is one of the most widely used method to produce and measure in situ single molecule junctions.[14] In this method, thousands of single molecule junctions are created successively by the repeated tapping motion of the STM tip on a flat electrode functionalized with the target molecular wires. This technique takes advantage of the ability of the piezoelectric components in the STM probe to precisely control the tip movements. In order to form a junction between the tip electrode and the substrate electrode of the STM, the target molecular wires are typically functionalized with anchoring groups that will interact strongly with the metal electrodes, and are deposited onto the substrate electrode via self-assembly. Thiol groups are commonly used for this purpose due to their strong affinity with Au as previously mentioned.

A typical measurement cycle is shown in Figure 1.1. The tip electrode is first brought close to the substrate electrode. The two electrodes may or may not be in contact depending on the current set point value. Molecules in the vicinity of the tip on the substrate can become attached to the tip at this time, bridging the two electrodes. The tip is then retracted from the substrate at a controlled

rate as the bridging molecular junctions begin to break, eventually forming a single molecule junction as the gap widen to a certain distance. During the retraction phase, the current between the tip and the substrate is monitored. Together with the distance travelled by the tip, the conductance-distance trace can provide the evidence of the formation of a single molecule junction. A typical conductance-distance trace that demonstrate a successful formation of a single molecule junction would show an exponential decay in conductance as the tip retract. This is followed by a plateau in conductance, signifying the formation of a single molecule junction. The length of the plateau will vary depending on the type of molecule being measured. As the tip continues to move away from the substrate, a sharp drop of the conductance can be observed due to the breaking of the single molecule junction. This entire cycle is repeated thousands of times in order to have a statistical assessment of the single molecule electrical properties of the molecular junction. A peak can be observed by plotting the occurrence of the conductance plateaus in a histogram, which can be used to give the most probable conductance of the molecular junction.

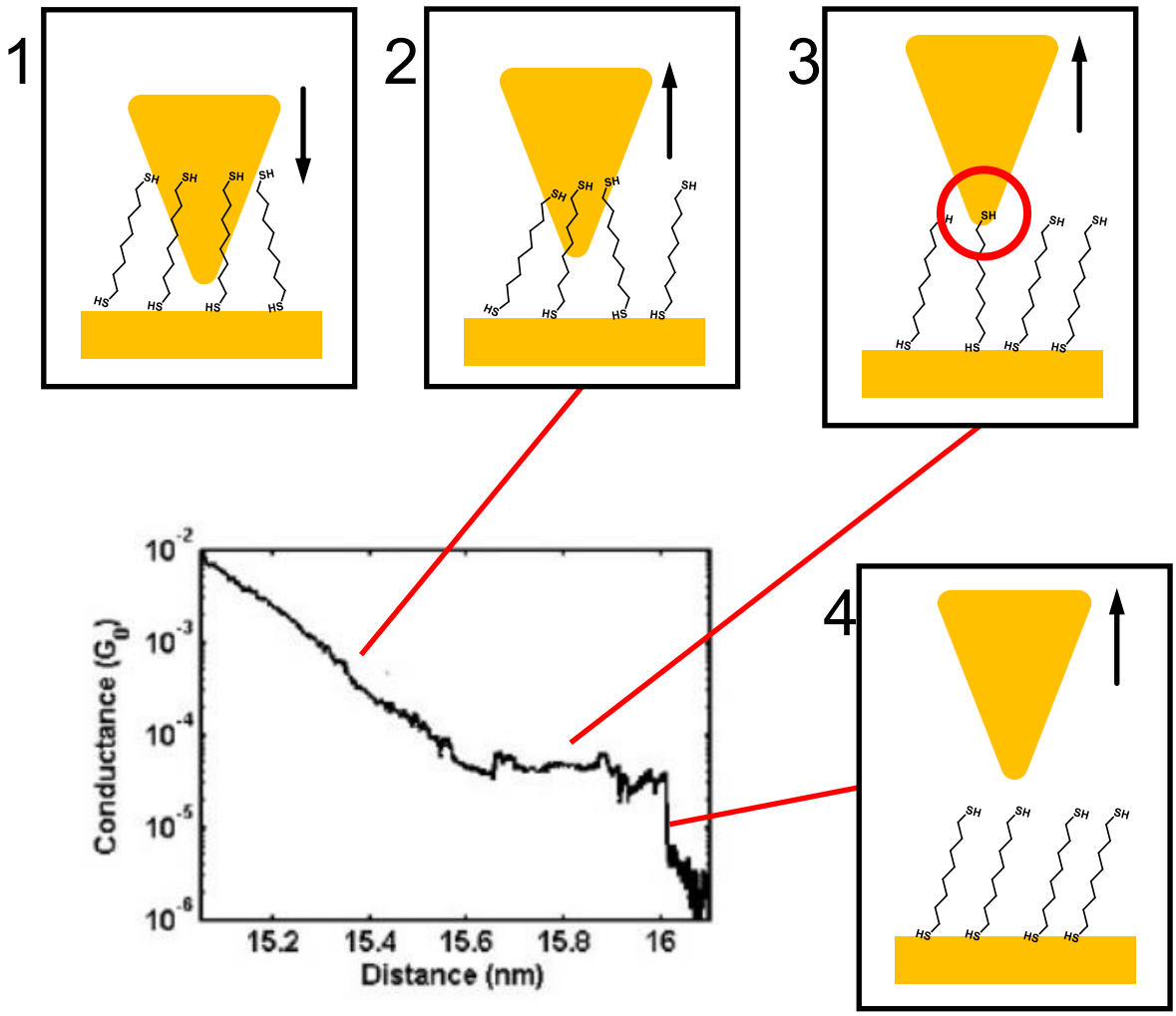

Figure 1.1 The STM break-junction tapping cycle.

1.3 Investigation of Molecular Rectifications in the Yu Group

In the following section, I will highlight the Yu group investigations on the designs and characterizations of molecular diodes and further on development of molecular switches and transistors.

1.3.1 Molecular Rectification in Diblock Oligomers

In search of a more simplistic structure for molecular rectification, we turned our attention to the p-n junction structure, which is a crucial architecture in semiconducting materials. Our initial idea came from our research effort in synthesis and characterization of conjugated blocks polymers with different conjugated blocks covalently connected for supramolecular assemblies.[44] The resulting diblock copolymers imposed challenges in investigating their electronic properties. Thus, we put this concept into designing p-n junction molecules, a diblock molecule incorporated with two conjugated blocks of opposite electronic demands.[44-48] The goal is to explore whether these molecules will behave as molecular diodes. If it works, the simplicity of the diblock architecture and the versatility in the structural variation would make this system unique and valuable in future designs of molecular-scale electronic components.

The first amphiphilic conjugated diode is composed of electron-rich semiconducting tetrathiophenes and electron-deficient tetrathiazoles. (Figure 1.2).[44, 45] To ensure the formation of monolayer assemblies, the tetrathiophene is functionalized with hydrophilic tetraethyleneglycols and tetrathiazoles with hydrophobic alkyl chains. A reference octathiophene molecular wire with the same side chain pattern was synthesized. Both **1** and **2** were assembled to a Langmuir-Blodgett (LB) monolayer at the air-water interface with the hydrophilic part adjacent to the water subphase and the hydrophobic part away from it. The LB monolayers were then transferred to glass, silicon wafer or hydrophilic gold surface under a constant pressure and studied by optical ellipsometry, UV/vis, STM and scanning tunneling spectroscopy (STS) techniques. From STM/STS studies, an asymmetric current-voltage (I-V) curve was obtained (Figure 1.2b) for **1** while a symmetrical I-V curve was observed for **2** (Figure 1.2c), confirming that the rectification originates from the asymmetric core. The rectification ratio was small at low bias but increase to 18 at 1 V. During the

measurement, the electron flowed from the tip to the thiazole group then flowed through the thiophene units to the gold substrate. Asymmetrical I-V curves were consistently obtained for asymmetrical diblock oligomers while symmetrical I-V curves were obtained for oligothiophene monolayer under different current setpoints during STM measurement. This proves that the diode effect is intrinsic to the molecular nature of the diblock oligomer.

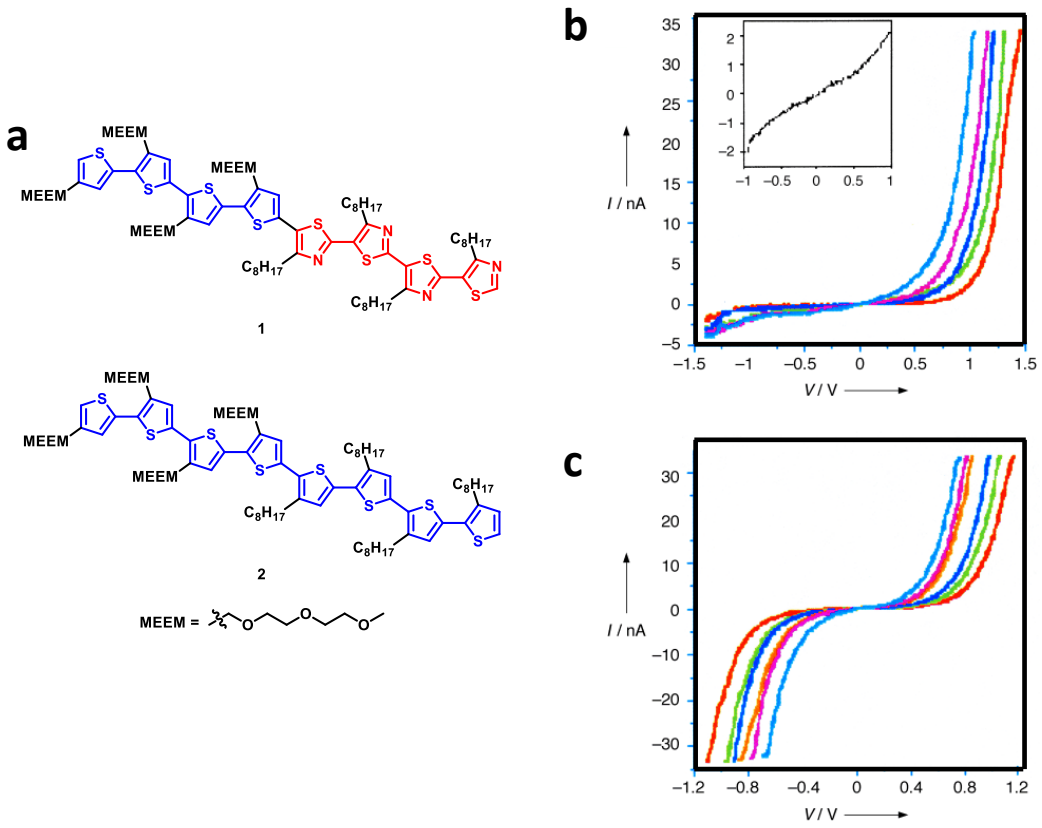

Figure 1.2 (a) Structures of amphiphilic conjugated diodes (top) and the reference oligothiophene (bottom). (b) I-V curves of 1 assembled via LB film technique showing asymmetric characteristics. (c) I-V curves of reference compound 2.[44] Colored curves represent different current setpoints (1 red, 2 green, 4 blue, 6 orange, 8 purple, and 10 pA light blue).

Although the assemblies of amphiphilic diblock co-oligomers were shown to be effective rectifier, the measurements were done on assemblies with unknown molecules connecting the

circuit. Uncertainty also exists in the junction between molecules and electrodes. To address these issues, the p-n junction molecules consisting diblock co-oligomer of bithiophene and bithiazole units terminated with dithiol groups were synthesized (Figure 1.3a). After the asymmetric molecular wire was assembled onto alkane thiolated gold surface, bright spots with 2 nm diameter can be observed on STM imaging, each contains two diode molecules (Figure 1.3b, inset). The rectification effect observed is therefore the contributions of a pair of p-n junction molecules. STS measurement showed an asymmetric I-V curve with a turn-on voltage at around 0.75 V. When a symmetrical oligothiophene was tested, a symmetric I-V curve was observed, (Figure 1.3c, inset) ruling out the possibility of rectification coming from the asymmetry of Pt/Ir tip and Au surface.

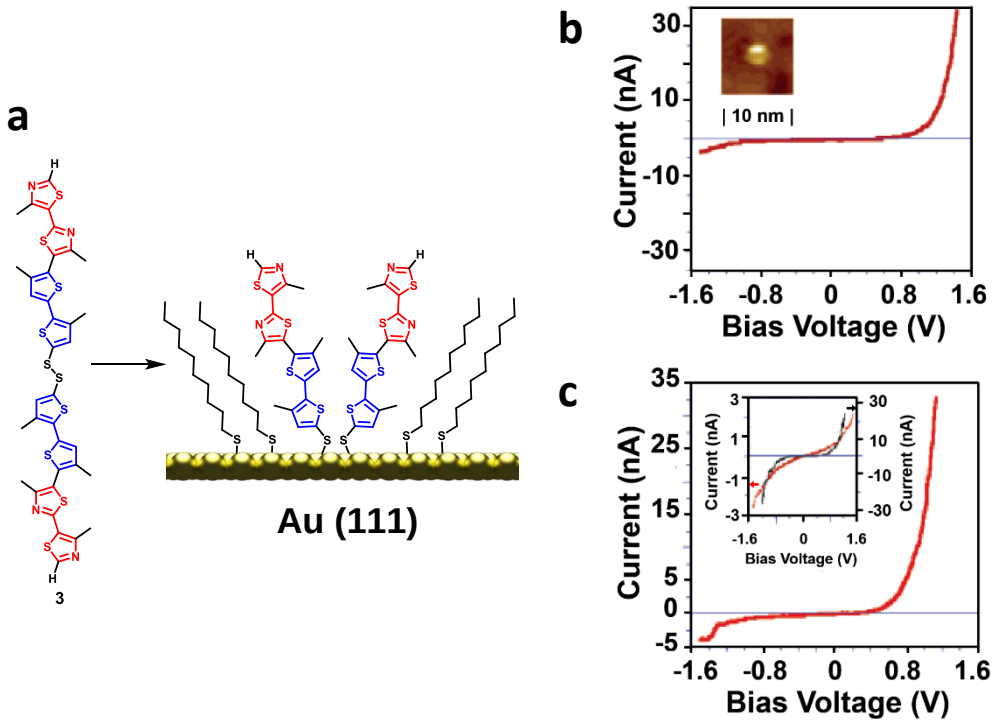

Figure 1.3 (a) Precursor structure and the co-assembly of diblock oligothiophenethiazole molecule with decanethiol on Au surface. (b) I-V curve of individual molecules deposit on Au surface (inset: STM image with the bright spot correspond to the diode molecule). (c) I-V curve of the pure monolayer of the diblock molecule (inset: I-V curves of reference molecules, tetrathiophene (black) and decanethiol (red)).[45] Adapted with permission from reference [45]. Copyright (2002) American Chemical Society.

These monothiolated diode molecules still impose challenge in measurement by using STS technique due to small contact area with STM tip. Thus, to control the orientation of single molecular rectifier and provide access to a second electrode, we prepared diblock co-oligomers with cyanoethyl (CNE) thiol and trimethylsilylethyl (TMSE) thiol end groups that can be orthogonally deprotected by using sodium ethoxide and tetrabutylammonium fluorides (TBAF), respectively, as shown in Figure 1.4.[46] To demonstrate the sequential deprotection, a molecule with a switched orientation was synthesized for comparison (Figure 1.4b). First, the CNE group was removed with sodium ethoxide in ethanol solution and the molecules were inserted in a preassembled dodacanethiol (DDT) SAM on gold substrate. A second deprotection using TBAF to remove TMSE group exposes the second thiol group, which can react with a gold nanoparticle. The self-assembly process can be monitored with STM image, which showed single molecule images with an average size of 1.8 nm, in accordance with other single molecules inserted in an alkyl thiol matrix. Au nanoparticles with apparent diameter of 9-11 nm was used to form the metal-molecule-metal junction. The formation of self-assemblies was confirmed by control experiments, grazing incidence FTIR studies. The I-V curve was measured with STS technique and shown in Figure 1.4c and d. The I-V curves showed significant asymmetry at different set current, indicating the rectification resulted from the molecular core. Switching the orientation of the diode reversed the direction of rectification. These results demonstrated that the rectification is indeed originated from the molecular p-n junction. We ascribed the rectification to the dipolar effect. Theoretical calculation indicated that the diode molecules exhibit an internal dipole moment of 2.8 D. When it was oriented in defined direction, the dipolar field will be superimposed to the external field that directs current flow.

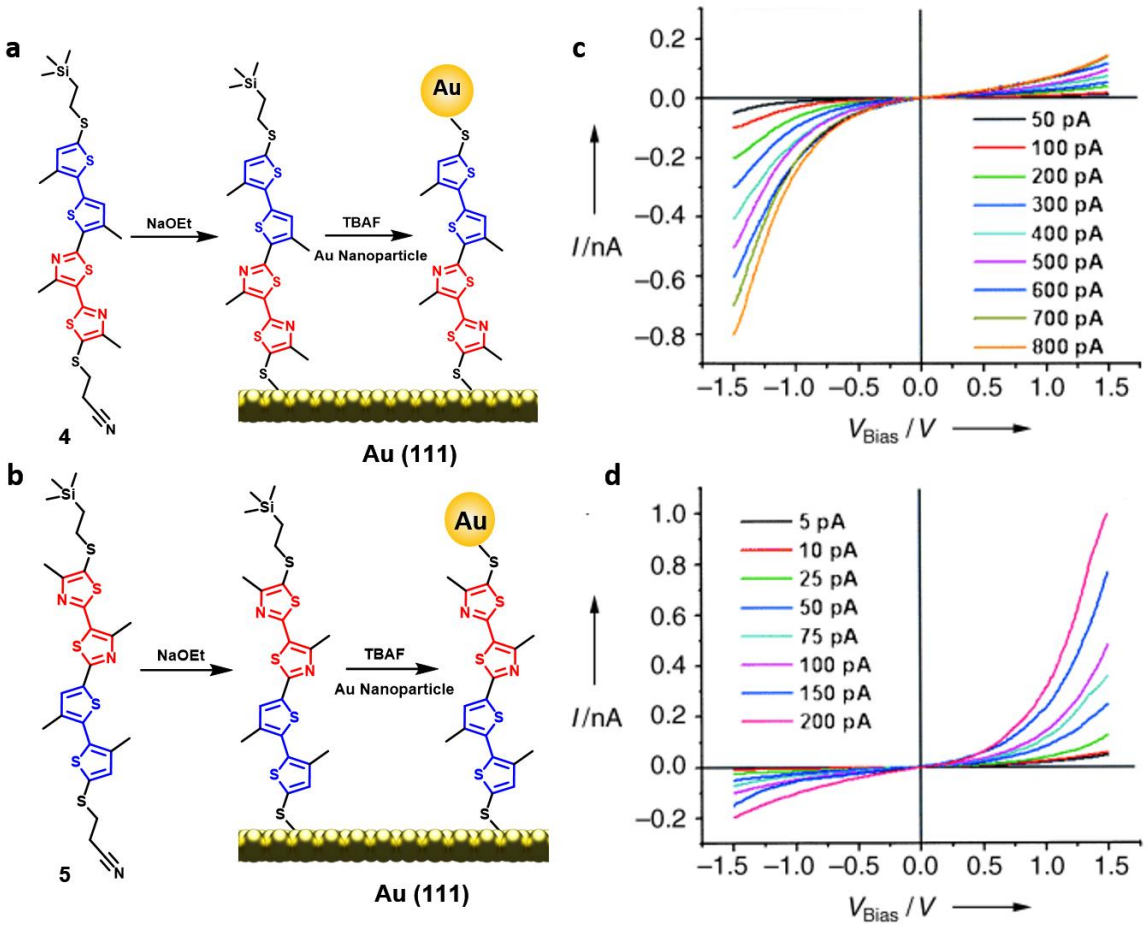

Figure 1.4 (a), (b) Structures and self-assembling monolayer of diodes molecules with orthogonal protecting groups for sequential assembly on Au surface with different orientations, and the corresponding I-V curves (c) and (d) of these molecules using Au nanoparticle as contact in the STM technique.[46]

The mechanism of rectification in this diblock system was further investigated by theoretical calculations.[49] The I-V curve of molecular diode **5** predicted by theory based on the Green's function theory of sub-barrier scattering was in qualitative agreement with the experimental results. This simple model shows that in addition to the localization of the wave function of the conducting orbital, the resonant electron transfer in the diblock system also contributes significantly to the rectifying behavior of the molecular diode.

Based on the dipolar effect, it can be hypothesized that molecules with large dipolar moment will exhibit more pronounced rectification effect. Thus, molecule **6** (Figure 1.5) was synthesized, which possesses similar protecting groups as the previous ones. The head-to-tail connected dipyrimidinyl segment is more electron-deficient and the dipole moment of the molecule is indeed 6.2D, larger than previous p-n junction molecules. Furthermore, the compound is geometrically linear, avoiding conformational uncertainty perceived in molecule systems based on five-member rings (i.e. thiophene). Applying the same procedure as before, the monolayer assembly was formed and characterized by STM and STS. The current – voltage curve showed that the molecule indeed exhibited more significant rectifying effect with rectification ratio ranging from 4.5 – 9 compared to that of the previous system, which ranges from 2-7. Interestingly, the direction of rectification can be inversed by protonation of the nitrogen atom on the pyrimidinyl group with hydrogen perchloric acid as shown in the I-V curves in Figure 1.5**Error! Reference source not found.**. The change in rectification direction can be explained qualitatively by the change in the dipolar orientation. As shown in the energy diagram presented in Figure 1.6, the dipole moment of the self-assembled monolayer created an asymmetric potential in the vacuum level of Au surface and Au nanoparticles, leading to asymmetric tunneling potential between the molecule and the two electrodes. After protonation, the dipole moment inverted and rectifying direction inverted. These results indicated that the shift of rectification direction provides access to switches responding to environmental factors.[50] The above examples also clearly demonstrate the impact of dipole moment to the charge transfer process in molecules.

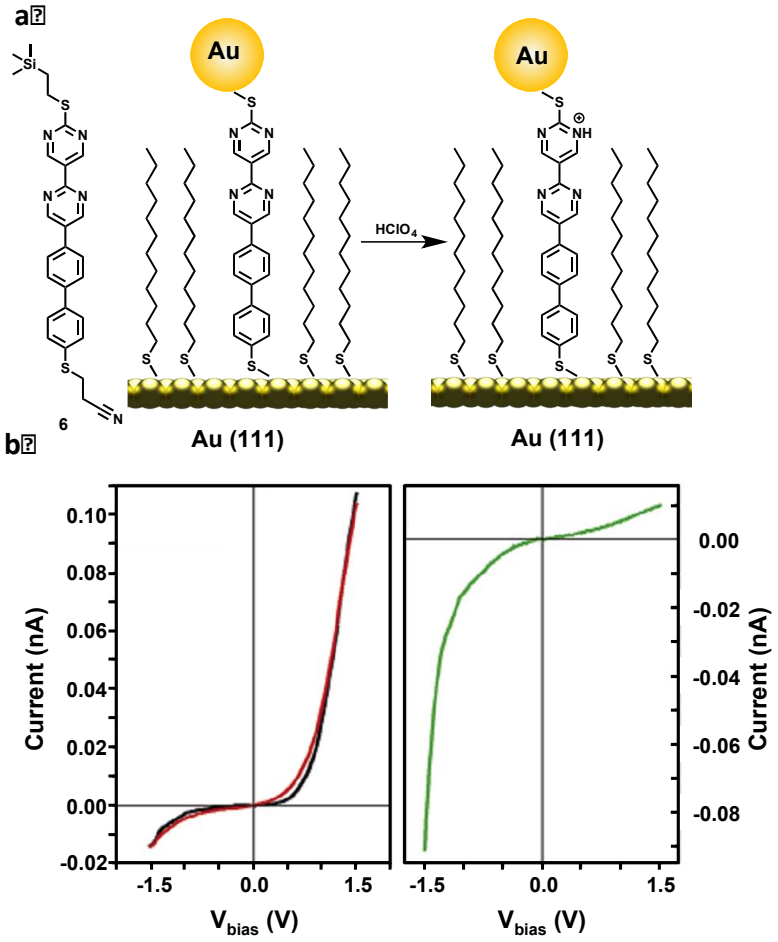

Figure 1.5 (a) Self-assembly of diblock molecular diodes and protonation by $HClO_4$. (b) I-V curves of diblock before protonation (black), after protonation (green), and after protonation-deprotonation (red), showing switchable rectifying effect by protonation. Reprinted with permission from reference [50]. Copyright 2005 American Chemical Society.

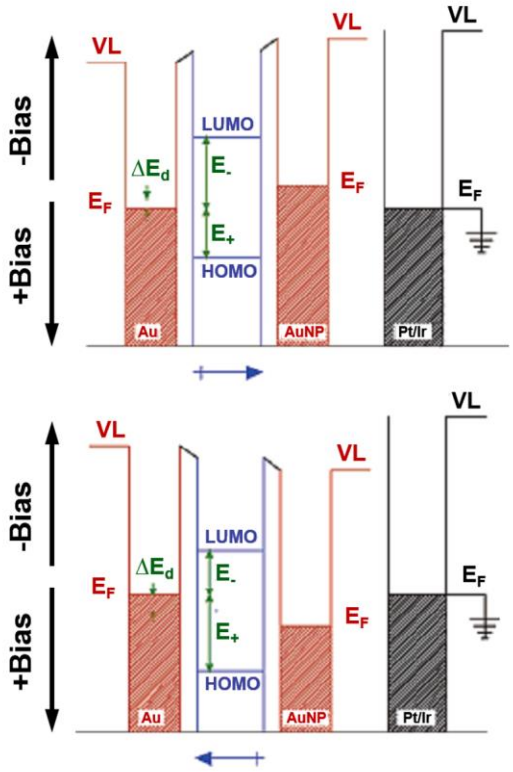

Figure 1.6 Energy diagrams for unprotonated (top) and protonated (bottom) dipyrimidinyldiphenyl assemblies. ΔE_d is the shift in local vacuum level at the interface due to the dipolar layer. $E_{+/-}$ are the energies required to align E_F with the HOMO/LUMO. Reprinted with permission from reference [50]. Copyright 2005 American Chemical Society.

All of these molecules shown above were investigated by simple STS experiments, which could be tedious and difficult to perform. Fortunately, all of our results have been reproduced with other measuring techniques. A convincing demonstration of rectification effect of a p-n junction with the STM break-junction technique was shown by our collaborative work with Tao's group.[48] Two molecular junctions, the symmetric tetraphenylene and the asymmetric dipyrimidinyldiphenylene, were studied. (Figure 1.7a) By applying the sequential deprotection processes, the diode molecules were aligned on the gold surface during self-assembly in a controlled direction. The conductance of the asymmetric molecule was observed to be three times greater than the symmetric one, even

though both molecules have similar length. While symmetric I-V curves are observed in the tetraphenyl molecule (Figure 1.7b and c), rectification effect was clearly observed in the dipyrimidinyldiphenyl diblock molecule, with higher current in the direction going from the dipyrimidinyl to the diphenyl block (Figure 1.7d and e). Measurements recorded with the non-symmetric molecules bound only to one electrode also display symmetric I-V curves, which emphasizes the importance of the molecule-electrode contact in the rectification effect.

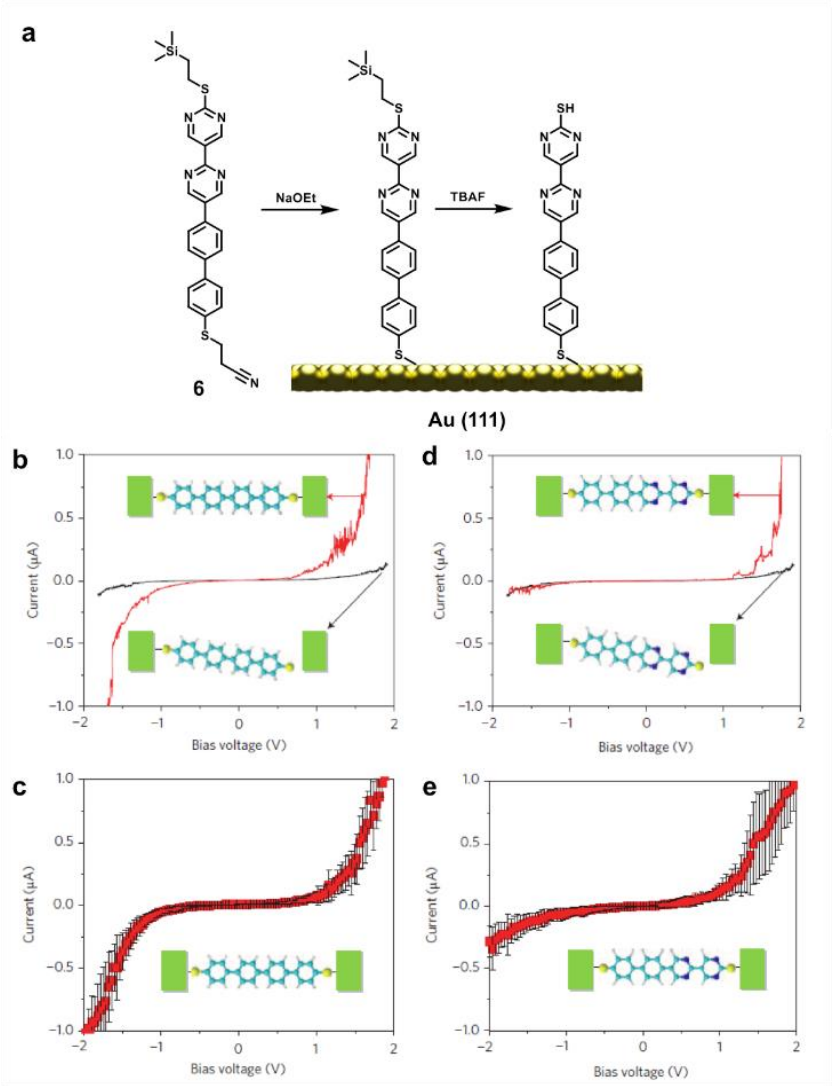

Figure 1.7 (a) Structure and self-assembly of compound 6. (b) Selected I-V curves and (c) average curve from 30 individual curves of the reference tetraphenyl molecule. (d) Selected I-V curves and (e) average curve from 50 individual curves of compound 6.[48]

The same molecules were also investigated by using the MCBJ technique in collaboration with the group in IBM Zurich lab.[36] As shown in Figure 1.8a, the histogram containing 500 opening cycles shows two distinct conductance peaks, reflecting that the two different orientations of the molecules forming the junction are of different polarization with respect to the applied bias and their dipole moments. The similar peak heights show that the two orientation are of similar probability. I-V curves measured at temperatures ranging from 300 to 50 K showed similar rectification behavior (Figure 1.8b), indicating rectification resulting from Coulomb blockade and electrical field induced level shifting. Theoretical calculations based on a single-level semiempirical model are in good agreement with the experimental data (Figure 1.8c and d).

More in-depth theoretical analysis showed that spatial asymmetry in the molecular junction is essential for the rectification behavior of the molecule.[51] The π-type HOMO is localized on the biphenyl group while the HOMO-1 and the HOMO-2 are localized on the dipyrimidinyl unit. The weak orbital overlap between the two units results in electronic structure similar to a p-n junction. In addition, a length induced inversion of rectification was observed theoretically in this pyrimidinyl/phenyl diblock system.[52] Using *ab initio* theory and the nonequilibrium Green's function theory, a series of increasing length diblock molecular junctions were modeled. The direction of the rectification was predicted to depend on the molecular length, with a critical length of 3 pyrimidinyl and 3 phenyl units long (27.735Å). The length-induced change of the LUMO energy level leads to a change of energy alignment with the electrode Fermi level. The LUMO energy level moves to the Fermi level and its wave function becomes more localized under a positive bias, while the opposites were observed when the junction is under a negative bias. The contradictory effects between the energy level alignment and orbital delocalization compete in the determination of the rectification direction.

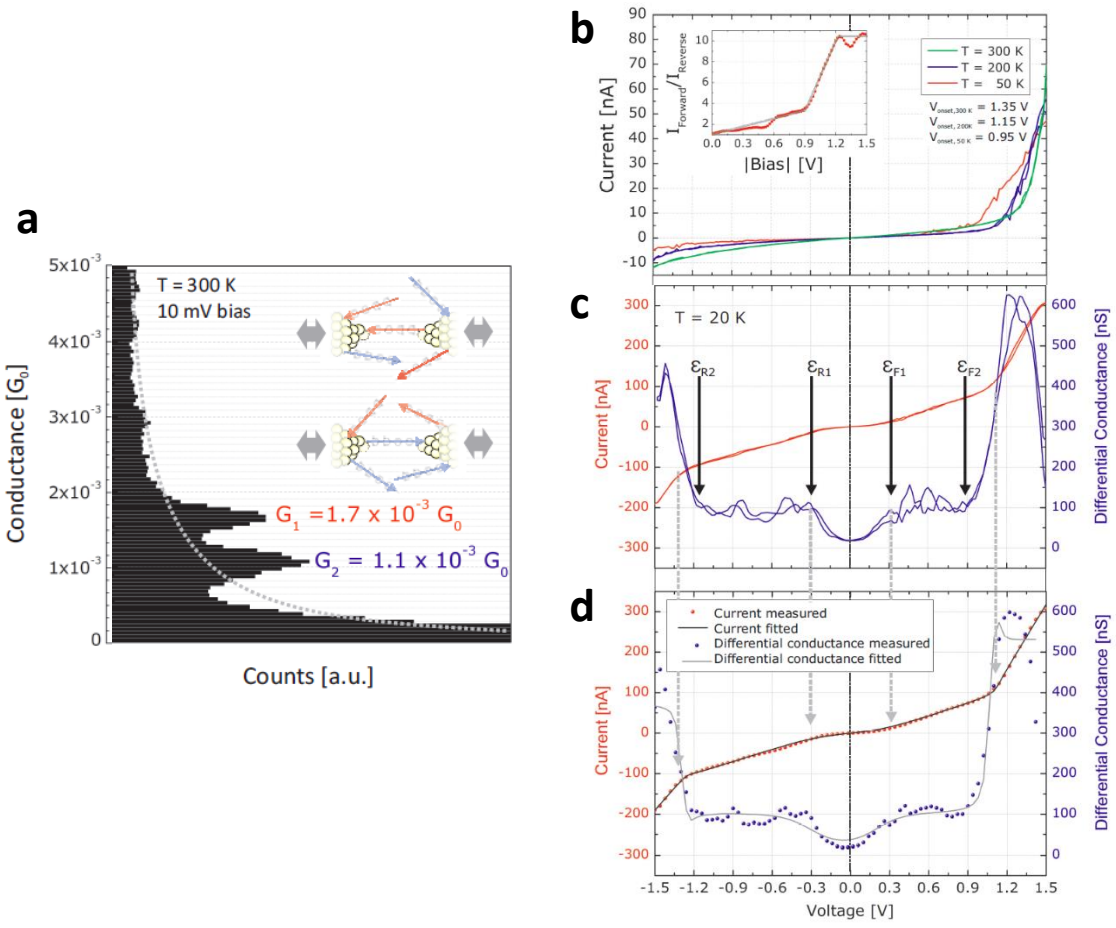

Figure 1.8 (a) Conductance histogram showing two distinct peaks for the two different orientations of compound 6. (b) Temperature dependent study (300 to 50 K) of the current-voltage characteristics. (inset: a plot of rectification ratio as a function of bias) (c) I-V (red) and G-V (blue) curves at 20 K. (d) Theoretical calculations (fitted) showing good agreement with the experimental I-V and G-V curves (measured). Reprinted with permission from reference [36]. Copyright 2012 American Chemical Society.

1.3.2 Molecular Rectification Induced by Anchoring Groups

An interesting example that demonstrated the effect of dipole moment is the studies of the different coupling strength of two anchoring groups with the electrodes.

We designed and prepared two dipyrimidinyldiphenyl possessing thiol/thiol and thiol/isocyanide anchoring groups (Figure 1.9a).[53] Significant difference in rectification effect was observed between **6** and **7** even though both molecules contain the same organic conjugated structure and the orientation and the molecular backbone was identical (Figure 1.9). In STM measurement, a significant rectifying I-V curve was observed for **6** and a much smaller rectification ratio was observed for **7**. (Figure 1.9b and c) Theoretical calculation revealed that replacing the electron donating thiol anchoring group with electron-withdrawing isocyano group led to the decrease of calculated molecule dipole moment from 6.3 D to 2.5 D. The HOMO of **6** is predominantly located on the biphenyl segment while the LUMO of **6** located on the bipyrimidyl moiety. The HOMO and the LUMO of **7** is evenly distributed over the entire molecule with the isocyano group possessed a large orbital distribution in both the LUMO and the HOMO. The decrease in dipole moment could account for the decrease in rectification ratio but not the inverse of rectification direction. The inverse of rectification direction came from different bond dipoles resulted from the different Fermi level alignment between the thiol and isocyano anchoring groups and the gold surface. When thiol bonds with gold, a negative bond dipole forms. In contrast, when isocyano group bonds with the gold surface, a positive bond dipole was generated. In **6**, the bond dipole was cancelled. Thus, the molecular dipole dominates the direction of rectification and the charge carrier tunnels through the HOMO. In **7**, the bond dipole between Au and isocyano group increased the Fermi level of Au surface and the thiol-Au bond decrease the Fermi lever of Au NP. Since the molecular dipole of molecule **6** is only 2.5 D, the difference in Fermi levels of Au substrate and Au NP dominates. Therefore, an inversed rectifying effect between molecular diode **6** and **7** was observed.

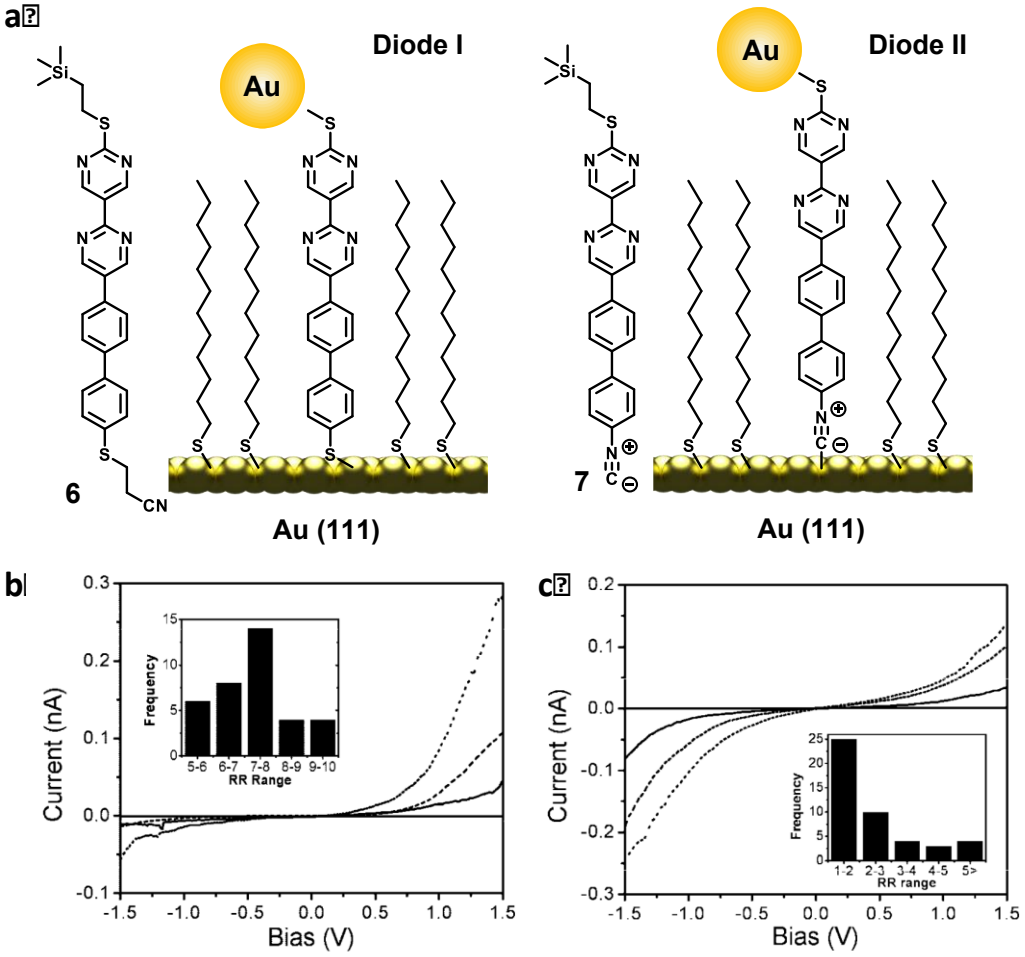

Figure 1.9 (a) Self-assembly of diblock molecules with thiol/thiol anchoring groups (6) and thiol/isocyanide anchoring groups (7) on Au surface. I-V curves at different current set points of 6 (b) and 7 (c) (insets: frequency of different rectification ratio ranges). Reprinted with permission from reference [53]. Copyright 2009 American Chemical Society.

1.3.3 Molecular Rectification Induced by Transition Metal Gates

Another surprising manifestation of dipolar effect came from studies of charge transport through single molecular transition metal complex. Two complexes consisting of redox active Ru[54] and Co[55] metal centers were investigated. Their structures are illustrated in Figure 1.10.

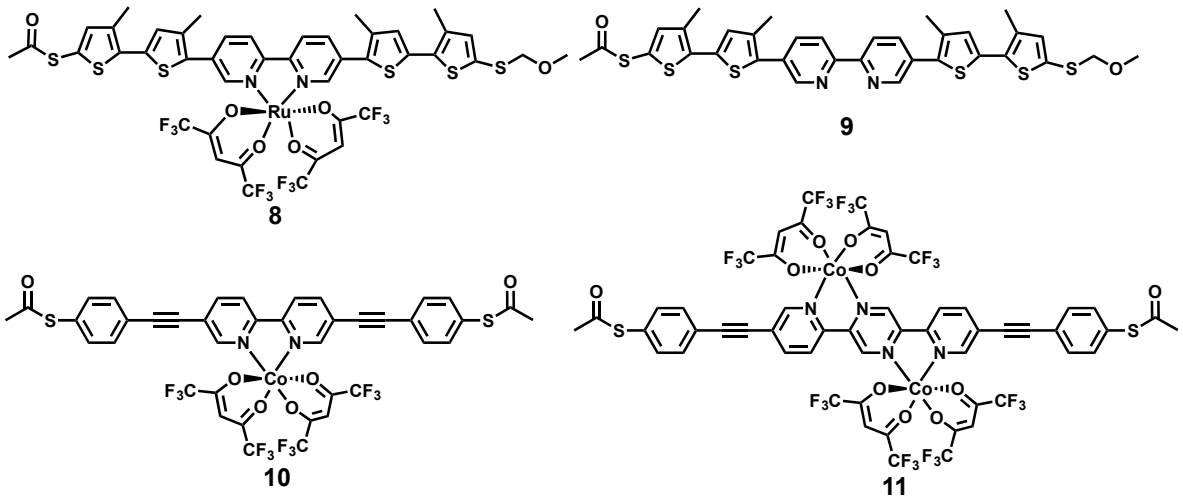

Figure 1.10 Illustration of the Structures of Transition Metal Complexes

We prepared compound **8** (Figure 1.10) to study the potential redox gating effect of the metal complex on the molecular wires.[54] Metal to ligand charge transfer bands observed in UV-vis spectrum indicates the blending of the π orbitals of the backbone ligand with the d orbitals of Ru metal centers. Compound **8** was immobilized on Au surface by stepwise de-protection strategy. The acetyl group was removed by NH_4OH and the molecule was inserted in a DDT SAM. A second deprotection of the MOM group with trifluoroacetic acid exposed the free thiol group for immobilization of gold nanoparticles. The same deprotection sequence was applied to the reference molecule **9** as well. The I-V curve of 8 showed asymmetric character while the I-V curve of the **9** is symmetric (Figure 1.11).

This asymmetry of **8** came from the projection of dipole of metal complex on the backbone as illustrated in Figure 1.11. The conductivity of ruthenium containing molecular wire is higher than that of the molecular backbone due to the forced planar conformation of the backbone by the chelating ruthenium complex. Moreover, the I-V curve of **8** showed multiple fine structures and the reference I-V curve of the **9** is smooth across the measurement. (Figure 1.11b and d)

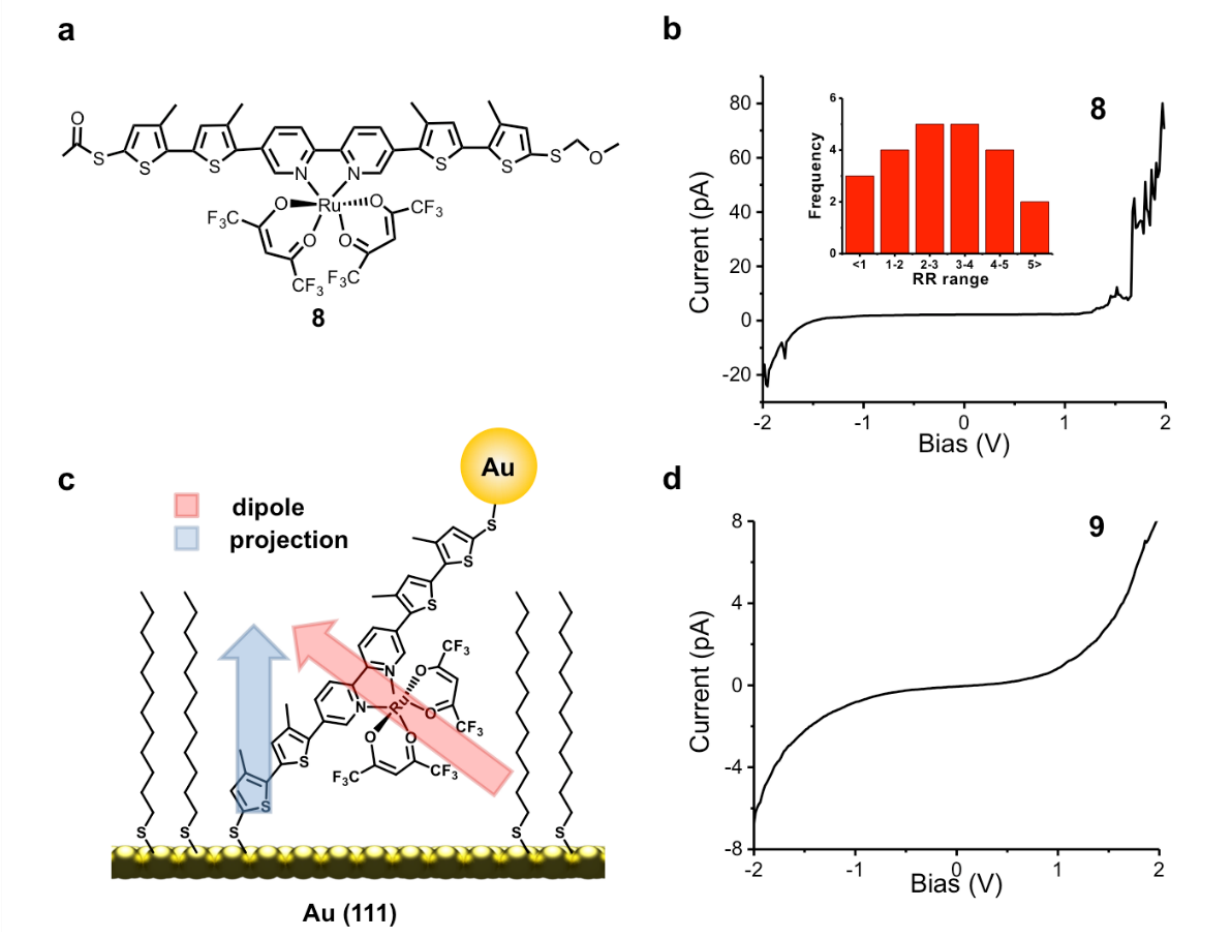

Figure 1.11 The structure of 8 (a), the orientation of 8 assembled on Au surface (c), the I-V curve of 8 (b) and the I-V curve of the 9 (d). Reproduced from Ref. [54] with permission from The Royal Society of Chemistry.

The fine structure of the I-V curve of **8** can be explained by the coupling of metal d orbitals with ligand π and π* orbitals. We calculated the molecular orbitals of the entire complex and found d_{xy}, d_{yz} and d_{xz} orbitals are coupled with π* orbital. This coupling provides resonance channel for charge transfer through π* orbital. When applying voltage so that the Fermi level of the electrode is in resonance with these orbitals, small negative differential resistance (the fine structures in I-V curve) was observed due to the reduction of available state density.

We further proved our hypothesis of rectification through projection of dipole *via* the comparison of two cobalt-containing complexes (**10** and **11** in Figure 1.10).[55] The two complexes have similar backbone structures. Both complexes showed metal to ligand charge transfer band in UV-vis spectrum. The molecules were deposit on Au surface assembled with DDT SAM.

As it is shown in Figure 1.12, the dipole moment in the monocobalt complex has a projection on the molecular backbone while the dipole moment of the di-cobalt complex cancelled out. The conductivities of metal complexes are higher than the backbones as observed in ruthenium complexes. Moreover, the asymmetric character of the I-V curves was observed only in the case of monocobalt complex but not in the di-cobalt complex. Fine structures were detected in the I-V curves of both **10** and **11**. These observations demonstrated that the asymmetric character of the mono metal complex molecular wire indeed come from the dipole projection on the molecular backbone. The fine structures in both cases showed the interaction of metal d orbitals with ligand π and π^* orbitals.

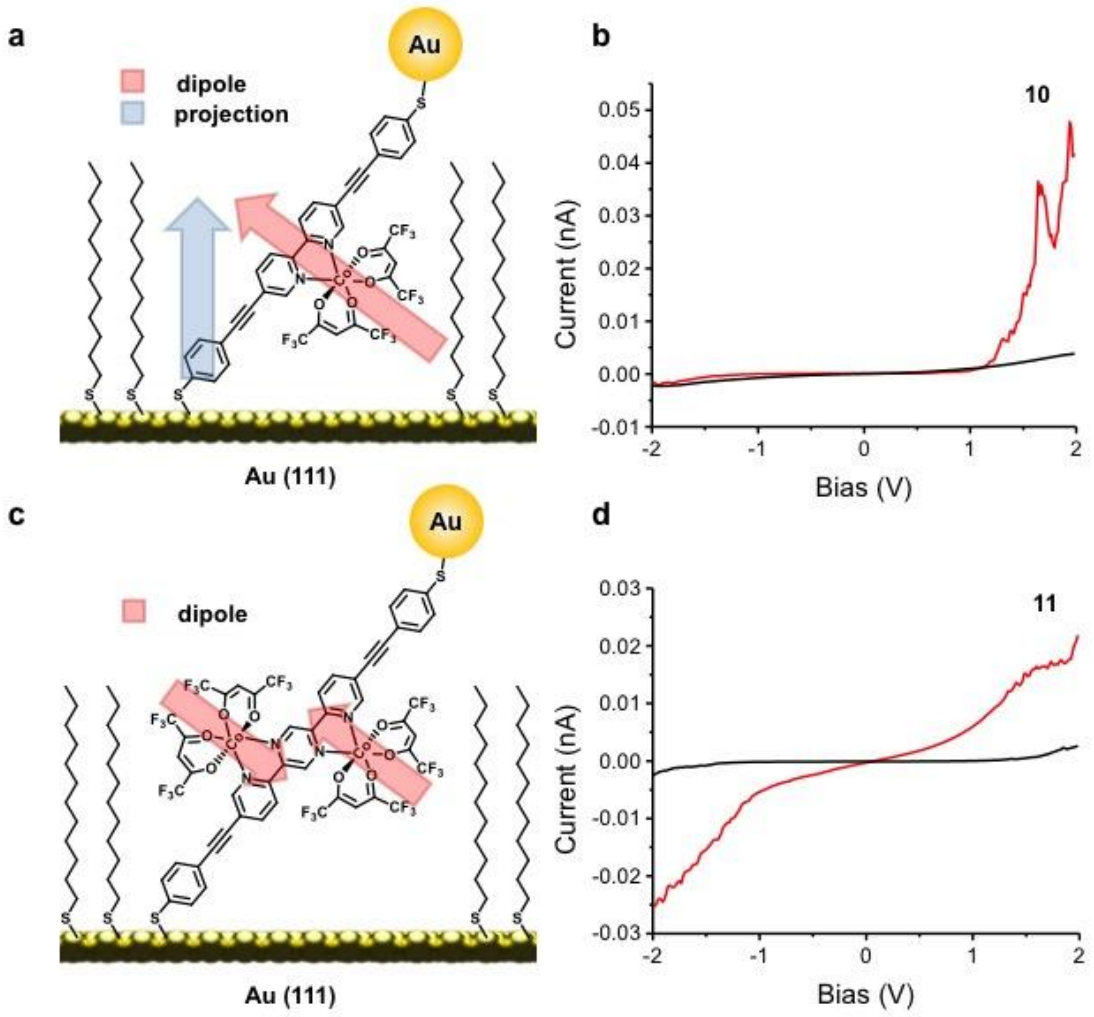

Figure 1.12 Assembly of 10 and 11 on Au surface (a and c) and the I-V curves of these two metal complexes (b and d in red) compared with the backbones (b and d in black).[55]

1.3.4 Other Effects Impacting Rectification and Conductance

We have also investigated the effect of hydrogen bonding on the rectification effect in molecular diode. In order to study the difference in electronic properties of molecular diode in the presence and the absence of an intramolecular hydrogen bond, we have designed and synthesized molecular diode incorporated with the hydroxyphenyl pyridine unit (Figure 1.13).[56]

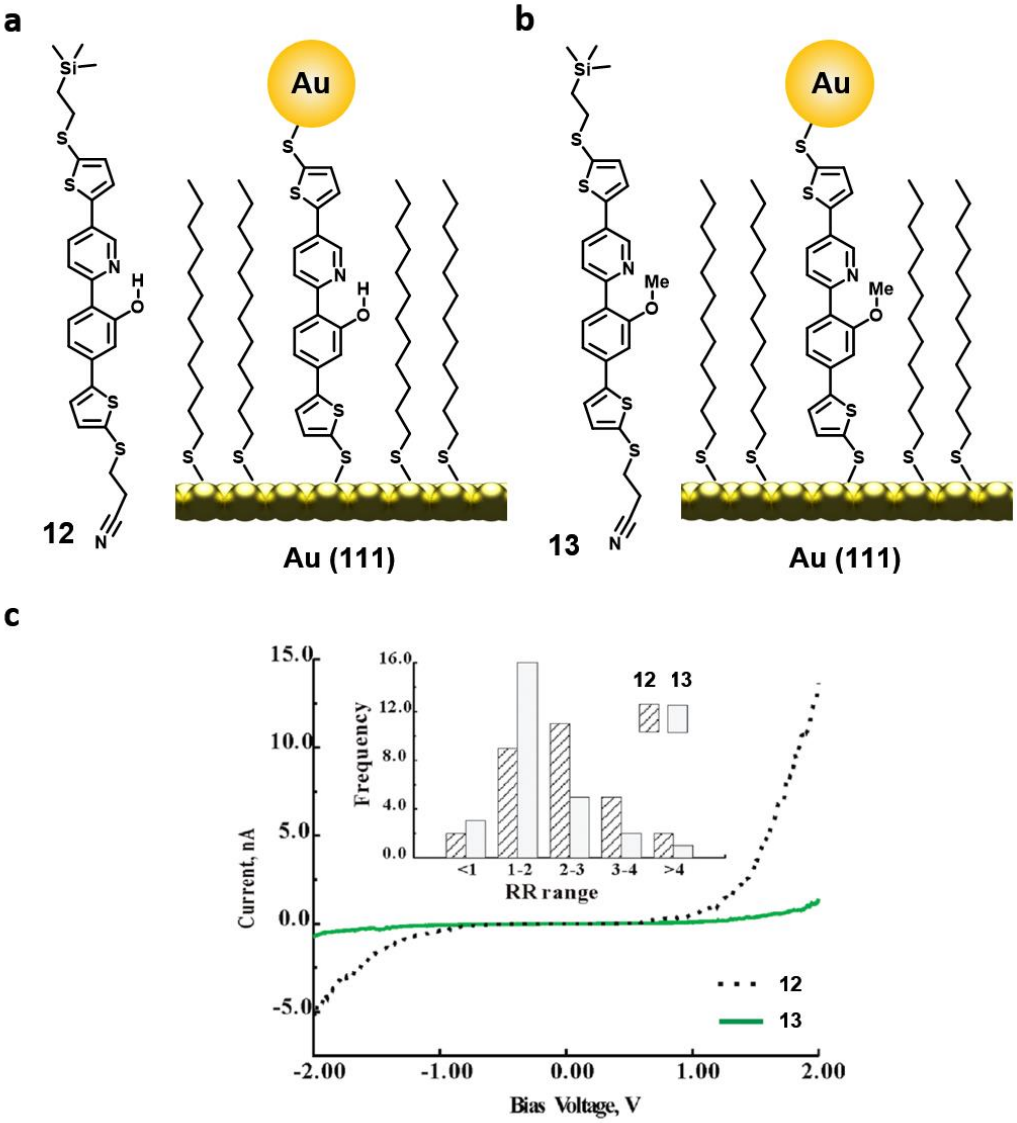

Figure 1.13 Structures and assembly of molecular wires with (a, 12) and without (b, 13) intramolecular hydrogen bond. (c) I-V curves of 12 (dashed black) and 13 (solid green) and rectification ratios (insert) of molecular wires 12 (gray, filled) and 13 (light blue, empty). Adapted with permission from reference [56]. Copyright (2011) American Chemical Society.

A control compound was also prepared with a methyl group replacing the hydrogen on the hydroxyl group. Similar to other diode studies, asymmetric protecting groups were used to allow alignment of diode orientation during self-assembly. STS measurements revealed that both

molecular wires display moderate asymmetric charge transport behavior. The wire containing hydrogen bond showed slightly higher rectification ratio. Moreover, the hydroxyphenyl pyridine diode showed a much higher current under bias, suggesting that charge transport is assisted by hydrogen bonding (Figure 1.13c). DFT calculations showed that the optimized structure of the hydroxyphenyl pyridine diode is planar, while the control compound with the methyl group is completely twisted, which explains the poor conductivity due to disrupted conjugation. More detailed theoretical study based on nonequilibrium Green's function method showed that the hydrogen bonding induced coplanar structure of **12** results in higher single molecule conductivity.[57] When the hydrogen bond is removed by turning the hydroxyl group away from the pyridine, the current value is lowered with this metastable state comparing to the original molecule.

1.4 References

(1) Waldrop, M. M. *Nature* **2016**, *530*, 144-147.
(3) Szent-Gyorgyi, A. *Proc. Natl. Acad. Sci. U S A* **1967**, *58*, 2012-2014.
(4) Mann, B.; Kuhn, H. *J. Appl. Phys.* **1971**, *42*, 4398-4405.
(5) Aviram, A.; Ratner, M. A. *Chem. Phys. Lett.* **1974**, *29*, 277-283.
(6) Geddes, N. J.; Sambles, J. R.; Jarvis, D. J.; Parker, W. G. *Appl. Phys. Lett.* **1990**, *56*, 1916-1918.
(7) Ashwell, G. J.; Dawnay, E. J. C.; Kuczynski, A. P. *J. Chem. Soc., Chem. Commun.* **1990**, 1355-1357.
(8) Metzger, R. M.; Chen, B.; Hopfner, U.; Lakshmikantham, M. V.; Vuillaume, D.; Kawai, T.; Wu, X.; Tachibana, H.; Hughes, T. V.; Sakurai, H.; Baldwin, J. W.; Hosch, C.; Cava, M. P.; Brehmer, L.; Ashwell, G. J. *J. Am. Chem. Soc.* **1997**, *119*, 10455-10466.
(10) Xiang, D.; Wang, X.; Jia, C.; Lee, T.; Guo, X. *Chem. Rev.* **2016**, *116*, 4318-4440.
(11) Love, J. C.; Estroff, L. A.; Kriebel, J. K.; Nuzzo, R. G.; Whitesides, G. M. *Chem. Rev.* **2005**, *105*, 1103-1169.
(12) Park, Y. S.; Whalley, A. C.; Kamenetska, M.; Steigerwald, M. L.; Hybertsen, M. S.; Nuckolls, C.; Venkataraman, L. *J. Am. Chem. Soc.* **2007**, *129*, 15768-15769.
(13) Venkataraman, L.; Klare, J. E.; Tam, I. W.; Nuckolls, C.; Hybertsen, M. S.; Steigerwald, M. L. *Nano Lett* **2006**, *6*, 458-462.
(14) Xu, B.; Tao, N. J. *Science* **2003**, *301*, 1221-1223.
(15) Mischenko, A.; Zotti, L. A.; Vonlanthen, D.; Bürkle, M.; Pauly, F.; Cuevas, J. C.; Mayor, M.; Wandlowski, T. *J. Am. Chem. Soc.* **2010**, *133*, 184-187.

(16) Zotti, L. A.; Kirchner, T.; Cuevas, J.; Pauly, F.; Huhn, T.; Scheer, E.; Erbe, A. *Small* **2010**, *6*, 1529-1535.
(17) Chen, F.; Li, X.; Hihath, J.; Huang, Z.; Tao, N. *J. Am. Chem. Soc.* **2006**, *128*, 15874-15881.
(18) Martin, C. A.; Ding, D.; Sørensen, J. K.; Bjørnholm, T.; van Ruitenbeek, J. M.; van der Zant, H. S. J. *J. Am. Chem. Soc.* **2008**, *130*, 13198-13199.
(19) Prins, F.; Barreiro, A.; Ruitenberg, J. W.; Seldenthuis, J. S.; Aliaga-Alcalde, N.; Vandersypen, L. M. K.; van der Zant, H. S. J. *Nano Lett* **2011**, *11*, 4607-4611.
(20) Hong, W.; Manrique, D. Z.; Moreno-García, P.; Gulcur, M.; Mischenko, A.; Lambert, C. J.; Bryce, M. R.; Wandlowski, T. *J. Am. Chem. Soc.* **2012**, *134*, 2292-2304.
(21) Su, T. A.; Neupane, M.; Steigerwald, M. L.; Venkataraman, L.; Nuckolls, C. *Nat. Rev. Mats.* **2016**, *1*, 1-15.
(22) Dell, E. J.; Capozzi, B.; Xia, J.; Venkataraman, L.; Campos, L. M. *Nat. Chem.* **2015**, *7*, 209-214.
(23) Batra, A.; Kladnik, G.; Gorjizadeh, N.; Meisner, J.; Steigerwald, M.; Nuckolls, C.; Quek, S. Y.; Cvetko, D.; Morgante, A.; Venkataraman, L. *J. Am. Chem. Soc.* **2014**, *136*, 12556-12559.
(24) Khobragade, D.; Stensrud, E. S.; Mucha, M.; Smith, J. R.; Pohl, R.; Stibor, I.; Michl, J. *Langmuir* **2010**, *26*, 8483-8490.
(25) Hong, W.; Li, H.; Liu, S.-X.; Fu, Y.; Li, J.; Kaliginedi, V.; Decurtins, S.; Wandlowski, T. *J. Am. Chem. Soc.* **2012**, *134*, 19425-19431.
(26) Saby, C.; Ortiz, B.; Champagne, G. Y.; Bélanger, D. *Langmuir* **1997**, 6805-6813.
(27) Venkataraman, L.; Klare, J. E.; Nuckolls, C.; Hybertsen, M. S.; Steigerwald, M. L. *Nature* **2006**, *442*, 904-907.
(28) Liu, S.; Tok, J. B. H.; Bao, Z. *Nano Lett* **2005**, *5*, 1071-1076.
(29) Choi, S. H.; Kim, B.; Frisbie, C. D. *Science* **2008**, 1482-1486.
(30) Valkenier, H.; Guédon, C. M.; Markussen, T.; Thygesen, K. S.; van der Molen, S. J.; Hummelen, J. C. *Phys. Chem. Chem. Phs.* **2014**, *16*, 653-662.
(31) Simmons, J. G. *J. Appl. Phys.* **1963**, *34*, 1793-1803.
(32) Metzger, R. M. *Chem. Rev.* **2015**, *115*, 5056-5115.
(33) Zhang, L.; Colella, N. S.; Cherniawski, B. P.; Mannsfeld, S. C. B.; Briseno, A. L. *ACS Appl. Mater. Interfaces* **2014**, *6*, 5327-5343.
(34) Yamada, R.; Kumazawa, H.; Noutoshi, T.; Tanaka, S.; Tada, H. *Nano Lett* **2008**, *8*, 1237-1240.
(35) Leary, E.; Hobenreich, H.; Higgins, S. J.; van Zalinge, H.; Haiss, W.; Nichols, R. J.; Finch, C. M.; Grace, I.; Lambert, C. J.; McGrath, R.; Smerdon, J. *Phys. Rev. Lett.* **2009**, *102*, 086801.
(36) Lörtscher, E.; Gotsmann, B.; Lee, Y.; Yu, L.; Rettner, C.; Riel, H. *ACS Nano* **2012**, *6*, 4931-4939.
(37) Ie, Y.; Endou, M.; Lee, S. K.; Yamada, R.; Tada, H.; Aso, Y. *Angew. Chem., Int. Ed.* **2011**, *50*, 11980-11984.
(38) Zhitenev, N. B.; Meng, H.; Bao, Z. *Phys. Rev. Lett.* **2002**, *88*, 226801.
(39) Ashwell, G. J.; Tyrrell, W. D.; Whittam, A. J. *J. Am. Chem. Soc.* **2004**, *126*, 7102-7110.
(40) Lara-Avila, S.; Danilov, A.; Geskin, V.; Bouzakraoui, S.; Kubatkin, S.; Cornil, J.; Bjørnholm, T. *J. Phys. Chem. C* **2010**, *114*, 20686-20695.
(41) Jia, C.; Migliore, A.; Xin, N.; Huang, S.; Wang, J.; Yang, Q.; Wang, S.; Chen, H.; Wang, D.; Feng, B.; Liu, Z.; Zhang, G.; Qu, D.-H.; Tian, H.; Ratner, M. A.; Xu, H. Q.; Nitzan, A.; Guo, X. *Science* **2016**, *352*, 1443-1445.

(42) Vazquez, H.; Skouta, R.; Schneebeli, S.; Kamenetska, M.; Breslow, R.; Venkataraman, L.; Hybertsen, M. S. *Nat. Nanotechnol.* **2012**, *7*, 663-667.
(43) Aradhya, S. V.; Meisner, J. S.; Krikorian, M.; Ahn, S.; Parameswaran, R.; Steigerwald, M. L.; Nuckolls, C.; Venkataraman, L. *Nano Lett* **2012**, 1643-1647.
(44) Wang, H. B.; Ng, M. K.; Wang, L. M.; Yu, L. P.; Lin, B. H.; Meron, M.; Xiao, Y. N. *Chem-Eur J* **2002**, *8*, 3246-3253.
(45) Ng, M.; Lee, D.; Yu, L. *J. Am. Chem. Soc.* **2002**, *124*, 11862-11863.
(46) Jiang, P.; Morales, G. M.; You, W.; Yu, L. *Angew. Chem. Int. Ed.* **2004**, *43*, 4471-4475.
(47) Hihath, J.; Bruot, C.; Nakamura, H.; Asai, Y.; Diez-Perez, I.; Lee, Y.; Yu, L.; Tao, N. *ACS Nano* **2011**, *5*, 8331-8339.
(48) Diez-Perez, I.; Hihath, J.; Lee, Y.; Yu, L. P.; Adamska, L.; Kozhushner, M. A.; Oleynik, I. I.; Tao, N. J. *Nat. Chem.* **2009**, *1*, 635-641.
(49) Oleynik, I. I.; Kozhushner, M. A.; Posvyanskii, V. S.; Yu, L. *Phys. Rev. Lett.* **2006**, *96*, 096803.
(50) Morales, G. M.; Jiang, P.; Yuan, S. W.; Lee, Y. G.; Sanchez, A.; You, W.; Yu, L. P. *J. Am. Chem. Soc.* **2005**, *127*, 10456-10457.
(51) Gasyna, Z. L.; Morales, G. M.; Sanchez, A.; Yu, L. *Chem. Phys. Lett.* **2006**, *417*, 401-405.
(52) Zhang, G.-P.; Xie, Z.; Song, Y.; Hu, G.-C.; Wang, C.-K. *Chem. Phys. Lett.* **2014**, *591*, 296-300.
(53) Lee, Y.; Carsten, B.; Yu, L. *Langmuir* **2009**, *25*, 1495-1499.
(54) Lee, Y.; Yuan, S.; Sanchez, A.; Yu, L. *Chem. Commun.* **2008**, 247-249.
(55) Lee, Y.; Yuan, S.; Yu, L. *Sci. China Chem.* **2011**, *54*, 410-414.
(56) Wang, W.; Yu, L. *Langmuir* **2011**, *27*, 2084-2087.
(57) Song, Y.; Xie, Z.; Wei, M.-Z.; Leng, J.-C.; Li, Z.-L.; Wang, C.-K. *Comp. Mater. Sci.* **2015**, *108*, 8-13.

CHAPTER 2

EDGE-ON GATING EFFECT IN MOLECULAR WIRES

2.1 Introduction and Background

Charge transport through single molecules is an active research topic that involves design, syntheses, physical measurements and theoretical understanding of functional molecules that can control charge transport.[1-3] The extensive research effort in both measurements and theoretical calculations of the charge transport phenomenon has led to deeper understanding on this topic. Different molecular components, including molecular wires and diode molecules were synthesized and investigated. Despite this progress, controlling charge transport through single molecules is still a challenging issue.[4, 5] Electric gating is an important means to manipulate charge transport behavior in semiconductor devices, which is the basis of field effect transistors (FET). The same gating effect was pursued in a limited number of field effect transistor structures using single molecular semiconductor, such as C60[6, 7], carbon nanotube[8] or simple 1,4-benzenedithiol[9] via external third gating electrode separated by an oxide dielectric layer. However, these molecular transistors were prepared with an exhaustive nanofabrication of small electrode gaps with very low yield.[10, 11] Other approaches were applied to study the gating effect, such as electrochemical gating.[12-14] There is no molecule that mimics the function of a transistor and can be investigated via a simple approach although several theoretical studies have dealt with this topic.[15, 16] An interesting example was reported by Rabe *et al*, in which the current through a hybrid molecular diode is modulated by the formation of charge transfer interaction.[17]

In the following study, we have designed and synthesized a single molecular transistor system that contains cyclophane moieties as shown in Figure 2.1 and investigated their electric gating effect on molecular junctions. The cyclophane moiety ([2.2](2,6)pyridinoparacyclophane-1,9-diene) offers a building motif for transistor molecules containing drain, source and gating termini; each of them can exhibit orthogonal reactivity for connection to an electric circuit. The building motif is a known compound that was shown to exhibit a perpendicular orientation between two aromatic rings[18, 19]. In this molecular system, the perpendicular pyridine moiety is connected to the conjugated semiconducting segment with two vinyl groups. The π-system in the pyridine ring and vinyl groups is orthogonal to that in the semiconducting wire (Figure 2.1). It provides several covalent bonding sites that can be chemically manipulated to introduce functional groups. This system is designed to mimic the structure of a bulk transistor at the molecular level, in which the pyridine unit can be used as the gating end that is not directly conjugated with the semiconducting entity. The double bonds in the cyclophane moiety act as the dielectric component to electrically isolate the gate from the semiconductor. The functional groups exert gating effect indirectly similar to a FET setup. Although our ultimate goal is to connect the molecule to three electrodes via orthogonal reactions, it is currently impossible for us to connect three termini into an external circuit with controlled precision. Thus we decided first to investigate the chemical gating effect.

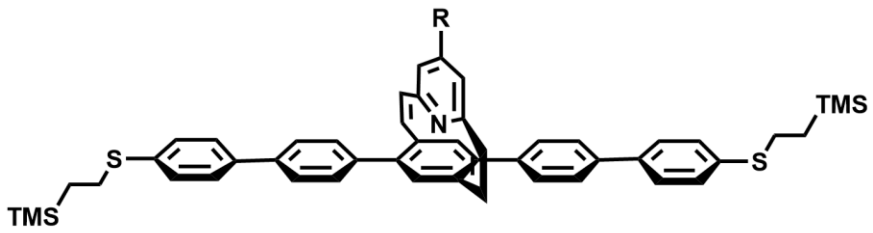

Figure 2.1 Chemical Structure of the protected cyclophane molecular wires.

Pentaphenylene bearing protected thiols on the ends was chosen to be the molecular semiconductor with structures as shown in Figure 2.1 in which the cyclophane core is integrated into it with the thiols as the anchoring groups for drain and source electrodes. The edge-on pyridine unit was functionalized with different groups that possess varied electronic demands, which will play the role of applied gating voltage to modulate the charge conductance in the molecular junction. These substituents, namely NO_2, Cl, H, OCH_3, and $N(CH_3)_2$, are attached onto the para-position of the pyridine in the cyclophane moiety and range from strongly electron withdrawing to strongly electron donating. Syntheses of these molecules are shown as followed:

2.2 Sample Characterizations and STM Break-Junction Experiments

To measure the conductance of single molecules, a self-assembled monolayer film of the deprotected molecules was prepared on gold surface via thiol-gold reaction[20]. The molecules with two terminal thiol groups strongly couple with two gold electrodes to form a molecular junction. A representative metal-molecule-metal junction is shown in Figure 2.2a. The density of the anchored molecules was characterized with cyclic voltammetry after the top thiol group was functionalized with ferrocene thioester as a reporting molecule. It was found that the typical surface coverage of molecules is around 7.2×10^{-10} mol·cm^{-2}. Cyclic voltammograms of the experiment are shown in Figure 2.3.

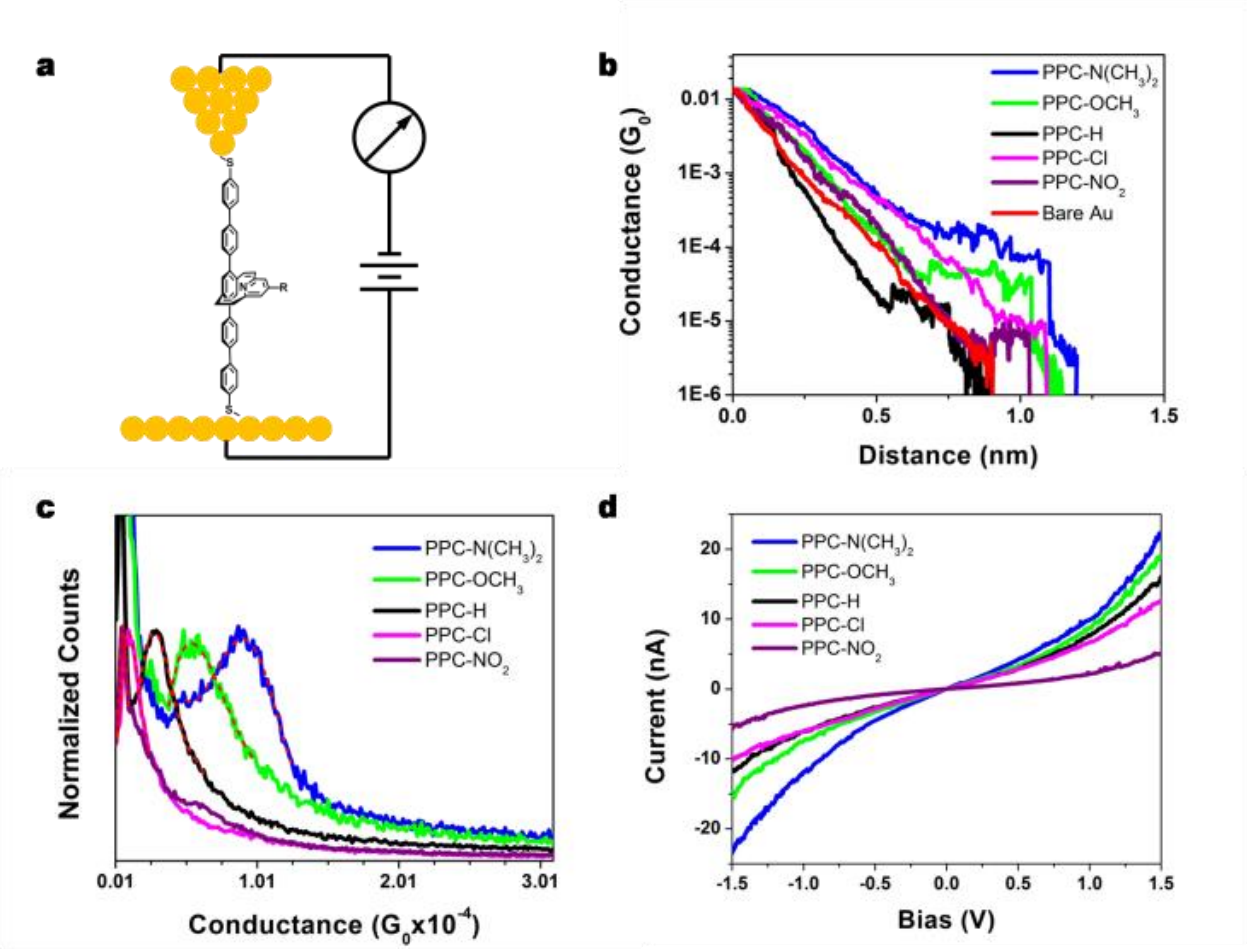

Figure 2.2 (a) A representative metal-molecule-metal junction in STM break-junction technique. (b) Sample conductance traces of molecular junctions with gating substituent: -NO_2, -Cl, -H, -OCH_3, and -$N(CH_3)_2$. (c) Conductance histogram of the five molecular junctions. Red dash lines represent polynomial fitting of each peak. (d) Single current-voltage characteristic curves of the five molecular junctions constructed from the average of 30 individual curves.

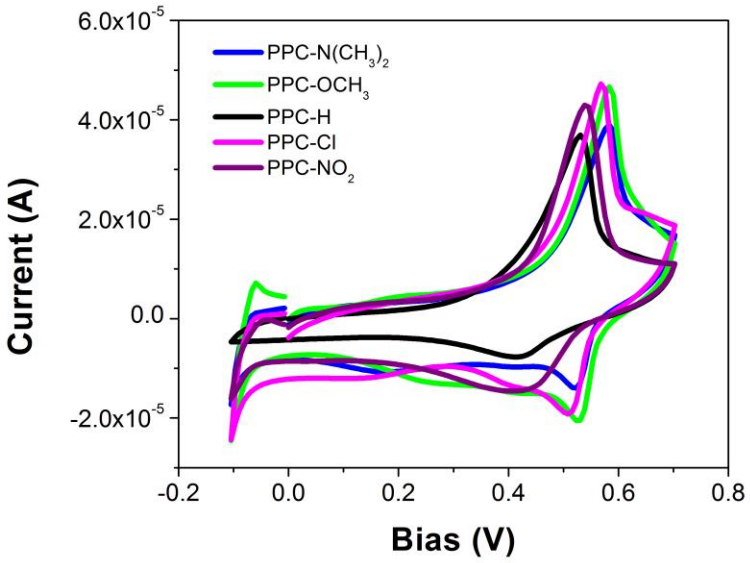

Figure 2.3 Cyclic voltammograms of ferrocene functionalized PPC molecular wire monolayer on gold.

2.2.1 Single-Molecule Gating of Conductance

The conductance of the molecular junctions was measured by using the break-junction technique with a modified STM system.[21-23] The experiments were carried out at 100mV of bias voltage in toluene according to the protocol by the Tao group.[22] The conductance traces of the molecules with different substituents were recorded by using a LabVIEW program and are shown in Figure 2.2b. In each measurement, molecule junctions are formed after the gold STM tip was brought into contact with a gold substrate functionalized with a monolayer of compound under a small bias voltage applied between the tip and the substrate. The STM tip was then pulled away from the substrate while monitoring the current between the tip and the substrate. A plateau in the conductance trace, recorded as the current as a function of pulling distance, before junction break would indicate the formation of a single molecule junction (Figure 2.2b).

The conductance in the last plateau in thousands of current traces for each molecule was analyzed statistically to produce a histogram with a clear peak, which corresponds to the single-molecule conductance at that bias voltage. From the conductance histograms in Figure 2.2c, the conductance values of molecules PPC-NO_2, PPC-Cl, PPC-H, PPC-OCH_3, and PPC-$N(CH_3)_2$ at 100 mV of bias voltage were determined to be $5.8 \times 10^{-6}\, G_o$, $11 \times 10^{-6}\, G_o$, $2.8 \times 10^{-5} G_o$, $5.8 \times 10^{-5}\, G_o$, and $9.1 \times 10^{-5}\, G_o$ respectively, where G_o equals $2e^2/h$ (e is the electron charge and h is the Plank constant). Systematic change can be clearly observed when the substituent changes from strong acceptor (NO_2) to strong donor ($N(CH_3)_2$).

2.2.2 Single-Molecule Current-Voltage Characteristics

To understand the charge transport mechanism in the single molecule junction at an extended bias voltage range, thousands of *I-V* curves were recorded for each molecule when the STM tip was pinned at the distance corresponding to single-molecule junction, which was deducted from the conductance measurements, and voltage was swept rapidly from -1.5V to 1.5V. Due to the instability of the single molecular junction caused by various side effects, such as high bias voltages and current-induced heating[21, 24, 25], a large portion of I-V curves (e.g. 47% of the total *I-V* curves for PPC-H) were thrown out automatically by the program.[23]

Based on the results of the conductance measurements, I-V curves were measured at the corresponding locations of the plateaus at around $5.8 \times 10^{-6}\, G_o$, $11 \times 10^{-6}\, G_o$, $2.8 \times 10^{-5} G_o$, $5.8 \times 10^{-5}\, G_o$, and $9.1 \times 10^{-5}\, G_o$ for PPC-NO_2, PPC-Cl, PPC-H, PPC-OCH_3, and PPC-$N(CH_3)_2$, respectively. 2D histograms of the I-V and the G-V relations can be found in Figure 2.4. Average I-V curves of the five molecular junctions constructed from 30 individual curves are shown in Figure 2.2d. It can be observed that the current displays a clear nonlinearity as a function of bias voltage. In particular, the current for the molecule with electron donating group increases much

faster at higher bias than that with electron withdrawing group. The conductance data clearly showed the gating effect, as the substituent becomes more electron-rich, the conductance increases. A better expression of the gating effect is the interesting correlation of conductance with the charge density change on the nitrogen atom in the pyridine ring. Density functional theory (DFT) calculations of these molecules yield the charge density on each atom. Specifically, we are more interested in the nitrogen atom in the pyridine ring whose charge density was shown in Table 2.1. Shown together in the table are also the Hammet parameters σ_{para}, which was developed for characterizing electronic effect of different functional groups on organic reactions. It is interesting to notice that the conductance changes correlate almost linearly with the charge density changes on nitrogen atom of the pyridine ring (relative to -H substituent) except for the compound containing the nitro group (Figure 2.5a). The Hammet equation gives a similar correlation (Figure 2.5b). When the pyridine ring in the cyclophane moiety is attached with electron withdrawing group, such as chlorine atom, the electronic density of the pyridine ring is reduced relative to that with hydrogen atom. The nitrogen atom in the pyridine ring bears less negative charge, which is confirmed from quantum mechanics calculation. On the other hand, a donating group (-$N(CH_3)_2$, or -OCH_3) can make the pyridine ring, thus the nitrogen atom, more negative, which will facilitate hole current through the molecule and increase the conductance. With no substituent present on the pyridine ring, effectively no bias is applied at the gate. As a comparison, the pentaphenylene wire was also synthesized and their conductance measured. It is very interesting to notice that the pentaphenylenedithiolate molecular junction exhibits a conductance of ca. $7.4 \times 10^{-5}\ G_o$, which is larger that of PPC-H ($2.8 \times 10^{-5} G_o$), but smaller than that of PPC-NMe_2($9.1 \times 10^{-5}\ G_o$). The difference is due to the significantly more twisted structure along the conjugating backbone caused by the cyclophane moiety of the PPC molecular wires (i.e. the two phenyl rings next to cyclophane)

than the pentaphenylene molecule. The detailed STM break junction experiment data of the pentaphenylene molecular junction is shown in Figure 2.6. Overall, the results indicated that variation in electronic demand in substituent is identical to the change in gating voltage and the single molecular circuit is performing similar to field effect transistor.

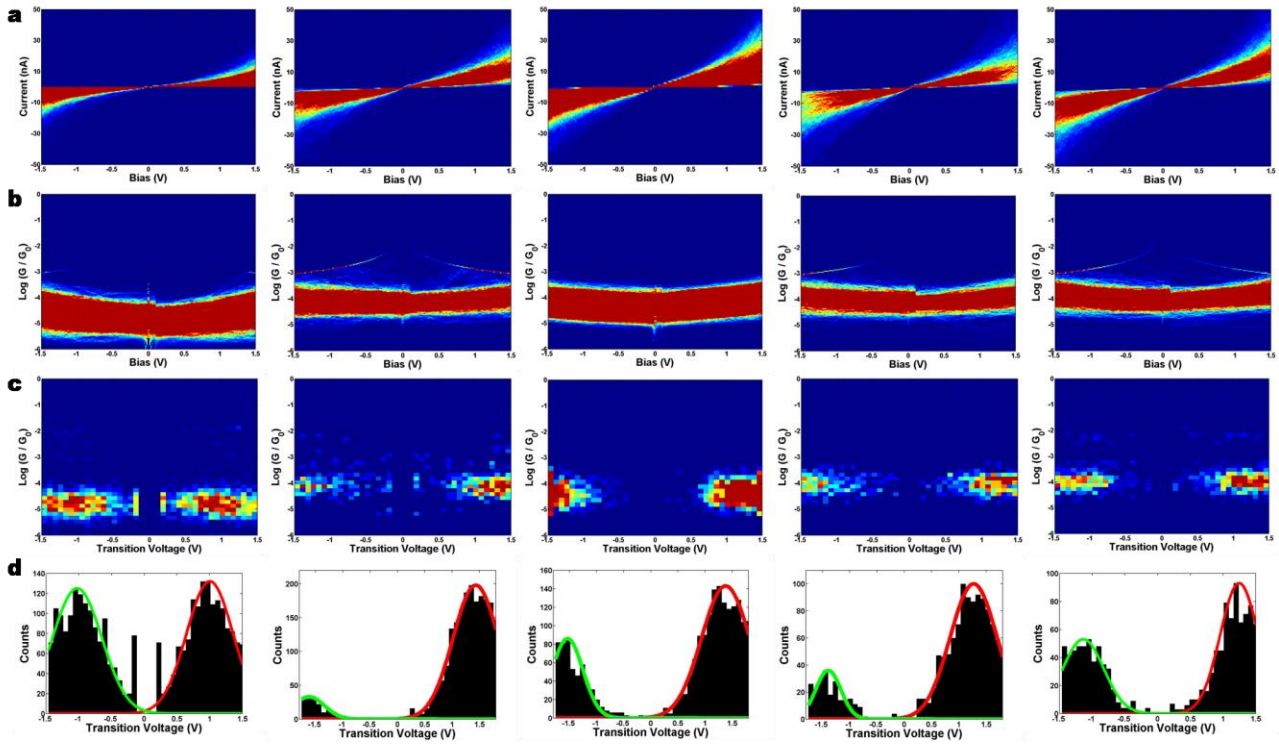

Figure 2.4 (a) Current-voltage 2D histograms, (b) conductance-voltage 2D histograms, (c) transition voltage 2D histograms, and (d) transition voltage 1D histograms of PPC molecular junctions with substituents -NO_2, -Cl, -H, -OMe, -$N(Me)_2$ (from left to right), respectively.

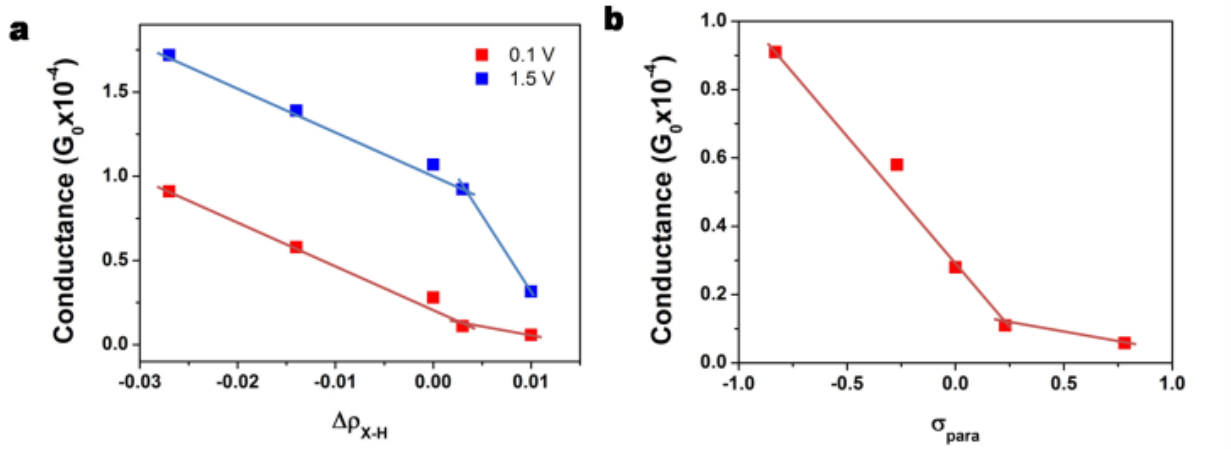

Figure 2.5 (a) A plot of conductance at 0.1 V (red) and 1.5 V (blue) against difference in charge of the pyridine N (from DFT calculations) of the four substituted PPC compare with PPC-H. The data points from left to right correspond to -N(CH_3)$_2$, -OCH_3, -H, -Cl, and -NO_2 respectively. (b) A plot of conductance against Hammet parameters of the corresponding functional group attached at the gate position. Colored lines are only used as eye guide.

Table 2.1 DFT calculation, STM experiment data, and other parameters.

Functional Groups	Charge on N[a,b]	$\Delta\rho_{X-H}$[b]	σ_{para}	Conductance (1×10^{-6} G_0)[c]	ΔE (eV)[b,d]	HOMO (eV)[b,d]	LUMO (eV)[b,d]	Barrier Height (eV)[c]
-NO_2	-0.568	0.010	0.78	5.8	2.746	-5.81725	-3.07081	0.87
-Cl	-0.575	0.003	0.23	11	4.058	-5.69262	-1.63513	1.36
-H	-0.578	0	0	28	4.177	-5.57153	-1.39458	1.26
-OMe	-0.592	-0.014	-0.27	58	4.184	-5.54976	-1.36601	1.15
-NMe_2	-0.605	-0.027	-0.83	91	4.148	-5.3982	-1.24955	1.03

[a]Mulliken charge analysis with b3lyp/6-31g*.
[b]Data obtained from theoretical calculations.
[c]Data obtained from STM experiments.
[d]DFT calculation is known to sometimes underestimate the gap of the molecule, therefore the bandgap values obtained from that are only good for rough comparisons with the experimental data.

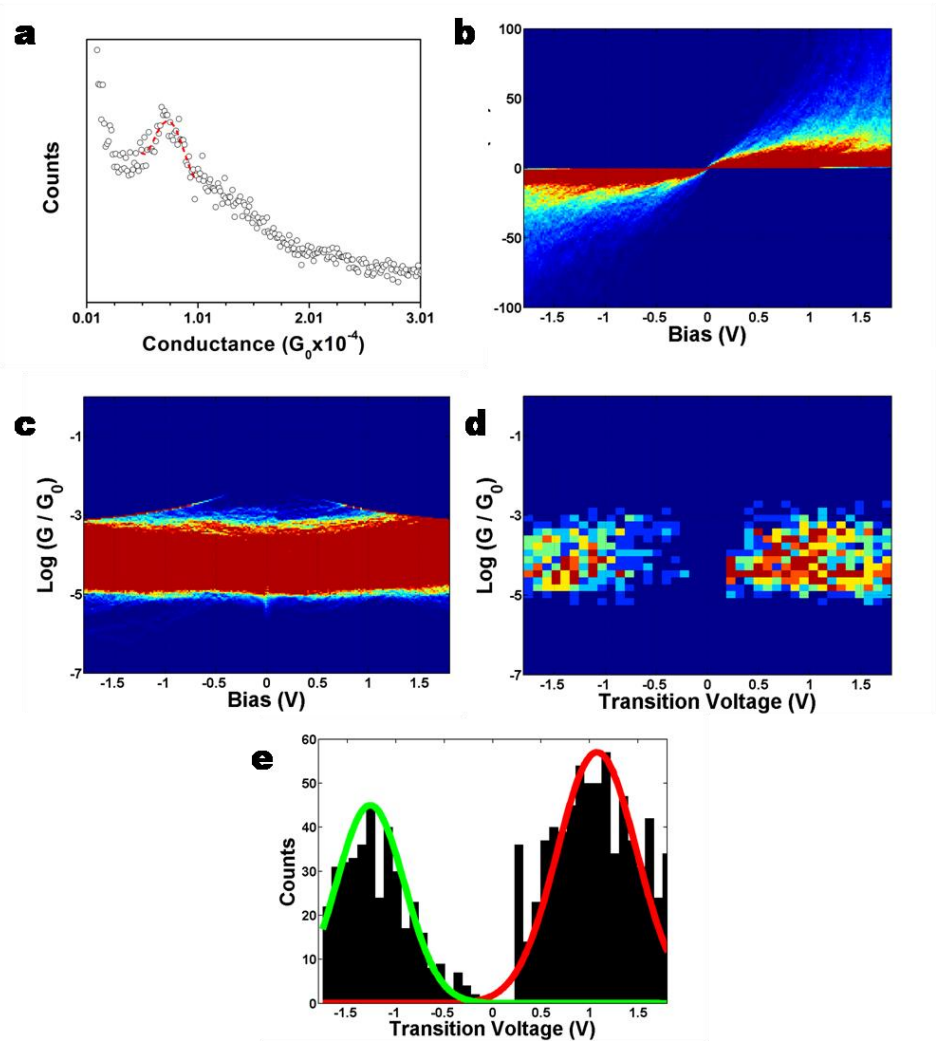

Figure 2.6 (a) Conductance histogram, (b) Current-voltage 2D histogram, (c) conductance-voltage 2D histogram, (d) transition voltage 2D histogram, and (e) transition voltage 1D histogram of the pentaphenylene dithiolate molecular junction. The molecular junction has a conductance of ca. 7.4 $\times 10^{-5}$ G_0.

2.2.3 Transition Voltage Spectroscopy Analysis

To better understand the edge-on gating effect on the charge transport mechanism, transition voltage spectroscopy (TVS) was recorded and used to determine the energy level alignment of the molecule.[26] Each I-V curve was converted into curve of $\ln(I/V^2)$ as a function of $1/V$, the so-called Fowler-Nordheim (FN) plot.[27] The minimum of the FN plot corresponds to the transition voltage

V_t and the 1D TVS histograms of the occurrence of the transition voltage can be constructed from these minimum values (Figure 2.7a-e). The heights of the charge tunneling barriers of molecules can then be deduced from the equation proposed by Baldea based on these transition voltage values.[28] The heights of the tunneling barriers of molecules with substituent groups of $-NO_2$, -Cl, -H, $-OCH_3$ and $-N(CH_3)_2$ was calculated to be ca 0.87 eV, 1.36 eV, 1.26 eV, 1.15 eV, and 1.03 eV respectively. The results clearly indicated that when the substituent changes from electron donor to electron acceptor, the transition voltage increased, and the charge tunneling barrier increase except for the compound with nitro group. The results of the other four compounds are consistent with the trend in the HOMO energy level deduced from DFT calculations by using calculation method RB3LYP with basis set 6-31G* (Table 2.1). In particular, the tunneling barrier for nitro group is very interesting and provides insightful information to be discussed below. The TVS histograms also indicated a significant asymmetry of conductance. This effect has been observed in many other systems, both conjugated or non-conjugated, and was attributed to the difference in geometry of two electrodes, one flat surface and the other a sharp tip.[22]

These results indicated that the pyridine unit modulates the conductance of the pentaphenylene via tuning the charge tunneling barriers. Since the main chain of the molecule is a p-type semiconductor, it favors hole transport through the HOMO of the molecule.[29] DFT calculations based on RB3LYP method with basis set 6-31G* show that the HOMO energy level of the molecular wire decreases when the substituent on the pyridine ring change from donor to acceptor (Table 2.1). This will cause an increase in charge tunneling barrier assuming the energy level alignment against the Fermi level of the gold was not significantly affected by the substituents. TVS results are consistent with the HOMO energy level changes for Cl, H, OCH_3 and $N(CH_3)_2$ molecules. However, the compound with nitro group exhibited abnormally small tunneling barrier,

yet its conductance is lower than other molecules. While studies have shown that the nitro group may potentially interact with gold surface[30, 31], we did not observe any substantial difference between the SAM of the nitro compound and that of the other wire molecules. Conductance histogram of the nitro molecular wire in our experiments shows a single well defined peak. Interaction from the nitro group with the gold surface would theoretically result in a different conductance value. Cyclovoltametry studies indicated similar surface coverage with other compounds. The similar anchoring effect with molecules containing thiolate and nitro side group was described in literature.[32] The results imply that the conduction mechanism in nitro compound is different from the others. Similar phenomenon can be observed in the effect of substituent on chemical reaction, the linear energy correlation often showed outstanding effect of nitro group due to mechanistic change.[33] From the DFT calculation results, we can notice that the LUMO energy level of the nitro compound (-3.07 eV) is unusually lowered than the others (around -1.3~-1.6 eV). Based on the tunneling barriers derived from TVS of the other four compounds, the energy offset of the four compounds are shown in Figure 2.7f, which puts the nitro compound in such energy level alignment that its LUMO energy level is closer to the Fermi energy level of gold electrodes. This implies that the charge transport in nitro compound is actually tunneling through the LUMO orbital. The DFT calculations showed that the LUMO orbital in the nitro compound is almost exclusively confined in the pyridine unit. The charge transport therefore has to tunnel through space via the nitropyridine, leading to diminished conductance.

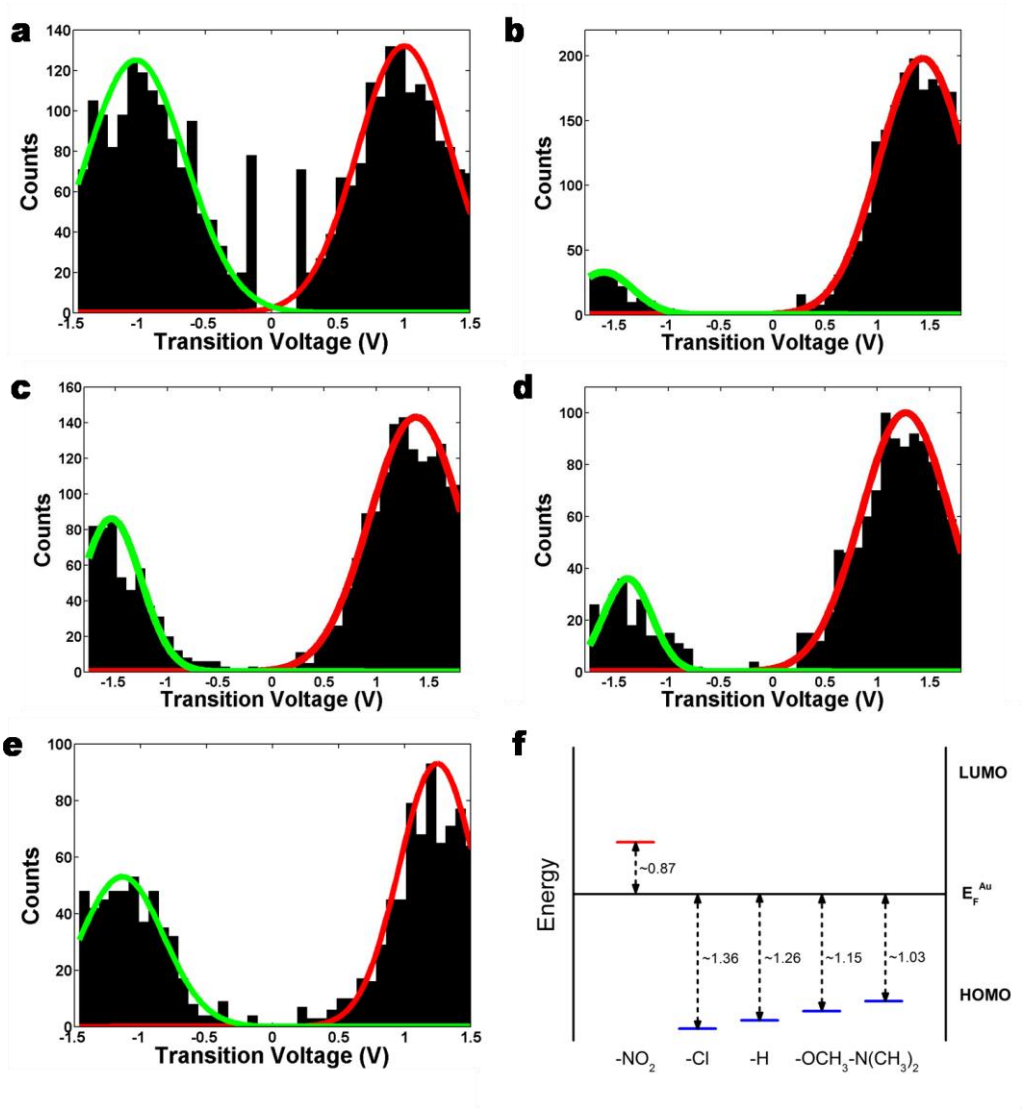

Figure 2.7 1D transition voltage histograms of (a) PPC-NO_2, (b) PPC-Cl, (c) PPC-H, (d) PPC-OCH_3, and (e) PPC-$N(CH_3)_2$ showing the occurrence of transition voltage for each molecular junction. (f)A plot of energy offsets calculated with the transition voltages from a-e for all five molecular junctions.

2.3 Conclusion

In conclusion, we have successfully synthesized a molecular wire system that demonstrated for the first time edge-on gating effect by utilizing the pyridinocyclophane moiety as the molecular gate. The gating effect is manifested via tuning the energy levels of the molecular orbitals.

Molecular conductance and current-voltage characteristics curves measured via STM break-junction method point out the possibility of molecular switching as a function of gating voltage.

2.4 Experimental Section

Syntheses of molecular wires:

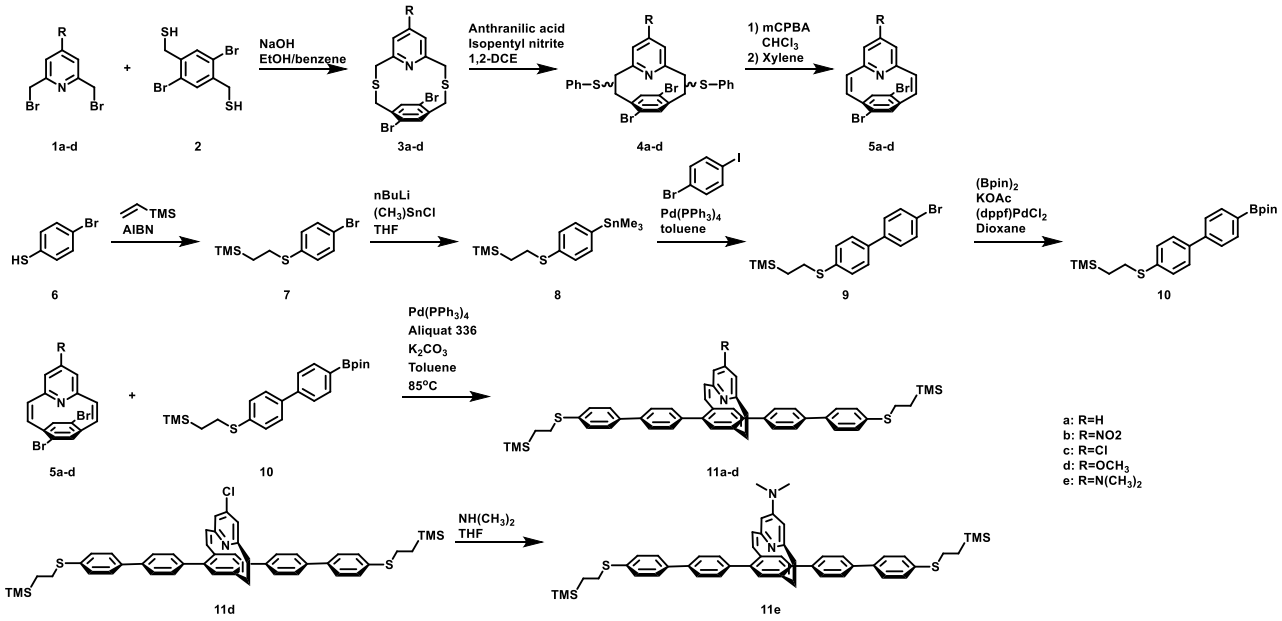

Scheme 2.1 Synthetic route of the cyclophane-gated molecular wires.

All of the chemicals were purchased from Aldrich except for tetrakis(triphenylphosphine)palladium from Strem Chemicals. All reagents purchased commercially were used without further purification except for toluene and tetrahydrofuran (THF), which were dried over sodium/benzophenone. ^{1}H NMR and ^{13}C NMR spectra were recorded on a Bruker DRX-400 spectrometer, with tetramethylsilane as an internal reference. Matrix-assisted laser desorption ionization time-of-flight (MALDI-TOF) mass spectra were recorded using a Bruker Ultraflextreme MALDI-TOF/TOF mass spectrometer with dithranol as the matrix. Compounds **1a-d**, **2** were prepared by standard literature methods.

5,8-Dibromo-2,11-dithia[3.3](2,6)pyridinoparacyclophane (3a). To a stirred solution of NaOH (0.526 g, 13.2 mmol) in ethanol (1.38 L) was added dropwise a solution of **1a** (1.57 g, 5.98 mmol) and **2** (1.95g, 5.98 mmol) in benzene (300 mL) over a period of 8 hours. The reaction was stirred for an additional 10 hours at room temperature. The solution was filtered and concentrated under reduced pressure. Chromatography of the residue over silica gel gave **3a** as white solid (1.54 g, 60% yield). ^{1}H NMR ($CDCl_3$, ppm): δ 3.57-3.68 (q, 4H), 3.74-4.20 (q, 4H), 7.13-7.15 (d, 2H), 7.22 (s, 2H), 7.49-7.53 (t, 1H). MS (MALDI-TOF/) m/z: Calcd, 428.9. Found, (M^+), 429.5.

5,8-Dibromo-7-nitro-2,11-dithia[3.3](2,6)pyridinoparacyclophane (3b). This was prepared following the general procedure given for the preparation of **3a**. From **1b** (2.00 g, 6.45 mmol) and **2** (2.12 g, 6.45 mmol) there was obtained **3b** as slight yellow solid (1.75 g, 57% yield). ^{1}H NMR ($CDCl_3$, ppm): δ 3.68-3.76 (q, 4H), 3.77-4.21 (q, 4H), 7.21 (s, 2H), 7.92 (s, 2H). MS (MALDI-TOF/) m/z: Calcd, 473.9. Found, (M^+), 474.6.

5,8-Dibromo-7-chloro-2,11-dithia[3.3](2,6)pyridinoparacyclophane (3c). This was prepared following the general procedure given for the preparation of **3a**. From **1c** (1.39 g, 4.63 mmol) and **2** (1.51 g, 4.63mmol) there was obtained **3c** as white solid (1.69 g, 79% yield). ^{1}H NMR ($CDCl_3$, ppm): δ 3.54-3.64 (q, 4H), 3.74-4.20 (q, 4H), 7.19 (s, 2H), 7.24 (s, 2H). MS (MALDI-TOF/) m/z: Calcd, 462.9. Found, (M^+), 463.5.

5,8-Dibromo-7-methoxy-2,11-dithia[3.3](2,6)pyridinoparacyclophane (3d). This was prepared following the general procedure given for the preparation of **3a**. From **1d** (2.00 g, 6.78 mmol) and

2 (2.22 g, 6.78 mmol) there was obtained **3d** as white solid (2.75 g, 88% yield). ^{1}H NMR ($CDCl_3$, ppm): δ 3.52-3.62 (q, 4H), 3.73-4.19 (q, 4H), 3.84 (s, 3H), 6.70 (s, 2H), 7.22 (s, 2H). MS (MALDI-TOF/) m/z: Calcd, 458.9. Found, (M^+), 459.4.

Benzyne-Stevens Rearrangement of 3a-d to Give 4a-d. To a solution of **3** (1.0 eq.) in 1,2-dichloroethane (45 mL/mmol) boiling under reflux was added isopentyl nitrite (10 eq.), followed by dropwise addition of a solution of anthranilic acid (2.5 eq.) in 1,2-dichloroethane (45 mL/mmol) over 2 hours. The reaction was refluxed for an additional 2 hours, cooled, and concentrated under reduced pressure. Chromatography of the residue over silica gel gave **4** as a mixture of isomers and was used directly in the next step.

4,7-Dibromo[2.2](2,6)pyridinoparacyclophane-1,9-diene (5a). To a solution of **4a** (100 mg, 0.172 mmol) in chloroform (5.73 mL) at -40°C was added dropwise a solution of m-chloroperoxybenzoic acid (77%) (85 mg, 0.378 mmol) in chloroform (5.73 mL). The reaction was stirred at -40°C for 1.5 hours, 0°C for 30 mins, and room temperature for 2 hours. The solution was then washed with aq $NaHCO_3$ solution, water, and brine, dried with $MgSO_4$ and concentrated under reduced pressure. The resulting residue was dissolved in m-xylene (12 mL) and heated to reflux under N_2 for 20 hours. The solution was allowed to cool to room temperature and concentrated under reduced pressure. Chromatography of the residue over silica gel gave **5a** as a white solid (10 mg, 16% yield). ^{1}H NMR ($CDCl_3$, ppm): δ 6.52-6.54 (d, 2H), 6.98-6.99 (d, 2H), 7.07 (s, 2H), 7.22-7.24 (d, 2H), 7.43-7.46 (t, 1H). MS (MALDI-TOF/) m/z: Calcd, 360.9. Found, (M^+), 361.7.

4,7-Dibromo-15-nitro[2.2](2,6)pyridinoparacyclophane-1,9-diene (5b). This was prepared following the general procedure given for the preparation of **5a**. From **4b** (1.61 g, 2.56 mmol) there was obtained **5b** as slight yellow solid (157 mg, 15% yield). ^{1}H NMR ($CDCl_3$, ppm): δ 6.62-6.65 (d, 2H), 7.06 (s, 2H), 7.38-7.40 (d, 2H), 7.69 (s, 2H). MS (MALDI-TOF/) m/z: Calcd, 405.9. Found, (M^+), 406.8.

4,7-Dibromo-15-chloro[2.2](2,6)pyridinoparacyclophane-1,9-diene (5c). This was prepared following the general procedure given for the preparation of **5a**. From **4c** (1.39 g, 2.25mmol) there was obtained **5c** as white solid (134 mg, 15% yield). ^{1}H NMR ($CDCl_3$, ppm): δ 6.45-6.47 (d, 2H), 7.01 (s, 2H), 7.06 (s, 2H), 7.27-7.30 (d, 2H). MS (MALDI-TOF/) m/z: Calcd, 394.9. Found, (M^+), 395.8.

4,7-Dibromo-15-methoxy[2.2](2,6)pyridinoparacyclophane-1,9-diene (5d). This was prepared following the general procedure given for the preparation of **5a**. From **4d** (1.81 g, 2.97 mmol) there was obtained **5d** as white solid (139 mg, 12% yield). ^{1}H NMR ($CDCl_3$, ppm): δ 3.74 (s, 3H), 6.44-6.47 (d, 2H), 6.55 (s, 2H), 7.06 (s, 2H), 7.20-7.22 (d, 2H). MS (MALDI-TOF/) m/z: Calcd, 390.9. Found, (M^+), 391.7.

(2-((4-Bromophenyl)thio)ethyl)trimethylsilane (7). To a high pressure reaction tube was added **6** (1.00 g, 5.30 mmol), vinyltrimethylsilane (0.921 mL, 6.35 mmol), and azobisisobutyronitrile (9 mg, 0.053 mmol). The tube was sealed and the reaction mixture was stirred and heated at 100°C for 20 hours. The mixture was then allowed to cool room temperature and concentrated under

reduced pressure to give **7** as a clear liquid (1.47 g, 95.7% yield). ^{1}H NMR ($CDCl_3$, ppm): δ 0.04 (s, 9H), 0.89-0.93 (m, 2H), 2.91-2.95 (m 2H), 7.15-7.17 (d, 2H), 7.38-7.40 (d, 2H).

Trimethyl(2-((4-(trimethylstannyl)phenyl)thio)ethyl)silane (8). To a solution of **7** (1.47 g, 5.07 mmol) in THF (10 mL) at -78°C under N_2 was added *n*-butyllithium (2.5 M in hexanes) (2.23 mL, 5.58 mmol). After stirring the reaction mixture at -78°C for 2 hours, trimethyltin chloride (1.0 M in hexanes) (5.58 mL, 5.58 mmol) was added to the mixture. The reaction was allowed to gradually warm to room temperature and stirred for 12 hours. The reaction was diluted with ethyl acetate and water. The organic phase was washed with water, dried with $MgSO_4$ and concentrated under reduced pressure to give **8** as slight yellow oil (1.71 g, 90% yield). ^{1}H NMR ($CDCl_3$, ppm): δ 0.04 (s, 9H), 0.28 (s, 9H), 0.92-0.96 (m, 2H), 2.94-2.98 (m 2H), 7.27-7.29 (d, 2H), 7.39-7.41 (d, 2H).

(2-((4'-Bromo-[1,1'-biphenyl]-4-yl)thio)ethyl)trimethylsilane (9). To a round-bottom flask equipped with a condenser was added **8** (1.71 g, 4.58 mmol), 1-bromo-4-iodobenzene (1.56 g, 5.53 mmol), and tetrakis(triphenylphosphine)palladium (266 mg, 5 mmol%). The system was evacuated and refilled with N_2 three times, then charged with toluene (50 mL). The reaction mixture was refluxed at 120°C under N_2 for 16 hours. After cooling to room temperature, the reaction mixture was filtered and concentrated under reduced pressure. Chromatography of the residue over silica gel gave **9** as white solid (954 mg, 57% yield). ^{1}H NMR ($CDCl_3$, ppm): δ 0.06 (s, 9H), 0.94-0.99 (m, 2H), 2.98-3.02 (m 2H), 7.35-7.37 (d, 2H), 7.43-7.49 (q, 4H), 7.54-7.56 (d, 2H).

Trimethyl(2-((4'-(4,4,5,5-tetramethyl-1,3,2-dioxaborolan-2-yl)-[1,1'-biphenyl]-4-yl)thio)ethyl)silane (10). To a round-bottom flask equipped with a condenser was added **9** (1.78 g, 4.87 mmol), bis(pinacolato)diboron (1.48 g, 5.84 mmol), potassium acetate (1.43 g, 14.6 mmol), and [1,1′-Bis(diphenylphosphino)ferrocene]dichloropalladium(II) (238 mg, 6 mmol%). The system was evacuated and refilled with N_2 three time, then charged with dioxane (100 mL). The reaction mixture was bubbled with N_2 for 5 minutes, then refluxed at 100°C under N_2 for 24 hours. After cooling to room temperature, the reaction mixture was filtered and diluted with dichloromethane. The organic phase was washed with water and brine, dried with $MgSO_4$, and concentrated under reduced pressure. Chromatography of the residue over silica gel gave **10** as white solid (1.20 g, 60% yield). ^{1}H NMR ($CDCl_3$, ppm): δ 0.06 (s, 9H), 0.94-0.99 (m, 2H), 2.98-3.02 (m 2H), 7.35-7.37 (d, 2H), 7.43-7.49 (q, 4H), 7.54-7.56 (d, 2H).

PPC-H (11a). To a round-bottom flask equipped with a condenser was added **5a** (7.5 mg, 0.021 mmol), **10** (18.8 mg, 0.046 mmol), tetrakis(triphenylphosphine)palladium (2 mg, 8 mmol%), and Aliquat 336 (0.3 mg, 3 mmol%). The system was evacuated and refilled with N_2 three times, then charged with toluene (0.5 mL). The reaction mixture was heated at 85°C under N_2 for 24 hours. After cooling to room temperature, the reaction mixture was filtered and concentrated under reduced pressure. Chromatography of the residue over silica gel gave **11a** as white solid (5 mg, 31% yield). ^{1}H NMR ($CDCl_3$, ppm): δ 0.05 (s, 18H), 0.94-0.98 (m, 4H), 2.98-3.02 (m, 4H), 6.31-6.34 (d, 2H), 6.77-6.78 (d, 2H), 7.26 (s, 2H), 7.35-7.39 (m, 8H), 7.50-7.53 (m, 11H). MS (MALDI-TOF/) m/z: Calcd, 773.3. Found, (M^+), 774.5.

PPC-NO_2 (11b). This was prepared following the general procedure given for the preparation of **11a**. From **5b** (50 mg, 0.123 mmol) and **10** (111 mg, 0.270 mmol) there was obtained **11b** as slight yellow solid (15 mg, 15% yield). ^{1}H NMR ($CDCl_3$, ppm): δ 0.05 (s, 18H), 0.94-0.98 (m, 4H), 2.98-3.02 (m, 4H), 6.41-6.44 (d, 2H), 7.32 (s, 2H), 7.32-7.37 (m, 8H), 7.49 (s, 2H), 7.51-7.54 (m, 8H), 7.68-7.71 (d, 2H). MS (MALDI-TOF/) m/z: Calcd, 818.3. Found, (M^+), 818.9.

PPC-Cl (11c). This was prepared following the general procedure given for the preparation of **11a**. From **5c** (30 mg, 0.076 mmol) and **10** (68 mg, 0.166mmol) there was obtained **11c** as white solid (9 mg, 15% yield). ^{1}H NMR ($CDCl_3$, ppm): δ 0.06 (s, 18H), 0.94-0.99 (m, 4H), 2.98-3.02 (m, 4H), 6.24-6.26 (d, 2H), 6.80 (s, 2H), 7.30 (s, 2H), 7.35-7.39 (m, 8H), 7.53-7.59 (m, 10H). MS (MALDI-TOF/) m/z: Calcd, 807.3. Found, (M^+), 808.2.

PPC-OCH_3 (11d). This was prepared following the general procedure given for the preparation of **11a**. From **5d** (50 mg, 0.128 mmol) and **10** (116 mg, 0.282 mmol) there was obtained **11d** as white solid (15 mg, 15% yield). ^{1}H NMR ($CDCl_3$, ppm): δ 0.06 (s, 18H), 0.94-0.99 (m, 4H), 2.98-3.02 (m, 4H), 3.69 (s, 3H) 6.24-6.27 (d, 2H), 6.35 (s, 2H), 7.30 (s, 2H), 7.35-7.40 (m, 8H), 7.49-7.55 (m, 10H). MS (MALDI-TOF/) m/z: Calcd, 803.3. Found, (M^+), 803.8.

PPC-$N(CH_3)_2$ (11e). To **11c** (10 mg) in a high pressure reaction tube was added dimethylamine (2.0M in THF) (2 mL). The tube was sealed and the reaction mixture was stirred and heated at 150°C for 24 hours. The reaction mixture was allowed to cool to room temperature and concentrated under reduced pressure to give **11e** as white solid (8 mg). ^{1}H NMR ($CDCl_3$, ppm): δ 0.06 (s, 18H), 0.94-0.99 (m, 4H), 2.98-3.02 (m, 4H), 3.03 (s, 6H) 6.24-6.27 (d, 2H), 6.35 (s, 2H),

7.30 (s, 2H), 7.35-7.40 (m, 8H), 7.49-7.55 (m, 10H). MS (MALDI-TOF/) m/z: Calcd, 816.3. Found, (M^+), 816.6.

STM break-junction sample preparation:

The gold substrates were prepared by thermally evaporating 130 nm of gold (99.999%, Alfa Aesar) on freshly cleaved mica slides (Ted Pella) in an ultra-high vacuum chamber (4×10^{-7} torr), and stored under vacuum. Before each measurement, the gold electrode was annealed briefly with a propane torch to remove any possible contamination and to generate large, atomically flat terraces.

The SAM of the five molecules were prepared in a single step using tetrabutylammonium fluoride (TBAF) as the deprotecting agent under a N_2 protected environment in a tetrahydrofuran (THF) solution containing ca. 5×10^{-5} M of the target molecule. A gold substrate prepared using the procedure described above was immersed in the solution for more than 12 hours. The substrate was then washed successively with THF and ethanol, dried under a stream of N_2, and immediately used for experiment.

STM break-junction experiment:

The experiments were performed with a previously described STM break-junction setup. Briefly, fresh gold tips were prepared by mechanically cutting a 0.25 mm gold wire (99.998% Alfa Aesar). The experiments were carried out in toluene (≥99.9% Sigma-Aldrich), which reduced possible surface contamination. Before use, the STM Teflon solvent holder was sonicated in acetone and dried with N_2. During assemble, the solvent holder was placed over the gold–SAM surface and filled with a couple drops of the solvent. A typical break-junction experiment comprised a total of 2,000–2,500 current–distance traces collected at pulling rates of 10–15 nm/s. Of these traces, 8–

10% displayed plateaus that corresponded to the formation of a molecular bridge and were employed to build the histograms. The break-junction experiments were performed at a bias of 0.1 V. I/V measurements were performed with a previously described method. Construction of the histograms was done following the work by Tao *et. al.*

Energy offsets of the molecular junctions ε_0 are calculated following the work by Baldea, with the equation:

$$|\varepsilon_0| = 2\frac{e|V_{t+}V_{t-}|}{\sqrt{V_{t+}^2 + 10|V_{t+}V_{t-}|/3 + V_{t-}^2}}$$

where V_{t+} is the transition voltage at positive bias, V_{t-} is the transition voltage at negative bias, and *e* is electron charge.

Surface characterization:

Cyclic voltammetry (CV) was performed with Autolab Voltammetric Analyzer in a conventional three-electrode cell. A disc of gold film on mica (prepared as described above) was used as the working electrode. After forming the SAM of the target molecule on the gold substrate (prepared as described above), the surface was immersed in THF and ferrocenoyl chloride was added to react with the free thiol to form ferrocene thioester as a reporting molecule. A platinum wire was used as auxiliary electrode and the potentials were measured against an $Ag/AgNO_3$ electrode in 0.01 M $AgNO_3$. 0.1 M tetrabutylammonium hexafluorophosphate ($TBAPF_6$) in acetonitrile was used as supporting electrolyte. The electrolyte solution was degassed prior to experiment by bubbling N_2 for 10 minutes. All measurements were carried out at ambient conditions.

Surface coverage of the molecule on the gold substrate were determined from the voltammograms recorded according to the equation:

$$\Gamma = \frac{Q_{Fe}}{nFAr}$$

where Q_{Fe} is the charge consumed for the oxidation-reduction process of the ferrocene groups, n is the number of electrons involved in the electron transfer process (n = 1 for ferrocene), A is the geometric surface area of the electrode (0.6362 cm^2), r is the scan rate, and F is the faraday constant. Values of Q_{Fe} were obtained by the integration of the faradaic current peaks from the voltammograms.

FMO calculations:

The molecular geometries of the molecules were optimized, and their orbital energies and charge distributions calculated using the B3LYP DFT function with basis set 6-31G* as implemented in Gaussian 09.

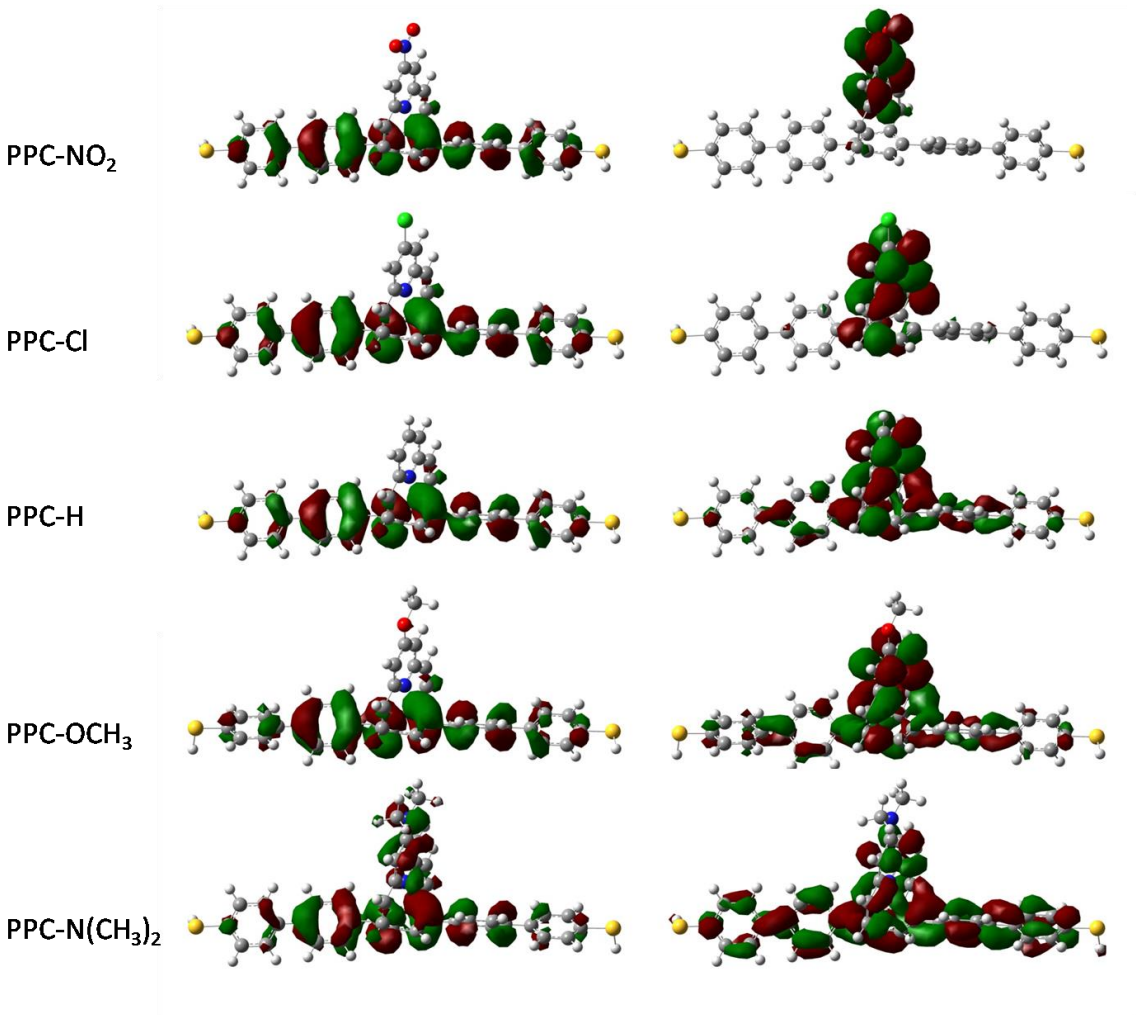

Figure 2.8 Geometries of the frontier molecular orbitals of the five molecules (left HOMO, right LUMO).

2.5 References

(1) Ratner, M. A. *Nat. Nanotechnol.* **2013**, *8*, 378-381.
(2) Ng, M. K.; Yu, L. P. *Angew. Chem. Int. Ed.* **2002**, *41*, 3598-3601.
(3) Ng, M. K.; Lee, D. C.; Yu, L. P. *J. Am. Chem. Soc.* **2002**, *124*, 11862-11863.
(4) Bernasek, S. L. *Angew. Chem., Int. Ed.* **2012**, *51*, 9737-9738.
(5) Venkataraman, L.; Klare, J. E.; Nuckolls, C.; Hybertsen, M. S.; Steigerwald, M. L. *Nature* **2006**, *442*, 904-907.
(6) Liang, W.; Shores, M. P.; Bockrath, M.; Long, J. R.; Park, H. *Nature* **2002**, *417*, 725-729.
(7) Park, H.; Park, J.; Lim, A. K. L.; Anderson, E. H.; Alivisatos, A. P.; McEuen, P. L. *Nat. Commun.* **2000**, *407*, 57-60.

(8) Martel, R.; Schmidt, T.; Shea, H. R.; Hertel, T.; Avouris, P. *Appl. Phys. Lett.* **1998**, *73*, 2447-2449.
(9) Artes, J. M.; Diez-Perez, I.; Gorostiza, P. *Nano Lett* **2012**, *12*, 2679-2684.
(10) Song, H.; Kim, Y.; Jang, Y. H.; Jeong, H.; Reed, M. A.; Lee, T. *Nature* **2009**, *462*, 1039-1043
(11) Baldea, I.; Koppel, H. *Phys. Lett. A* **2012**, *376*, 1472-1476.
(12) Xu, Y. Q.; Fang, C. F.; Cui, B.; Ji, G. M.; Zhai, Y. X.; Liu, D. S. *Appl. Phys. Lett.* **2011**, *99*, 043304.
(13) Olsen, S. T.; Hansen, T.; Mikkelsen, K. V. *Theor. Chem. Acc.* **2011**, *130*, 839-850.
(14) Saha, K. K.; Nikolic, B. K.; Meunier, V.; Lu, W. C.; Bernholc, J. *Phys. Rev. Lett.* **2010**, *105*, 236803.
(15) Mukhopadhyay, S.; Pandey, R. *J. Phys. Chem. C* **2012**, *116*, 4840-4847.
(16) He, H.; Pandey, R.; Karna, S. P. *Nanotechnology* **2008**, *19*, 505203.
(17) Jackel, F.; Watson, M. D.; Mullen, K.; Rabe, J. P. *Phys. Rev. Lett.* **2004**, *92*, 188303.
(18) Weaver, L. H.; Matthews, B. W. *J. Am. Chem. Soc.* **1974**, *96*, 1581-1584.
(19) Boekelheide, V.; Galuszko, K.; Szeto, K. S. *J. Am. Chem. Soc.* **1974**, *96*, 1578-1581.
(21) Diez-Perez, I.; Hihath, J.; Lee, Y.; Yu, L. P.; Adamska, L.; Kozhushner, A.; Oleynik, I. I.; Tao, N. J. *Nat. Chem.* **2009**, *1*, 635-641.
(22) Xu, B.; Tao, N. J. *Science* **2003**, *301*, 1221-1223.
(23) Guo, S. Y.; Hihath, J.; Diez-Perez, I.; Tao, N. J. *J. Am. Chem. Soc.* **2011**, *133*, 19189-19197.
(24) Huang, Z. F.; Chen, F.; D'Agosta, R.; Bennett, P. A.; Di Ventra, M.; Tao, N. J. *Nat. Nanotechnol.* **2007**, *2*, 698-703.
(25) Di Ventra, M.; Pantelides, S. T.; Lang, N. D. *Phys. Rev. Lett.* **2002**, *88*, 046801.
(26) Beebe, J. M.; B., K.; Frisbie, C. D.; Kushmerick, J. G. *ACS Nano* **2008**, *2*, 827-832.
(27) Stern, T. E.; Gossling, B. S.; Fowler, R. H. *Proc. R. Soc. London, Ser. A* **1929**, *124*, 699-723.
(28) Baldea, I. *Phys. Rev. B* **2012**, *85*, 035442.
(29) Reddy, P.; Jang, S.; Segalman, R. A.; Majumdar, A. *Science* **2007**, *315*, 1568-1571.
(30) Venkataraman, L.; Park, Y. S.; Whalley, A. C.; Nuckolls, C.; Hybertsen, M. S.; Steigerwald, M. L. *Nano Lett* **2007**, *7*, 502-506.
(31) Zotti, L. A.; Kirchner, T.; Cuevas, J.; Pauly, F.; Huhn, T.; Scheer, E.; Erbe, A. *Small* **2010**, *6*, 1529-1535.
(32) Xiao, X.; Nagahara, L. A.; Rawlett, A. M.; Tao, N. *J. Am. Chem. Soc.* **2005**, *127*, 9235-9240.
(33) Hammett, L. P. *Chem. Rev.* **1935**, *17*, 125-136.

CHAPTER 3

PROTON-TRIGGERED SWITCH BASED ON MOLECULAR WIRE WITH EDGE-ON GATE

This chapter contains parts of the published work [Li, L.; Lo, W.-Y.; Cai, Z. *et al. Chem. Sci.* **2016**, *7*, 3137-3141] The Royal Society of Chemistry.

3.1 Introduction and Background

As mentioned in Chapter 1, variation of molecular structures, either electronic or geometric changes, can exert a profound effect on electric conductance of single molecular wires. For example, meta- or para-position of connection will lead to different electric conductance; introduction of dipole into single molecules can render the molecules rectification property.[1-3] In addition to these intrinsic structural changes, a continuing interest in molecular electronics is to build devices integrating molecules whose conductivity can be manipulated by external stimuli such as pH values of environmental solution,[2, 4] light,[5] mechanical motion,[6] temperature,[7] magnetic field,[8] or electric field.[9-16] For example in the previous chapter, we have demonstrated the concept of edge-on gating at the molecular level with a set of single molecular wires, which contain the 2.2(2,6)pyridinoparacyclophane-l,9-diene (PPC) moiety (Figure 3.1a).[17] In this system, we took the advantage of the perpendicular orientation between the two aromatic planes and used the pyridine end of the moiety as the gating part of the wire attached with function groups of different electronic demands.[18, 19] Further studies by scanning tunneling microscopy break-junction (STM-BJ) technique demonstrated that the single-molecule conductance, the orbital energy level, as well as the charge tunneling barrier of these molecular wires can be tuned by changing the electronic

property of the gating substituent group. The collective behavior of these compounds resembles that of field effect transistors when the functional group changes from strong electron acceptors to strong electron donors.

An important function of transistor is their switching behavior, which is the basis of modern computing mechanism. The function of switch "on" and "off" corresponds to binary information of "0" and "1". In this study, we report an on/off switch based on a molecular wire containing the edge-on pyridinoparacyclophane moiety, triggered by the protonation of the pyridine ring. The results reveal that the protonation/deprotonation processes on the nitrogen atom of the edge-on pyridine ring can reversibly alter the electrical property of the molecular wire, leading to a binary system.

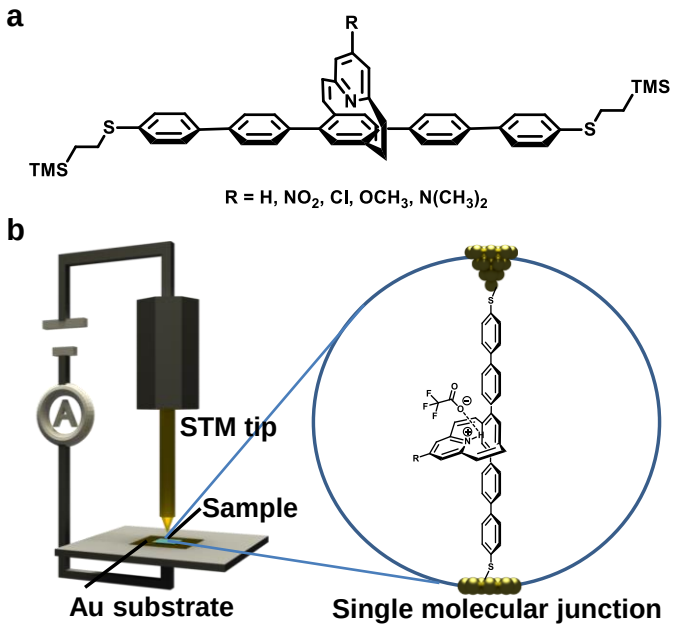

Figure 3.1 Experimental setup. (a) Chemical structure of the PPC-based molecular wires. (b) A representation of metal-molecule-metal junction in the STM-BJ technique.

3.2 Sample Characterizations and STM Break-Junction Experiments

Detailed synthesis and characterization of these PPC-molecular wires with gating pyridinyl moiety whose para-position are functionalized with groups -NO_2, -Cl, -H, -OCH_3, and -$N(CH_3)_2$ were described in the previous chapter.[17] The pyridinoparacyclophane unit was shown to be similar to other pyridine derivatives that can be protonated by strong acid.[18,20, 21] To measure the conductance of single molecules, self-assembled monolayer (SAM) films of the deprotected thiol molecules were prepared on gold surface via thiol-gold binding chemistry. The resulting SAM was further treated with trifluoroacetic acid (TFA) (100 mM in degassed THF) to protonate the SAM for conductance measurements, and then with Na_2CO_3 solution (100 mM in a degassed water/acetonitrile (v/v, 1/1) mixture) to obtain deprotonated assembly. Details of the preparation of SAMs can be found in the supporting information. Successful immobilization of these molecular wires onto gold substrates was confirmed by the CV measurements[17] and the XPS characterization (Figure 3.2), and further supported by the variation of the contact angles of these modified surfaces compared with bare gold surface (Figure 3.3). Specifically, XPS studies indicated that the C/S ratio for PPC-OCH_3 SAM before treated with TFA was 40.0/2.3, in agreement with the theoretical ratio of 40.0/2.0. An extra signal of fluorine was detected for TFA-treated PPC-OCH_3 SAM, demonstrating the success of the protonation process.

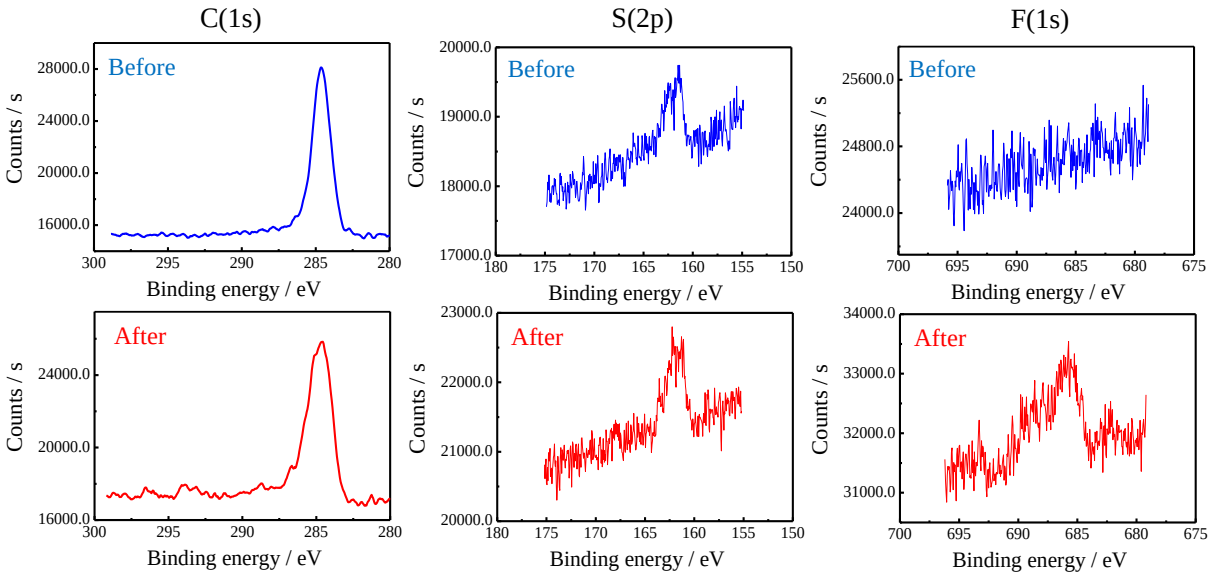

Figure 3.2 XPS characterization of elements C, S and F of PPC-OCH_3 self-assembled monolayer before and after treated with TFA.

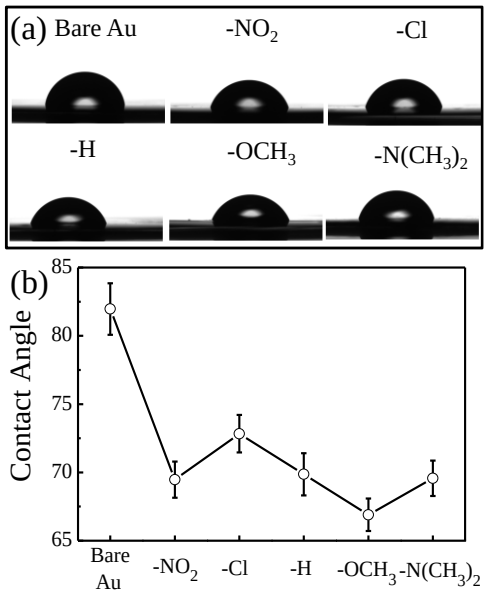

Figure 3.3 (a) Photographs of water droplets on the PPC-based self-assembled monolayers (SAMs). (b) Statistical average values of the contact angle of the PPC-based self-assembled monolayers (SAMs), where 3 individual measurements were carried out to extract the average contact angle.

3.2.1 Single-Molecule Conductance Switch

The single-molecule conductance was measured by the break-junction technique with a modified STM system.[13, 22, 23] The experiments were carried out at a small bias voltage of 100 mV in degassed toluene.[22] The conductance traces of the molecular junctions with different substituent were recorded by using a LabVIEW program. Figure 3.4a shows the typical conductance-distance curves for the protonated single molecular junctions with different functional groups. The plateaus of constant conductance observed in these stretching traces around ~ 10^{-5} G_0 represent the signature of single molecule junction, where G_0 is the quantum of conductance $2e^2/h$ (e is the electron charge and h is the Plank constant). The plateau length is generally around 0.5-1.0 nm. The fluctuation of the conductance value below 10^{-6} G_0 is originated from the noise floor. Repeated measurements gave a statistical assessment of the junction properties. Figure 3.4b shows the corresponding conductance histograms generated from 300 ~ 500 effective conductance decay curves. The histogram reveals an unambiguous peak for all of the molecules measured. By fitting these peaks to a Gaussian function, we can determine the most probable conductance value for the junctions. More specifically, the values of single molecule conductance of the protonated molecules PPC-NO_2, PPC-Cl, PPC-H, PPC-OCH_3, and PPC-$N(CH_3)_2$ at 100 mV of bias voltage were determined to be 6.3×10^{-6} G_0, 5.6×10^{-6} G_0, 6.0×10^{-6} G_0, 5.5×10^{-6} G_0, and 5.4×10^{-6} G_0 respectively. These results clearly indicated that the protonated molecules exhibit similar conductance, independent of the nature of substituent on pyridine ring. The conductance values of protonated molecules are almost identical to that of unprotonated, nitro-substituted compound. It shows that the positive charge on protonated pyridinyl moiety suppressed charge transport and acted as a switch.

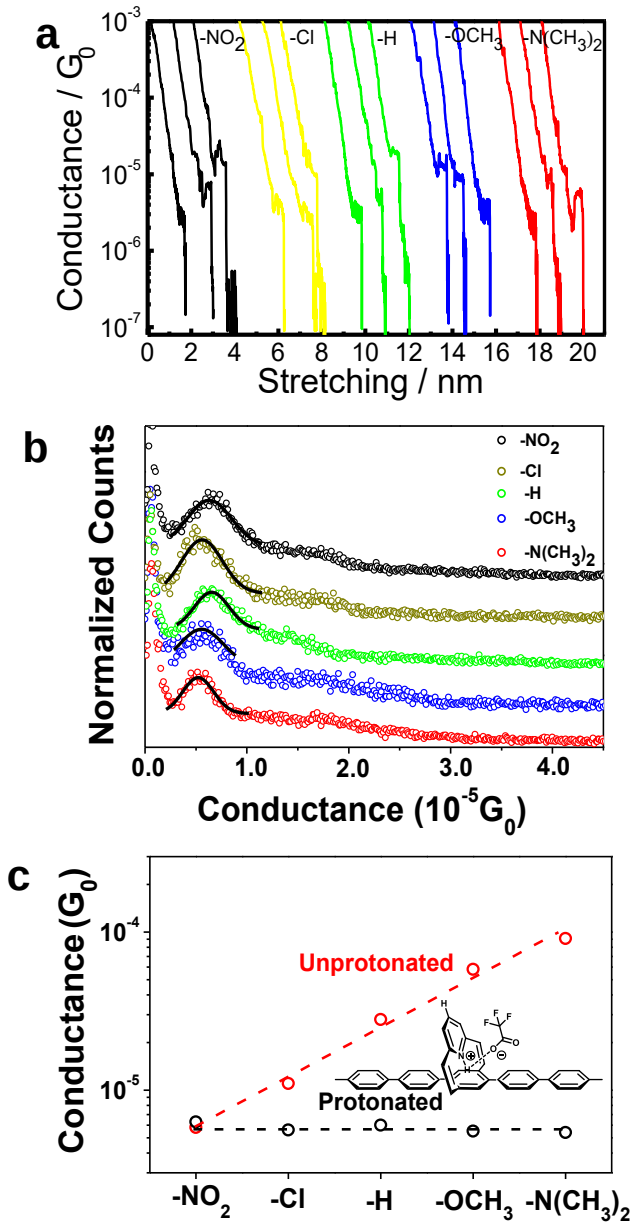

Figure 3.4 Conductance of protonated molecular junctions. (a) Representative conductance-distance traces of the protonated molecular wires with different substituent. (b) Conductance histograms of the five protonated molecular wires, where the black solid lines represent the Gaussian fitting curves. (c) The most probable conductance values of the unprotonated and protonated molecular wires. Dotted lines are only used as eye guide.

As mentioned in the above section, XPS studies indicated the presence of fluorine atoms in the monolayer assembly, an evidence for the protonation by TFA. To further ensure that the observed difference of conductance values is due to the effect of protonation, spectroscopic studies were carried out in solution state. The ^{1}H-NMR studies showed that chemical shifts of all protons of PPC-based molecules shift to lower field after protonation, which was caused by the enhanced de-shielding effect of the pyridinium compared with the neutral pyridine ring. The UV-vis spectra showed that the absorption maxima of these PPC-based molecules exhibits a bathochromic shift after TFA protonation, and the shift enhances as the substituent group changes from electron-withdrawing to electron-donating group (Figure 3.5). It is interesting to note that the protonation of PPC-NO_2 and PPC-Cl molecules did not lead to obvious bathochromic shift, which is consistent with the conductance results, where all of the conductance values fall to the level of the nitro-substituted compound. The DFT calculation discussed below indicated that the protonation affects LUMO more than HOMO orbitals unless the pyridine ring is substituted with electron deficient groups.

The effect of protonation process on the conductance of molecular wires was shown to be reversible after the protonated SAM was treated with Na_2CO_3 solution in a water/acetonitrile mixture. The conductance histograms of the unprotonated, protonated and deprotonated PPC-NO_2, PPC-H and PPC-$N(CH_3)_2$ molecular junctions are shown in Figure 3.6. Figure 3.7a summarizes the corresponding most probable conductance values, and the results clearly demonstrate the deprotonation of the nitrogen atom of pyridine ring successfully restore the conductance of neutral PPC-based molecules. The reversible features of the protonation/deprotonation process were consistent with spectroscopic observation (Figure 3.7b).

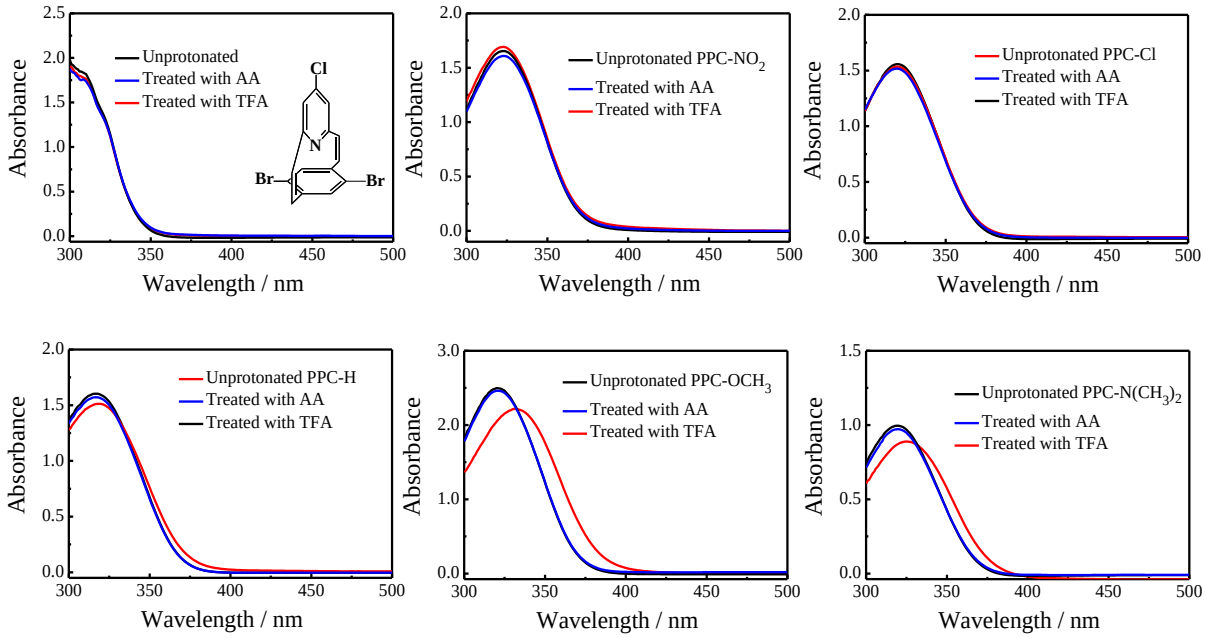

Figure 3.5 UV-vis spectra of the PPC-based molecules treated by TFA and AA.

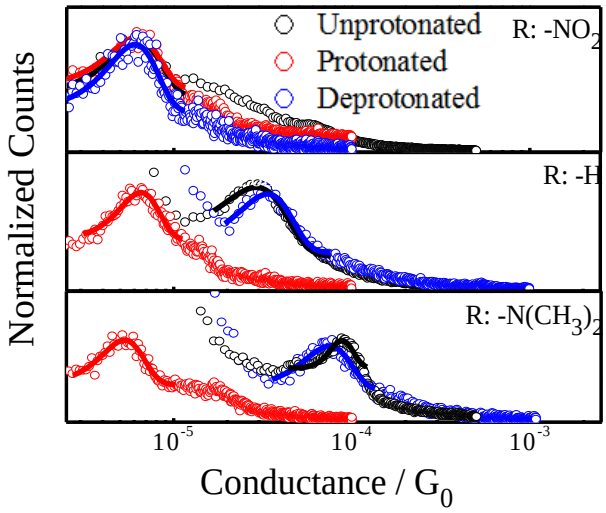

Figure 3.6 Conductance histograms of the unprotonated, protonated and deprotonated molecular wires with different substituents (R): -NO_2, -H, and -$N(CH_3)_2$.

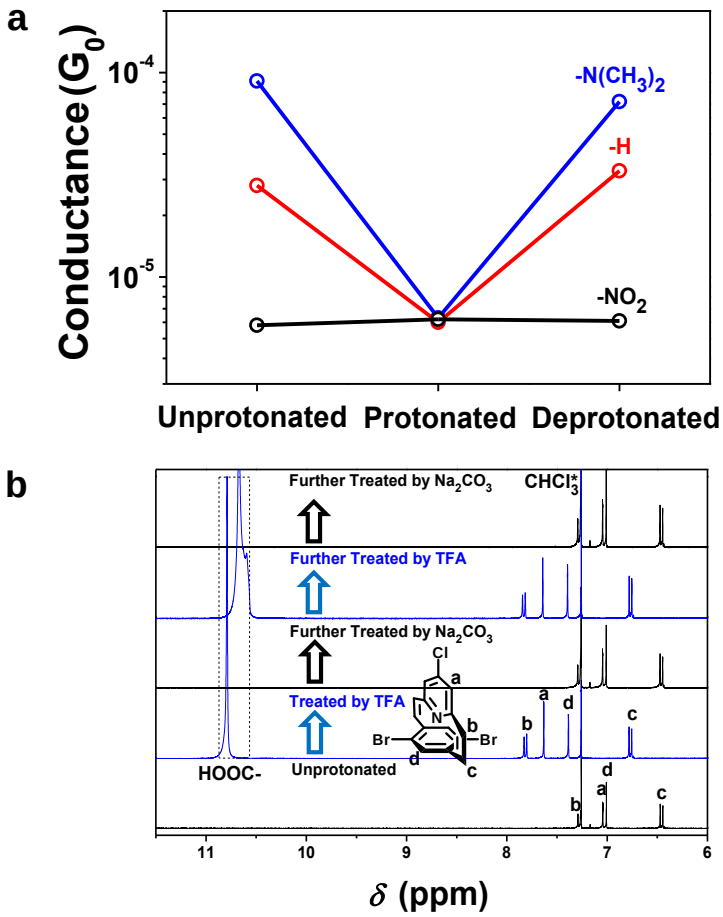

Figure 3.7 Reversible change in conductance and chemical shift due to protonation. (a) The corresponding most probable conductance values of the unprotonated, protonated and deprotonated molecular wires. (b) 1H-NMR spectra of PPC-Cl core of the protonation/deprotonation cycles.

The contact angle measurements showed no significant difference between the untreated SAM, and the SAMs treated by TFA and Na_2CO_3. This is reasonable because the wetting property of SAM is mainly dominated by the outermost functional group, i.e., thiol group in our case, instead of the pyridine ring hidden in the interior.

The protonation effect is further demonstrated by the inability of weak acid in changing the conductance. The pyridine moiety cannot be protonated by acetic acid, a weak acid, with a pK_a

value ~ 4.75. Thus, when the SAMs were treated with acetic acid, no difference in conductance can be detected in break-junction measurements before and after protonation. Similar phenomenon was observed in all other experiments including the ^{1}H-NMR spectra and UV-vis spectra.

3.2.2 Single-Molecule Current-Voltage Characteristics

The current−voltage (*I-V*), conductance-voltage (*G-V*) characteristics, and the related transition voltage spectroscopy (*TVS*) were obtained to further probe the charge transport mechanism in the protonated molecular junctions. Figure 3.8a and e plot ca. 800 *I-V* curves for unprotonated and protonated PPC-H molecular junctions. The incomplete *I-V* curves constituting ~70% of all the curves due to the breakdown and instability of the molecular junctions were automatically detected and not included in the *I-V* histogram shown in Figure 3.8. Typically, most of the initial slopes of the *I-V* curves for the protonated PPC-H molecular junction are smaller than that for the unprotonated version, consistent with the observed trend of the previous conductance histograms. The *I-V* and *G-V* histograms for other molecules are summarized in Figure 3.9. Most of the *I-V* curves display a clear nonlinearity as a function of bias voltage, which was also reflected in the corresponding bowl-shaped 2-D *G-V* histograms (Figure 3.8b and f).

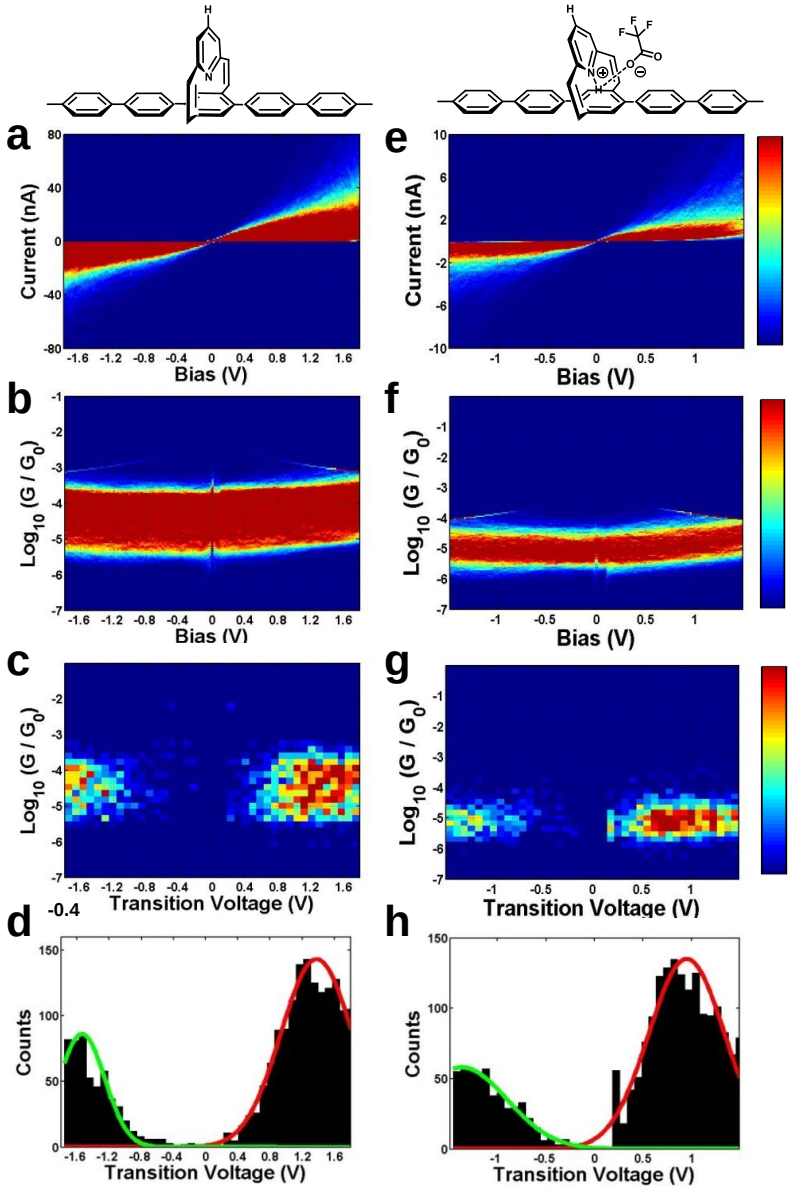

Figure 3.8 Change in electrical properties due to protonation. 2-D *I-V* histograms, 2-D *G-V* histograms, 2-D transition voltage histograms, and 1-D transition voltage histograms for unprotonated (left column: a, b, c, d)[17] and protonated (right column: e, f, g, h) PPC-H molecular junctions, respectively.

The single-molecule *TVS* was obtained by converting each *I-V* curve into curve of $\ln(I/V^2)$ as a function of $1/V$, the so-called Fowler-Nordheim (FN) plot.[23-26] The minimum of the FN plot corresponds to the transition voltage V_t and the 1D TVS histograms of the occurrence of the

transition voltage can be constructed from these minimum values. The *TVS* plot of octanedithiol was constructed as a control experiment. The result indicates that the measured V_t for octanedithiol is ~ 1.35 V, which is consistent with the reported values (1.30 V ~ 1.40 V) in the literatures.[23, 27] As shown in Figure 3.8d and h, the transition voltage histograms of the unprotonated and protonated PPC-H molecules exhibit two distinguished characteristics: (1) both histograms are asymmetric in nature; (2) the absolute values of the measured positive and negative transition voltages (V_{t+} and V_{t-}) decrease from 1.35 V to 0.95 V and 1.51 V to 1.35 V, respectively, after protonation. The asymmetry of the transition voltage histogram for molecular junctions was previously observed in the work of Kushmerick[24] and Tao[23]. The phenomenon was mainly attributed to the metal-molecule contacts and the symmetry of the molecule itself, namely, the flat substrate electrode versus the sharp tip electrode and the stronger coupling of the π-electrons of the aromatic rings to the flat substrate than to the atomically sharp tip. Most recently, it was shown that polarity of solvent can also cause the asymmetry.[28]

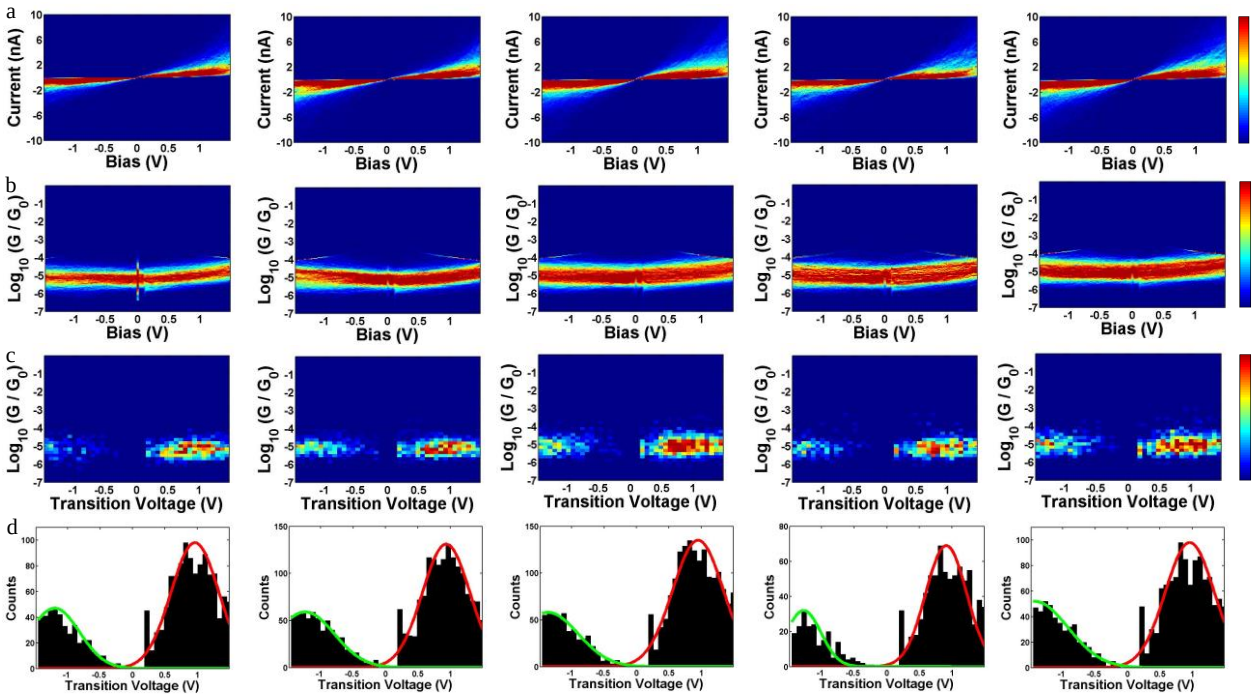

Figure 3.9 (a) Current-voltage 2D histograms, (b) conductance-voltage 2D histograms, (c) transition voltage 2D histograms, and (d) transition voltage 1D histograms of the protonated PPC molecular junctions with substituents -NO_2, -Cl, -H, -OMe, -$N(Me)_2$ (from left to right), respectively.

3.2.3 Transition Voltage Spectroscopy Analysis

Since the applied bias V can affect the energy offset between Fermi level of electrodes and molecular orbitals, $\varphi_0 \equiv \varphi_0(V)|_{V=0} \rightarrow \varphi_0(\mathrm{V})$, voltage division factor γ was designed to account for this effect, where $\varphi_0(V) = \varphi_0 + \gamma\, eV$.[29, 30] More specifically, the experimentally measured transition voltages $V_{t\pm}$ for both bias polarities are related to the barrier height φ_0 and the voltage division factor γ based on the equations developed by Bâldea.[29, 30] The calculated values for the unprotonated and the protonated PPC molecular wires are summarized in Figure 3.10 and Supplementary Table S2. As shown in Figure 3.10a, all the calculated γ values are positive, indicating that the potential drop at the soft contact (e.g., STM-tip) is slightly larger. Moreover, the γ values of the protonated molecular wires are larger than those of the unprotonated molecular

wires. This implies that protonation changes the symmetry of the molecular structure, thus affects the interfacial potential drops. Figure 3.10b shows a comparison of the calculated energy offsets of the molecular wires before and after protonation. We can see that protonation converts the φ_0 value of different molecules to the same value within the experimental uncertainty. This is consistent with the observed trend of conductance value, demonstrating that the protonation indeed functions as a switch by changing the energy levels. Our previous study[17] showed that the tunneling barrier of the unprotonated PPC-molecular wires followed the order: φ_0(-Cl)>φ_0(-H)>φ_0(-OCH_3)>φ_0(N(-CH_3)$_2$), which agreed well with the observed order of conductance: G(-Cl)<G(-H)<G(-OCH_3)<G(N(-CH_3)$_2$). This was attributed to the modulation of the charge tunneling barriers of the pentaphenylene wire via the pyridine unit, acting like gate electrode. Since the pentaphenylene unit is a *p*-type semiconductor, the measured φ_0 reflects the $E_F - E_{HOMO}$ offset. However, for the unprotonated PPC-NO_2, its conductance was observed to be the lowest among the neutral compounds while its tunneling barrier was also the lowest. We attributed the cause of this phenomenon to a switch of transport mechanism by tunneling through the LUMO due to strong electron withdrawing ability of nitro group. The DFT calculation supported this explanation.[17] The results in this study indicate that the effect of protonation is the same as for nitro groups. The positive charge in the pyridine ring converted the molecular wire into n-type semiconductor. The charges are tunneled through the LUMO energy level. This mechanistic change in charge tunneling is the origin of the switching behavior.

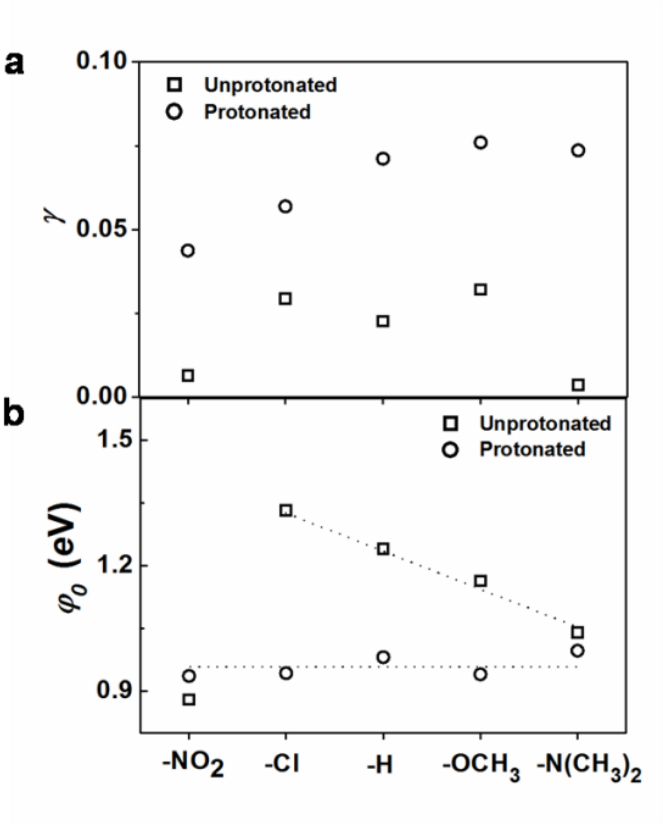

Figure 3.10 Transition voltage analysis. Calculated voltage division factor (γ) (a) and energy offset (φ_0) (b) of unprotonated and protonated PPC-NO_2, PPC-Cl, PPC-H, PPC-OCH_3 and PPC-$N(CH_3)_2$ molecular junctions.

3.3 Conclusion

The protonation effect observed in this work is different from those molecules in which the pyridine ring is a component along the charge transport pathway in molecular wire.[2, 4] In this system, the pyridine ring is orthogonal to the conjugated system in molecular wire. The effect of protonation is akin to a gating voltage, demonstrating that the molecular system reported here will be a genuine transistor if it can be connected to three electrodes.

The influence of protonation on the edge-on gating effect of a series of novel pyridinocyclophane moiety-based molecular junctions was investigated. It was found that the

protonation on the nitrogen atom of the edge-on pyridine ring can reversibly change the conductance of the molecular wires and act as a switch. Protonation converted a molecular wire from p-type to n-type semiconductor. The switch mechanism is thus attributed to the change in charge tunnelling channels from HOMO in neutral molecules to LUMO in protonated ones.

3.4 Experimental Section

Preparation of self-assembled monolayers (SAMs):

Prior to each experiment, the substrate was briefly annealed in a propane flame. The self-assembled monolayers (SAMs) of the five molecules were prepared in a single step using tetrabutylammonium fluoride (TBAF) as the deprotecting agent under a N_2 protected environment in a tetrahydrofuran (THF) solution containing ca. 5×10^{-5} M of the target molecule. A gold substrate prepared using the procedure described above was immersed in the solution for 12 hours. For the measurement of the unprotonated samples, the substrate was then washed successively with THF and ethanol, dried under a stream of N_2, and immediately used for experiment. For the measurement of the protonated samples, the substrate was further submerged in a solution of trifluoroacetic acid (TFA) 100 mM in THF for 15 min, subsequently washed with THF and then dried under a stream of N_2, and immediately used for experiment. For the measurement of the deprotonated samples, the protonated substrate was washed with THF and distilled water, and then was further submerged in 100 mM Na_2CO_3 water/acetonitrile (v/v, 5/5) solution for 15 min, subsequently washed with water, THF and then dried under a stream of N_2, and immediately used for experiment.

Break-junction experiment for single molecule junctions:

The STM-BJ experiments were performed with a previously described STM break-junction setup. Briefly, fresh gold tips were prepared by mechanically cutting a 0.25 mm gold wire (99.998% Alfa Aesar). The experiments were carried out in degassed toluene (≥99.9% Sigma-Aldrich), which reduced possible surface contamination. Before use, the STM Teflon solvent holder was sonicated in acetone and dried with N_2. During measurement, the solvent holder was placed over the gold–SAM surface and filled with a couple drops of toluene. A typical break-junction experiment comprised thousands of current–distance traces. Of these traces, ~ 30% (300 ~ 500 effective curves) displayed plateaus that corresponded to the formation of a molecular bridge and were employed to build the histograms. The break-junction experiments were performed at a bias of 100 mV.

***I-V* recording for single molecule junctions:**

The *I-V* recording experiments were carried out at 100 mV of bias voltage in toluene. Positive bias means that the substrate is positive and the tip negative. The entire process consists of iterations of three steps, tapping, conductance step detection and *I-V* recording, which is in contrast to the single-step tapping procedure used in the STM break junction measurements. In the tapping step, the tip is moved towards the substrate until the current reaches a preset threshold, and then is retracted until it reaches a lower preset current. In the present method, the conductance step detection is applied during each retraction cycle to identify conductance steps. The measured conductance range was selected according to the previously measured conductance histogram of each molecule. Once a conductance step is detected, the *I-V* recording step is activated, which involves the following sub-steps: 1) The tip is immediately held in position, 2) the current -voltage curve was recorded from + 1.5 V to – 1.5 V quickly (10 Hz), 3) upon completion of the *I-V* curve,

the tip was pulled away from the substrate until the current drop to a preset value, and the measurement started over again. For the data selection, *I-V* curves that are incomplete or contain large switching noises are detected and removed from statistical analysis. This procedure allowed us to obtain complete *I-V* curves for statistical analysis.

Energy offsets φ_0 and voltage division factor γ of the molecular junctions are calculated following the work by Baldea, with the equation:

$$\varphi_0 = 2\frac{e|V_{t+}V_{t-}|}{\sqrt{V_{t+}^2 + 10|V_{t+}V_{t-}|/3 + V_{t-}^2}}$$

$$\gamma = -\frac{1}{2}\frac{V_{t+} + V_{t-}}{\sqrt{V_{t+}^2 + 10|V_{t+}V_{t-}|/3 + V_{t-}^2}}$$

Other characterizations:

The contact angle measurements were performed using a KSV (Helsinki, Finland) CAM 200 contact angle goniometer. The X-ray photoelectron spectroscopy (XPS) measurements were conducted on an ESCALAB-250 spectrometer using a monochromatic Al Kα (1486.6 eV) as radiation source. The ultraviolet absorption spectra were recorded by a UV-vis spectrometer, and the scan range was set from 300 nm to 500 nm.^{1}H nuclear magnetic resonance (^{1}H NMR) spectra were recorded on a Bruker AV400 spectrometer by using deuterated chloroform ($CDCl_3$) as solvent and tetramethylsilane (TMS) as an internal standard. For the protonation/deprotonation cycle measurement: 1) ~ 4 mg of PPC-Cl sample was first dissolved in 1 mL of $CDCl_3$ for the ^{1}H NMR measurement; 2) the solution was further added ~15 μL of TFA/AA for the ^{1}H NMR measurement; 3) the solution was further added an excess of anhydrous Na_2CO_3 powder and stirred for 10 min, after filtrated with a 220 nm PVDF filter to remove the inorganic salt, the clear solution

was used for the ^{1}H NMR measurement; 4) steps 2 and 3 were repeated one more time to finish the whole cycle measurement.

3.5 References

(1) Jiang, P.; Morales, G. M.; You, W.; Yu, L. *Angew. Chem. Int. Edit.* **2004**, *43*, 4471-4475.
(2) Morales, G. M.; Jiang, P.; Yuan, S. W.; Lee, Y. G.; Sanchez, A.; You, W.; Yu, L. P. *J. Am. Chem. Soc.* **2005**, *127*, 10456-10457.
(3) Ng, M.-K.; Lee, D.-C.; Yu, L. *J. Am. Chem. Soc.* **2002**, *124*, 11862-11863.
(4) Xiao, X.; Xu, B.; Tao, N. *J. Am. Chem. Soc.* **2004**, *126*, 5370-5371.
(5) Roldan, D.; Kaliginedi, V.; Cobo, S.; Kolivoska, V.; Bucher, C.; Hong, W.; Royal, G.; Wandlowski, T. *J. Am. Chem. Soc.* **2013**, *135*, 5974-5977.
(6) Quek, S. Y.; Kamenetska, M.; Steigerwald, M. L.; Choi, H. J.; Louie, S. G.; Hybertsen, M. S.; Neaton, J. B.; Venkataraman, L. *Nat. Nanotechnol.* **2009**, *4*, 230-234.
(7) Zhao, X.; Huang, C.; Gulcur, M.; Batsanov, A. S.; Baghernejad, M.; Hong, W.; Bryce, M. R.; Wandlowski, T. *Chem. Mater.* **2013**, *25*, 4340-4347.
(8) Jo, M.-H.; Grose, J. E.; Baheti, K.; Deshmukh, M. M.; Sokol, J. J.; Rumberger, E. M.; Hendrickson, D. N.; Long, J. R.; Park, H.; Ralph, D. C. *Nano Lett* **2006**, *6*, 2014-2020.
(9) Tans, S. J.; Verschueren, A. R. M.; Dekker, C. *Nature* **1998**, *393*, 49-52.
(10) Di Ventra, M.; Pantelides, S. T.; Lang, N. D. *Appl. Phys. Lett.* **2000**, *76*, 3448-3450.
(11) Cui, Y.; Lieber, C. M. *Science* **2001**, *291*, 851-853.
(12) Jiao, L. Y.; Zhang, L.; Wang, X. R.; Diankov, G.; Dai, H. J. *Nature* **2009**, *458*, 877-880.
(13) Díez-Pérez, I.; Hihath, J.; Lee, Y.; Yu, L.; Adamska, L.; Kozhushner, M. A.; Oleynik, I. I.; Tao, N. *Nat. Chem.* **2009**, *1*, 635-641.
(14) Ioffe, Z.; Shamai, T.; Ophir, A.; Noy, G.; Yutsis, I.; Kfir, K.; Cheshnovsky, O.; Selzer, Y. *Nat. Nanotechnol.* **2008**, *3*, 727-732.
(15) Perrin, M. L.; Prins, F.; Martin, C. A.; Shaikh, A. J.; Eelkema, R.; van Esch, J. H.; Briza, T.; Kaplanek, R.; Kral, V.; van Ruitenbeek, J. M.; van der Zant, H. S. J.; Dulić, D. *Angew. Chem. Int. Edit.* **2011**, *50*, 11223-11226.
(16) Widawsky, J. R.; Chen, W.; Vázquez, H.; Kim, T.; Breslow, R.; Hybertsen, M. S.; Venkataraman, L. *Nano Lett* **2013**, *13*, 2889-2894.
(17) Lo, W.-Y.; Bi, W.; Li, L.; Jung, I. H.; Yu, L. *Nano Lett* **2015**, *15*, 958-962.
(18) Boekelheide, V.; Galuszko, K.; Szeto, K. S. *J. Am. Chem. Soc.* **1974**, *96*, 1578-1581.
(19) Boekelheide, V.; Tsai, C. H. *Tetrahedron* **1976**, *32*, 423-425.
(20) Barrow, G. M. *J. Am. Chem. Soc.* **1956**, *78*, 5802-5806.
(21) Golubev, N. S.; Smirnov, S. N.; Gindin, V. A.; Denisov, G. S.; Benedict, H.; Limbach, H.-H. *J. Am. Chem. Soc.* **1994**, *116*, 12055-12056.
(22) Xu, B.; Tao, N. J. *Science* **2003**, *301*, 1221-1223.
(23) Guo, S. Y.; Hihath, J.; Diez-Perez, I.; Tao, N. J. *J. Am. Chem. Soc.* **2011**, *133*, 19189-19197.
(24) Beebe, J. M.; Kim, B.; Gadzuk, J. W.; Daniel Frisbie, C.; Kushmerick, J. G. *Phys. Rev. Lett.* **2006**, *97*, 026801.
(25) Huisman, E. H.; Guédon, C. M.; van Wees, B. J.; van der Molen, S. J. *Nano Lett* **2009**, *9*, 3909-3913.

(26) Stern, T. E.; Gossling, B. S.; Fowler, R. H. *Proc. R. Soc. Lon. Ser-A.* **1929**, *124*, 699-723.
(27) Beebe, J. M.; Kim, B.; Frisbie, C. D.; Kushmerick, J. G. *ACS Nano* **2008**, *2*, 827-832.
(28) Capozzi, B.; Xia, J.; Adak, O.; Dell, E. J.; Liu, Z.-F.; Taylor, J. C.; Neaton, J. B.; Campos, L. M.; Venkataraman, L. *Nat Nano* **2015**, *10*, 522-527.
(29) Bâldea, I. *Chem. Phys.* **2012**, *400*, 65-71.
(30) Bâldea, I. *Phys. Rev. B* **2012**, *85*, 035442.

CHAPTER 4

MOLECULAR RECTIFICATION TUNED BY THROUGH-SPACE GATING EFFECT

4.1 Introduction and Background

The control of charge transport in single molecular electronic junction is critical for the construction of complex molecular circuitries.[1-3] Molecular diode provides access to basic functions including rectification, switches[4-6] and transistors.[7] Aviram and Ratner (AR) first proposed theoretically that rectification effect in molecular scale is possible with donor acceptor systems.[8] The general structure of an AR diode consists of a donor block electronically decoupled by an σ bridge from an acceptor block. However, the incorporation of σ bond decreases the conductance of the molecular wires, limiting the length of the molecular junction and the potential complex functions that can be introduced. Inspired by the p/n junction structure in semiconductors, we proposed and demonstrated the concept of p/n junction in molecular diodes.[9-12] The molecular rectification is induced by the dipole of the molecular core.[9-12] Rectification can also come from asymmetric anchoring groups, which induce asymmetric bond dipole.[13] Other effects that changes rectification including protonation,[11] environmental effects,[14] and the introduction of charged host.[15] All these diodes involve changes in the molecular backbone, thus leading to dramatic changes of charge transfer properties. Inspired by nature where proteins regulate the electron transfer using through-space amino acid residue,[16] this chapter describes synthesis and investigation of a gated molecular diode system, in which a change in electronic structure through-space would result in the fine tuning of the electronic structures of the backbone, leading to the control of the rectification behavior.

The diode molecules consist of the cyclophane moiety as the bridging group between the p-type biphenyl unit and the n-type bipyrimidinyl unit. Recently, we found the incorporation of a pyridinocyclophane unit in the molecular backbone effectively tune the conductance via non-conjugating spatial electronic effect.[17] The substitution group of pyridinocyclophane acts as an effective gate electrode that control the conductance of a series of molecular wires. Moreover, this through-space effect can switch off the charge transport through molecular wire via protonation of the nitrogen atom in the pyridine moiety.[18] Combination of the through-space edge-on gating effect and p/n type diode construction enabled us to demonstrate the cyclophane gating effect in molecular diodes.

We have synthesized five molecular diodes with functional groups of varying electronic properties at the gating position. The five functional groups, namely NO_2, Cl, H, OCH_3 and $N(CH_3)_2$, are used as chemical gates to tune the electrical properties of the molecular wire. The two ends of the molecular wires are functionalized with thiol groups with asymmetric protecting groups: trimethylsilylethyl (TMSE) and cyanoethyl (CNE), to allow for sequential deprotection during the self-assembly process so that the orientation of the diodes immobilized on the Au surface was controlled.[11, 12] The structure and the orientation of the five molecular diode assemblies is shown in Figure 4.1.

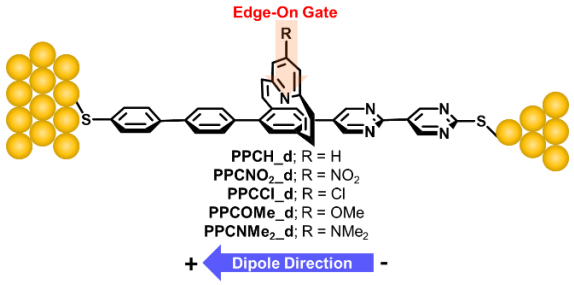

Figure 4.1 Assembly of pyridinoparacyclophane based diodes with edge-on gates on Au surface.

4.2 Sample Characterizations and STM Break-Junction Experiments

The synthesis and characterizations of these diode molecules can be found in the supporting information. Self-assembled monolayer (SAM) films of the deprotected thiol molecules were prepared in order to measure their single-molecule electrical properties. Details of the SAM preparation can be found in the supporting information. The low bias single-molecule conductance was determined by the break-junction technique with a modified STM system. The experiments were carried out at a positive bias voltage of 100 mV in degassed mesitylene. As the STM tip retracts from the surface, plateaus can be observed in the conductance-distance trace, which indicated the formation of single molecule junctions. This tapping motion was performed repeatedly to give a statistical evaluation of the junction properties. From the break-junction experiment, the single-molecule conductance of these molecules were found to be ca. 1 to 7×10^{-5} G_0 (SI Table 1), where G_0 is $2e^2/h$ (e is the charge of electron and h is the Planck constant), depending on the nature of the gating group.

4.2.1 Current-Voltage Characteristics of Gated Diodes

To study the rectification behavior of these diode molecules, the current-voltage (*I-V*) characteristics of these molecular junctions were investigated. During the retraction phase, the Au tip of the STM probe head was briefly held in the position at the detection of plateau in the conductance-distance curve, an indication of the formation of a single-molecule junction. A voltage sweep between 1.8 V and -1.8 V was performed at this point to obtain the individual *I-V* characteristics. Similar to the measurement of conductance, this process was performed repeatedly to compile an *I-V* histogram. The 2D histograms are shown in Figure 4.2.

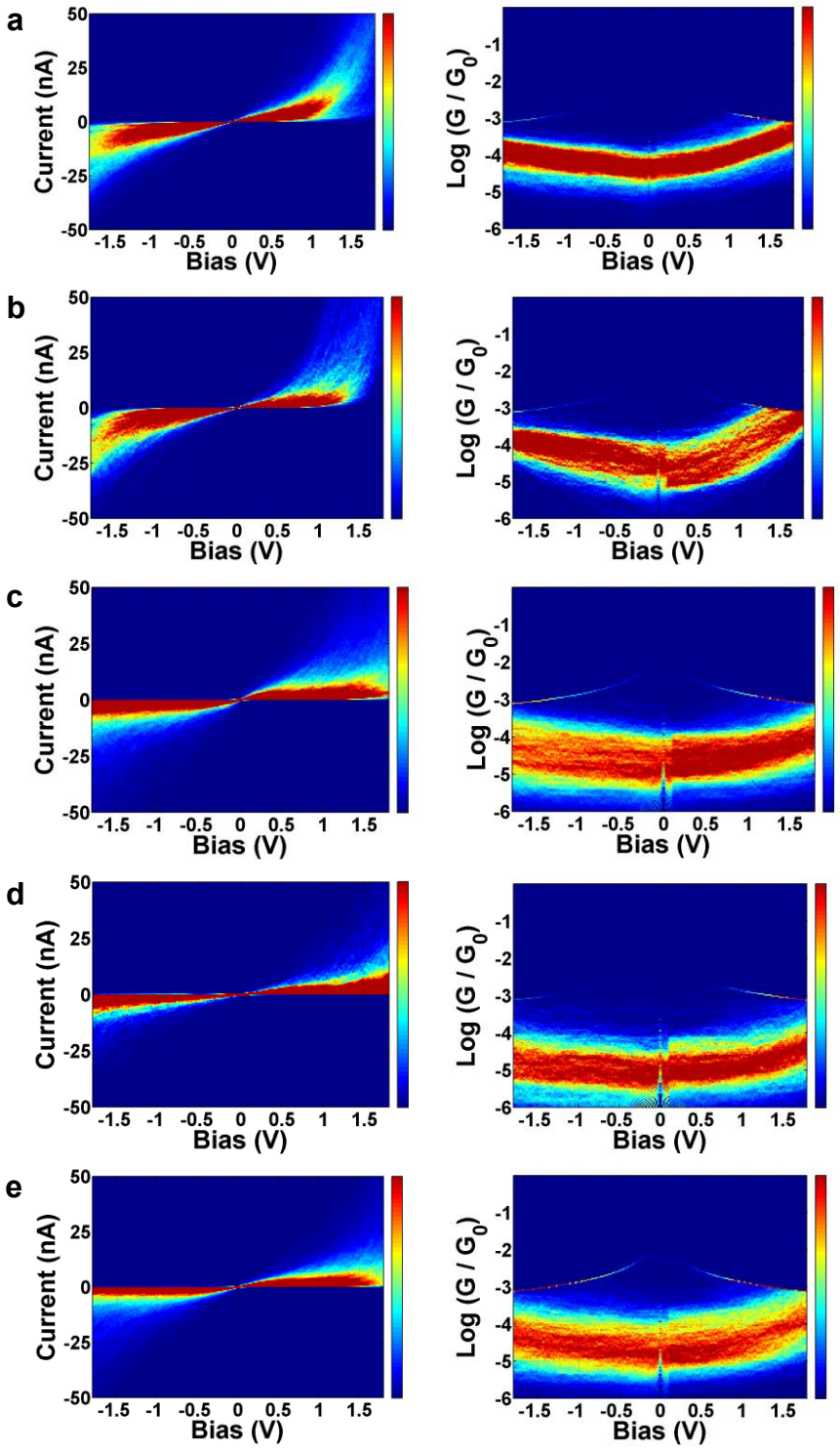

Figure 4.2 2D histograms of I-V (left) and G-V (right) of a) PPCNMe$_2$_d, b) PPCOMe_d, c) PPCH_d, d) PPCCl_d, e) PPCNO$_2$.

The average *I-V* curves for each molecule were compiled from ca. 700 to 1000 individual curves, as shown in Figure 4.3. A clear rectification effect in all five molecular diodes can be seen in all of the *I-V* curves, with the forward bias results in high current and low current under reverse bias. Since the symmetric pentaphenyl paracyclophane molecular wires showed symmetric *I-V* curves,[17] the asymmetric character in the *I-V* curves of these diodes originates from the molecular backbone. It is also clear that the current increases the fastest as the forward bias increases for the diode with the NMe_2 gating group, and was tuned down as the gating group becomes less electron donating. The lowest current under forward bias was reached with electron withdrawing NO_2 as the gating group. This gating effect was similarly observed in the *I-V* characteristics of the symmetrical version of the molecule under positive bias. The junction of the molecule with the most electron-rich gating group has the highest current, while that with the most electron-deficient gating group has the lowest.[17] However, under reverse bias, all molecules exhibit similar current level. The rectification ratio at 1.5 V is calculated and plotted against the corresponding Hammett parameters of the gating groups. The general trend shows that rectification increases as the gating group becomes more electron-rich, with the amine wire having the highest rectification ratio of 2.63.

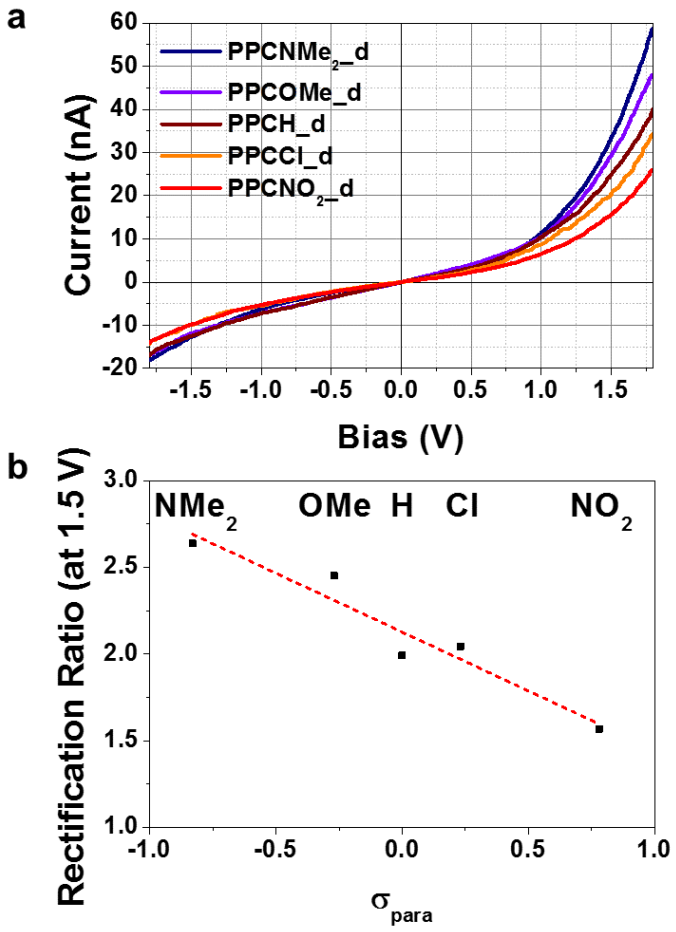

Figure 4.3 a) Average current (nA) over bias (V) plot of five molecular junctions with varying gating groups. The forward bias refers to negative charge applied on Au tip. b) The rectification ratio plotted against the Hammett parameters of the R gating group. The dotted line is for visual aid only.

Since rectification ratio is dependent on bias, transition voltage is another method of revealing inherent junction asymmetry. The Fowler-Nordheim (FN) plot was obtained by converting each *I-V* curve into curve of $\ln(I/V^2)$ as a function of $1/V$. The single-molecule transition voltage can then be deduced by plotting the minimum of the FN plot, which corresponds to transition voltage V_t, against the corresponding conductance. This 2D transition voltage histogram can be further converted into 1D histograms as shown in Figure 4.4 for extracting V_t data.

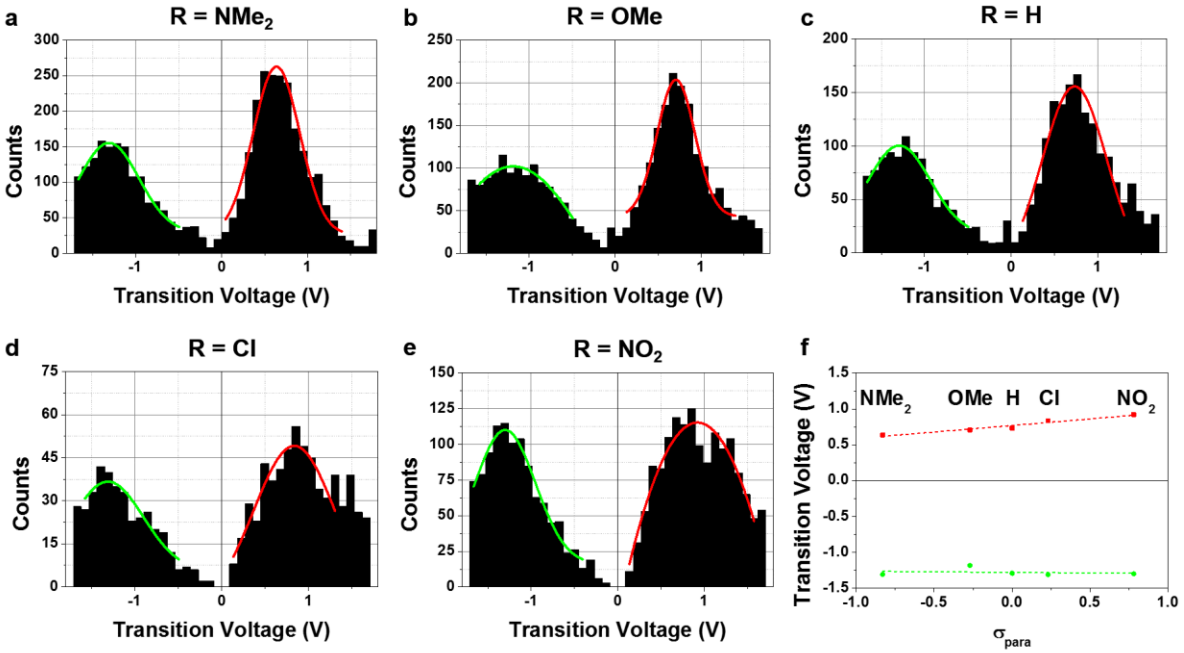

Figure 4.4 a) - e) The transition voltage histograms and Gaussian fit of five molecular junctions with through-space gating groups namely: NMe_2, OMe, H, Cl, NO_2. Red curve corresponds to the positive bias and green curve corresponds to negative bias. f) plot of transition voltages over the Hammett parameter of R group. The dash lines are for visual assistance.

The transition voltage histograms of the series show an increase in forward bias transition voltage V_{t+} as the gating group changes from electron-rich amine group to electron-deficient nitro group, while the reverse bias transition voltage V_{t-} remains relatively constant. Although the transition voltage cannot be quantitatively related to the energy barrier between the HOMO of the molecular backbone and the Au Fermi level in the case of diodes, it can be used to qualitatively evaluate the energy barrier.[19-21] The plot of transition voltage over the Hammett constant of the R gating group showed the through-space electronic gating effect indeed impacted the HOMO energy level and the electron density distribution on the molecular diodes.

4.2.2 Proposed Gated Diodes Transport Mechanism

To explain the underlying mechanisms of the rectification behavior, we propose a model based on a combination of the asymmetric energy level shifting due to electric field and molecule charging in the presence of a bias.[22] The general mechanism is shown in Figure 4.6. Judging from DFT calculated HOMO and LUMO levels, charge transport in this series of molecules mostly occurs via the HOMO. The electric field resulted from the intrinsic dipole of the molecule was calculated based on the dipole moment from the DFT calculations (Table 4.1). It is shown that all five diode molecules exert similar electric dipole field along the backbone direction to the junction. The diode backbone without the cyclophane gate also exhibit similar dipole field. This indicates the gating group has minimal effect on dipolar field generated from the diode, and the contribution comes primarily from the p/n junction. In addition, the Au-S bond dipole also contribute to the asymmetric character of the junction. Comparison of the dipoles between the two ends of the diode shows a more significant dipole on the bipyrimidinyl side, which is attached to the tip electrode (Figure 4.5). As a result, the electric dipole field from the backbone together with the bond dipole of the Au-S bond constructively offset the Fermi level of the tip electrode (ΔE_d in Figure 4.6). Under zero bias, the charge transfer rate is low due to the small energy level overlap between the HOMO and the Fermi level of gold electrodes. Transport occurs via non-resonant tunneling. When the junction is put under a positive bias, the Fermi level of the Au tip decreases further and the HOMO level of the diode shifts in respond to the electrical field between both electrodes. Since the junction is asymmetric and the HOMO is closer to the substrate, the change of the HOMO level is small compared to the shift of the Fermi level of the Au tip. Upon the alignment of the Au tip Fermi level and the HOMO of the backbone, resonant tunneling occurs. Different bias is required to achieve resonant tunneling for the five diodes since their HOMO levels are gated by

the functional groups with different electronic effects. While the forward bias transition voltage V_{t+} does not necessarily represent the resonant bias, the relative trend in Figure 4.4f agrees with this mechanism. DFT calculated HOMO levels also show similar trend. When a negative bias is applied to the junction, the Fermi level of the Au tip increases. At the same time, additional bias is required to counteract the potential from the dipole field exerted onto the junction by the diode core and the bond dipole. The large difference between HOMO level and the Fermi level on the substrate side demands a large bias to reach resonance between the Au electrodes. Transport remains inefficient and occurs mostly due to non-resonant tunneling, leading to a low current in all cases of R groups.

Table 4.1 Electric dipole fields calculated from the dipole moment (DFT) of the core.

	μ (Debye)	μ_x (Debye) [a]	E_x (V/Å) [a, b]	φ (V) [c]
NMe_2	7.9355	4.7166	0.00740	0.04321
OMe	7.1743	5.7782	0.00907	0.05294
H	6.3882	5.2954	0.00831	0.04851
Cl	5.6662	5.3927	0.00846	0.04940
NO_2	5.7503	5.4087	0.00849	0.04955
Backbone	5.3975	5.2820	0.00829	0.04839

[a] Direction along the molecular backbone.

[b] The electric dipole fields were calculated by the equation:

$$\vec{E} = \frac{1}{4\pi\varepsilon_\omega r^3}\left[3\frac{(\vec{p}\cdot\vec{r})\vec{r}}{r^2} - \vec{p}\right]$$

where p is the dipole moment, r is the position relative to the center of mass of the dipole, ε_ω is the permittivity constant of mesitylene.

[c] The potential from the dipole is given by the equation:

$$\varphi = \frac{1}{4\pi\varepsilon_\omega r^3}(\vec{p}\cdot\vec{r})$$

Figure 4.5 Bond dipole comparison between the biphenyl side (2.35 Debye) and the bipyrimidinyl side (5.36 Debye) of the diode.

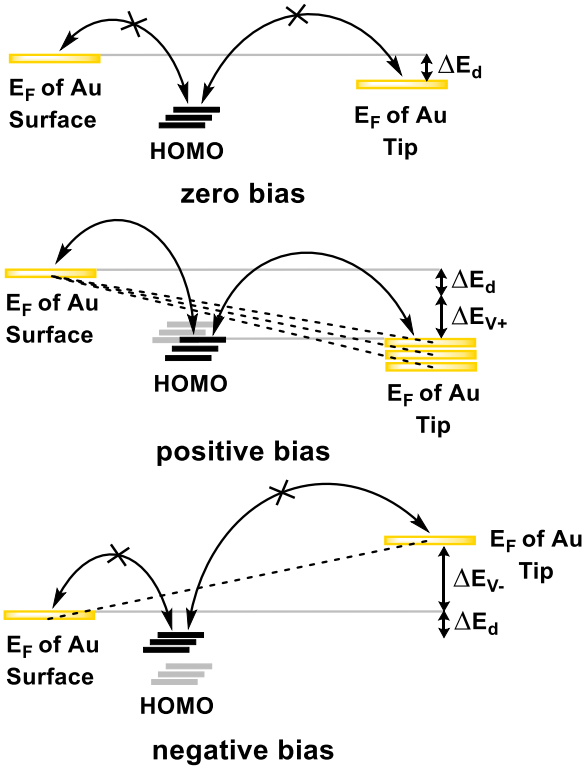

Figure 4.6 The charge transfer mechanism of the pyridinoparacyclophane gated molecular wires. Black bars represent the HOMOs at the respective bias and grey bars represent that at zero bias. ΔE_d is the potential from the electric dipole field of the p/n junction and the Au-S bond.

4.2.3 Theoretical Analysis

The transmission spectra for the diodes with NMe_2, H, and Cl, were calculated based on the non-equilibrium Green's function theory and shown in Figure 4.7a. Highest transmission with the HOMO was observed closest to the electrode Fermi level with the diode bearing the most electron-rich gating group. The transmission peak is shifted further away from the Fermi level as the gating group changes to less electron donating. The trend observed is similar to that in the TVS and DFT calculated HOMO energy levels. In addition, the I-V characteristics of the NMe_2 gated diode was calculated and showed asymmetric feature (Figure 4.8) as expected from the experimental results. The transmission eigenstates of the diode molecule with gating group NMe_2 also exhibit asymmetric geometries at the opposite bias (Figure 4.7b and c), confirming the diode behavior of this molecular wire system.

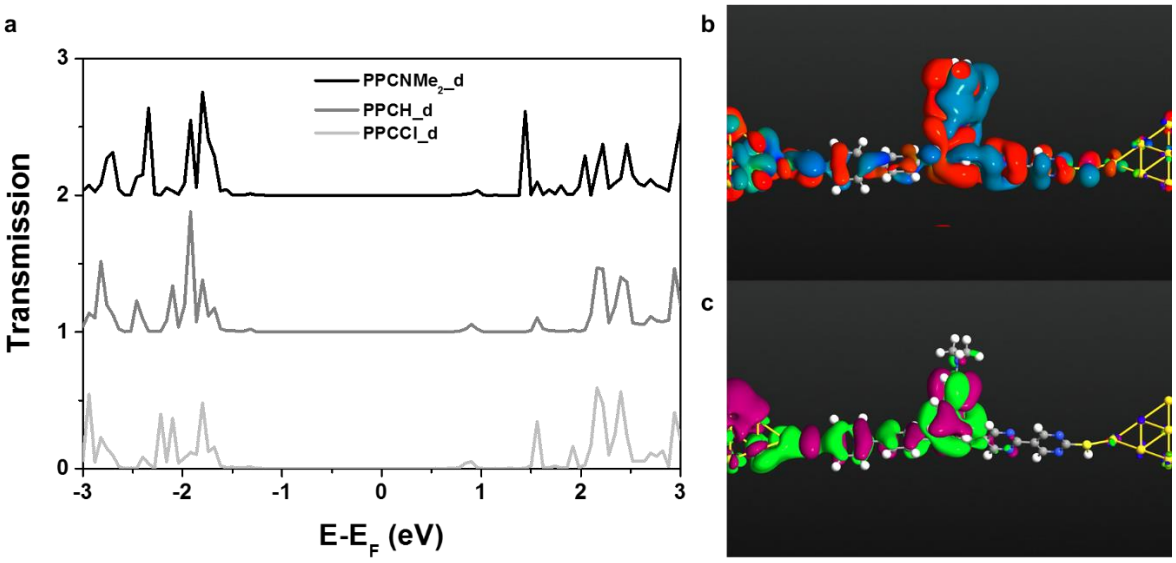

Figure 4.7 a) Transmission spectra of the diode molecules with gating group NMe_2, H, and Cl. Transmission eigenstates of the diode molecule with gating group NMe_2 at b) 1.5 V and c) -1.5 V calculated by non-equilibrium Green's function theory showing asymmetric conducting behavior under forward and reverse bias.

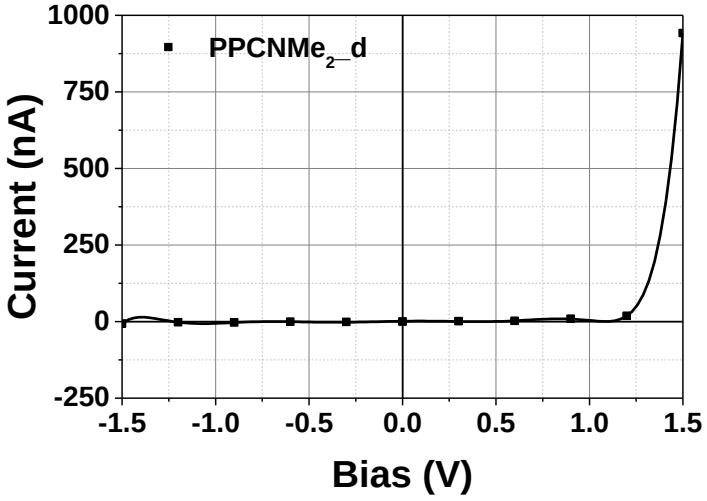

Figure 4.8 Simulated I-V curve for $PPCNMe_2$ under vacuum based on non-equilibrium Green's function theory showing asymmetric characteristics between forward and reverse bias. Black line is the polynomial fit of the data points.

4.3 Conclusion

In conclusion, we have demonstrated the tuning of rectification ratio by through-space gating effect. Rectification ratio increases as the gating group becomes more electron-rich. The forward transition voltage can be correlated with the Hammett parameter of the R gating group on pyridinoparacyclophane, indicating a through-space gating effect of pyridinoparacyclophane on diodes. This fine tuning of charge transport properties of molecular diodes by through-space interaction provides a mean to control properties of molecular electronics without major change to the backbone.

4.4 Experimental Section

Syntheses of Pyridinoparacyclophane Diode Molecular Wires and the Reference Compound:

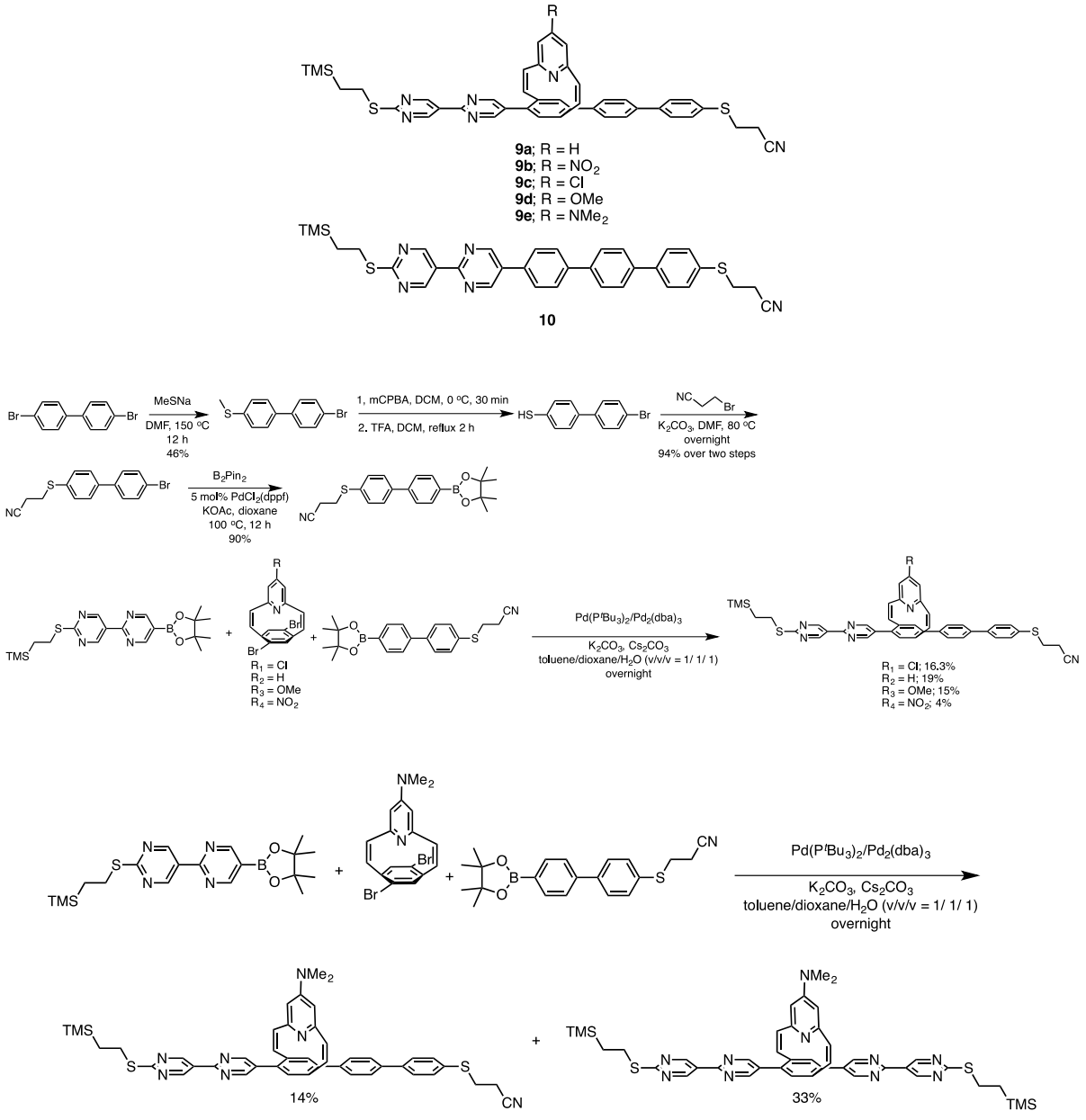

Scheme 4.1 Synthetic route of the molecular diodes.

Materials: 3-(4'-Bromobiphenyl-4-ylthio)propanenitrile and 5-bromo-2'-(2-(trimethylsilyl)ethylthio)-2,5'-bipyrimidine were synthesized according to literature procedures.[11] 5,8-Dibromo-7-chloro-2,11-dithia[3.3](2,6)pyridinoparacyclophane, 5,8-dibromo-7-nitro-2,11-dithia[3.3](2,6)pyridinoparacyclophane, 5,8-dibromo-7-methoxy-2,11-dithia[3.3](2,6)pyridinoparacyclophane and 5,8-dibromo-2,11-dithia[3.3](2,6)pyridinoparacyclophane were synthesized according to literature procedures.[17] Other chemicals and materials are used as received without purification.

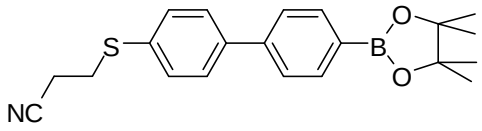

3-(4'-(4,4,5,5-Tetramethyl-1,3,2-dioxaborolan-2-yl)biphenyl-4-ylthio)propanenitrile

In a 250 mL round bottom flask charged with a stirring bar was added 3-(4'-bromobiphenyl-4-ylthio)propanenitrile (430 mg, 1.17 mmol, 1 equiv), bis(pinacolato)diboron (445 mg, 1.75 mmol, 1.5 equiv), $PdCl_2$(dppf) (50 mg, 0.058 mmol, 0.05 equiv) and potassium acetate (344 mg, 3.51 mmol, 3 equiv) and sealed. The flask was evacuated for 5 min and refilled with nitrogen for three times. Dioxane (anhydrous, 24 mL) was added via a syringe. The flask was put in to an oil bath preheated to 100 °C. The reaction was left in oil batch for 15 h and cooled down. The solution was added to saturated sodium bicarbonate solution (20 mL) and extracted with ethyl acetate (20 mL). The organic layer was collected and washed with water (20 mL) and brine (20 mL) and dried with sodium sulfate. The organic layer was filtered and the filtrate was collected and concentrated to yield a brown solid, which was further purified by silica gel column chromatography with gradient ethyl acetate and dichloromethane mixture (1:4 to 4:1). The crude product was further purified by heptane wash to give a white solid. Yield: 482.6 mg, 99%. ^{1}H NMR (500 MHz, $CDCl_3$) δ: 9.49 (s,

2H), 9.05 (s, 2H), 3.25-3.28 (m, 2H), 1.37 (s, 12H), 1.04 – 1.08 (m, 2H), 0.09 (s, 9H). ^{13} C{^{1}H} NMR (125 MHz, $CDCl_3$) δ: 175.1, 163.1, 162.8, 157.0, 125.8, 84.6, 83.4, 27.4, 24.8, 16.8, -1.8. $[M_w+H]^+$ calced for $[C_{21}H_{35}BNO_2S]^+$ at 366.17, MALDI-TOF observed at 364.722.

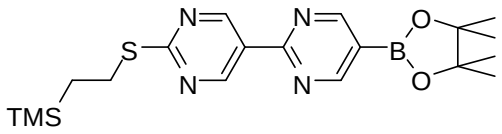

5-(4,4,5,5-Tetramethyl-1,3,2-dioxaborolan-2-yl)-2'-(2-(trimethylsilyl)ethylthio)-2,5'-bipyrimidine

In a 250 mL round bottom flask charged with a stirring bar was added 5-bromo-2'-(2-(trimethylsilyl)ethylthio)-2,5'-bipyrimidine (318 mg, 1mmol, 1 equiv), bis(pinacolato)diboron (381 mg, 1. 5 mmol, 1.5 equiv), $PdCl_2$(dppf) (81.6 mg, 0.1 mmol, 0.1 equiv) and potassium acetate (300 mg, 3 mmol, 3 equiv) and sealed. The flask was evacuated for 5 min and refilled with nitrogen for three times. Dioxane (anhydrous, 20 mL) was added via a syringe. The flask was put in to an oil bath preheated to 100 °C. The reaction was left in oil batch for 15 h and cooled down. The solution was added to saturated sodium bicarbonate solution (20 mL) and extracted with ethyl acetate (20 mL). The organic layer was collected and washed with water (20 mL) and brine (20 mL) and dried with sodium sulfate. The organic layer was filtered and the filtrate was collected and concentrated to yield a brown solid, which was further purified by silica gel column chromatography with gradient ethyl acetate and dichloromethane mixture (0% to 10%) to give a white solid. Yield: 360 mg, 90%. ^{1}H NMR (500 MHz, $CDCl_3$) δ: 7.88-7.90 (d, 2H), 7.57-7.60 (dd, 4H), 7.47-7.50(d, 2H), 3.15-3.18 (t, 3H), 2.60-2.65 (t, 3H), 1.37 (s, 12H). ^{13} C{^{1}H} NMR (125 MHz, $CDCl_3$) δ: 143.2, 141.1, 136.0, 133.0, 132.3, 128.7, 126.8, 118.5, 84.5, 30.8, 25.4, 18.8. $[M_w+H]^+$ calced for $[C_{19}H_{29}BN_4O_2SSi]^+$ at 417.195, MALDI-TOF observed at 416.905.

Synthesis of 5,8-dibromo-7-*N,N*-dimethyl-2,11-dithia[3.3](2,6)pyridinoparacyclophane

In a thick wall tube (4 mL) was added 40 mg 5,8-dibromo-7-chloro-2,11-dithia[3.3](2,6)pyridinoparacyclophane, dimethylamine in THF solution (2 M, 2 mL) and heated to 150 °C for 6 hours. The orange solution was concentrated and purified by silica gel column chromatography with 20% ethyl acetate in hexanes to generate an orange solid. Yield (17 mg, 55%). ^{1}H NMR (400 MHz, $CDCl_3$) δ: 7.13-7.16 (d, 2H), 7.04 (s, 2H), 6.41-6.44 (d, 2H), 6.28 (s, 2H), 2.91 (s, 3H). ^{13} C{^{1}H} NMR (125 MHz, $CDCl_3$) δ: 155.0, 152.4, 144.1, 135.3, 134.2, 133.3, 122.2, 106.4, 39.4. $[M_w+H]^+$ calced for $[C_{17}H_{15}Br_2N_2]^+$ at 406.958, MALDI-TOF observed at 406.731.

Synthesis of diodes:

Compound **9a**: In an oven dried round bottom flask (100 mL) charged with a stirring bar was added 5,8-dibromo-2,11-dithia[3.3](2,6)pyridinoparacyclophane (27 mg, 0.075 mmol, 1 equiv), boronate 1(54 mg, 0.15 mmol, 2 equiv), boronate 2(31 mg, 0.075 mmol, 1 equiv), $Pd(P^tBu_3)_2$ (3.8 mg, 0.0075 mmol, 0.1 equiv), $Pd_2(dba)_3$ (3.4 mg, 0.00375 mmol, 0.05 equiv), Cs_2CO_3 (75 mg, 0.225 mmol, 3 equiv) and Aliquat (1 drop). The flask was degassed by three cycles of evacuation and refill with nitrogen. K_2CO_3 (2M, aqueous solution, 1 mL) was degassed by bubbling N_2 through it for half an hour. Dioxane (anhydrous), toluene (anhydrous, 1 mL) and potassium carbonate solution (1 mL) were added via syringe under nitrogen. The reaction was left stirring at room temperature for 15 h. The reaction was quenched by addition of water (5 mL) and the mixture was extracted with ethyl acetate (4 mL) for three times. The organic layer was combined, dried with sodium sulfate and filtered. The filtrate was concentrated and purified by silica gel column

chromatography with 20% ethyl acetate in hexanes solution to give a pale yellow solid. Yield:14.0 mg, 19%. ^{1}H NMR (500 MHz, $CDCl_3$) δ: 9.47 (s, 2 H), 8.69 (s, 2H), 7.50 – 7.61 (m, 8 H), 7.46-7.47 (d, 2H), 7.46(s, 1H) 7.38 – 7. 41 (t, 1H), 7.32 (s, 1H), 6.83-6.86 (dd, 2H), 6.38 – 6.41 (dd, 2H), 3.27 – 3.29 (m, 2H), 3.18– 3.20 (t, 2H), 2.65 – 2.67 (t, 2H), 1.07- 1.10 (m, 2H), 0.12 (s, 9H). ^{13}C{^{1}H} NMR (125 MHz, $CDCl_3$) δ: 174.6, 159.4, 156.7, 156.6, 152.7, 152.4, 143.3, 141.8, 141.5, 140.2, 139.4, 138.9, 136.1, 135.5, 135.0, 134.9, 134.2, 133.5, 132.2, 132.1, 131.8, 129.6, 128.7, 128.5, 127.9, 127.0, 125.8, 122.3, 122.2, 117.9, 30.3, 27.4, 18.3, 16.7, -1.7. $[M_w+H]^+$ calced for $[C_{43}H_{39}N_6S_2Si]^+$ at 731.244, MALDI-TOF observed at 730.825.

Compound **9b**: In an oven dried round bottom flask (100 mL) charged with a stirring bar was added 4,7-dibromo-15-nitro[2.2](2,6)pyridinoparacyclophane-1,9-diene (28 mg, 0.07 mmol, 1 equiv), boronate 1(38 mg, 0.105 mmol, 1.5 equiv), boronate 2(28 mg, 0.07 mmol, 1 equiv), $Pd(P^tBu_3)_2$ (3 mg, 0.007 mmol, 0.1 equiv), $Pd_2(dba)_3$ (3mg, 0.0035 mmol, 0.05 equiv), Cs_2CO_3 (70 mg, 0.21 mmol, 3 equiv) and aliquat (1 drop). The flask was degassed by three cycles of evacuation and refill with nitrogen. K_2CO_3 (2M, aqueous solution, 0.5 mL) was degassed by bubbling N_2 through it for half an hour. Dioxane (anhydrous), toluene (anhydrous, 1 mL) and potassium carbonate solution (1 mL) were added via syringe under nitrogen. The reaction was left stirring at room temperature for 15 h. The reaction was quenched by addition of water (5 mL) and the mixture was extracted with ethyl acetate (4 mL) for three times. The organic layer was combined, dried with sodium sulfate and filtered. The filtrate was concentrated and purified by silica gel column chromatography with 20% ethyl acetate in hexanes solution to give a pale yellow solid. Yield: 4.1 mg, 8%. ^{1}H NMR (500 MHz, $CDCl_3$) δ: 9.47 (s, 2 H), 8.73 (s, 2H), 7.56 – 7.60

(m, 2 H), 7.49-7.52 (m, 6H), 7.38-7.43(d, 2H) 7.29 (dd, 4H), 6.47-6.54 (dd, 2H), 3.26 – 3.30 (m, 2H), 3.18– 3.21 (t, 2H), 2.64 – 2.68 (t, 2H), 1.06- 1.10 (m, 2H), 0.12 (s, 9H). $^{13}C\{^{1}H\}$ NMR (125 MHz, $CDCl_3$) δ: 174.9, 159.8, 156.7, 156.6, 155.0, 154.7, 154.3, 143.4, 141.1, 140.7, 139.9, 139.3, 139.2, 138.7, 138.0, 134.9, 132.9, 132.4, 132.0, 131.7, 131.6, 129.4, 128.3, 127.9, 127.9, 127.2, 125.6, 117.9, 114.2, 114.1, 30.2, 27.4, 18.3, 16.7, -1.7. $[M_w+H]^+$ calced for $[C_{43}H_{38}N_7O_2S_2Si]^+$ at 776.229, MALDI-TOF observed at 776.009.

Compound **9c**: In an oven dried round bottom flask (100 mL) charged with a stirring bar was added 5,8-dibromo-7-chloro-2,11-dithia[3.3](2,6)pyridinoparacyclophane (40 mg, 0.1 mmol, 1 equiv), boronate 1(36 mg, 0.1 mmol, 1 equiv), boronate 2(41 mg, 0.1 mmol, 1 equiv), $Pd(P^tBu_3)_2$ (6 mg, 0.01 mmol, 0.1 equiv), $Pd_2(dba)_3$ (6 mg, 0.005 mmol, 0.05 equiv), Cs_2CO_3 (100 mg, 0.3 mmol, 3 equiv) and aliquat (1 drop). The flask was degassed by three cycles of evacuation and refill with nitrogen. K_2CO_3 (2M, aqueous solution) was degassed by bubbling N_2 through it for half an hour. Dioxane (anhydrous, 1 mL), toluene (anhydrous, 1 mL) and potassium carbonate solution (0.5 mL) were added via syringe under nitrogen. The reaction was left stirring at room temperature for 17 h. The reaction was quenched by addition of water (5 mL) and the mixture was extracted with ethyl acetate (4 mL) for three times. The organic layer was combined, dried with sodium sulfate and filtered. The filtrate was concentrated and purified by silica gel column chromatography with 20% ethyl acetate in hexanes solution to give a pale yellow solid. Yield: 12.1 mg, 21%. ^{1}H NMR (500 MHz, $CDCl_3$) δ: 9.45 (s, 2 H), 8.70 (s, 2H), 7.59 – 7.54 (m, 6 H), 7.48-7.50 (d, 2H), 7.41 – 7. 43 (d, 2H), 7.39 (s, 1H), 7.31 (s, 1H), 6.85 (s, 2H), 6.27 – 6.32 (dd, 2H), 3.24 – 3.28 (m, 2H), 3.16 – 3.19 (t, 2H), 2.62 – 2.65 (t, 2H), 1.04- 1.08 (m, 2H), 0.10 (s, 9H). $^{13}C\{^{1}H\}$ NMR (125 MHz,

$CDCl_3$) δ: 174.9, 159.7, 156.8, 156.8, 153.9, 153.6, 143.5, 143.2, 141.7, 141.3, 140.2, 139.3, 139.2, 137.8, 136.7, 135.1, 133.3, 132,6, 132.4, 132.1, 131.9, 129.7, 128.8, 128.5, 128.0, 127.3, 125.8, 122.4, 122.3, 118.1, 30.4, 27.6, 18.4, 16.9, -1.6. $[M_w+H]^+$ calced for $[C_{43}H_{38}ClN_6S_2Si]^+$ at 765.205, MALDI-TOF observed at 765.125.

Compound **9d**: In an oven dried round bottom flask (100 mL) charged with a stirring bar was added 5,8-dibromo-7-methoxy-2,11-dithia[3.3](2,6)pyridinoparacyclophane (20 mg, 0.05 mmol, 1 equiv), boronate 1(19 mg, 0.05 mmol, 1 equiv), boronate 2(21 mg, 0.05 mmol, 1 equiv), $Pd(P^tBu_3)_2$ (3 mg, 0.005 mmol, 0.1 equiv), $Pd_2(dba)_3$ (3mg, 0.005 mmol, 0.1 equiv), Cs_2CO_3 (50 mg, 0.15 mmol, 3 equiv) and aliquat (1 drop). The flask was degassed by three cycles of evacuation and refill with nitrogen. K_2CO_3 (2M, aqueous solution, 0.5 mL) was degassed by bubbling N_2 through it for half an hour. Dioxane (anhydrous), toluene (anhydrous, 1 mL) and potassium carbonate solution (1 mL) were added via syringe under nitrogen. The reaction was left stirring at room temperature for 15 h. The reaction was quenched by addition of water (5 mL) and the mixture was extracted with ethyl acetate (4 mL) for three times. The organic layer was combined, dried with sodium sulfate and filtered. The filtrate was concentrated and purified by silica gel column chromatography with 20% ethyl acetate in hexanes solution to give a pale yellow solid. Yield: 5.7 mg, 15%. ^{1}H NMR (500 MHz, $CDCl_3$) δ: 9.47 (s, 2 H), 8.70 (s, 2H), 7.56 – 7.62 (m, 4 H), 7.46-7.51 (m, 6H), 7.41(d, 1H) 7.31 (d, 1H), 6.41-6.42 (dd, 2H), 6.30 – 6.34 (dd, 2H), 3.73 (s, 3H), 3.26 – 3.31 (m, 2H), 3.17– 3.19 (t, 2H), 2.64 – 2.68 (t, 2H), 1.06- 1.10 (m, 2H), 0.12 (s, 9H). ^{13}C NMR (125 MHz, $CDCl_3$) δ: 174.6, 165.7, 159.4, 156.7, 156.6, 153.8, 153.5, 143.4, 141.9, 141.6, 140.2, 139.5, 138.8, 136.2, 135.1, 135.0, 134.4, 133.6, 132.3, 132.1, 131.8, 129.6, 128.9, 128.7, 128.3,

127.9, 127.6, 127.0, 125.8, 117.9, 115.8, 108.6, 108.4, 54.9, 30.3, 27.4, 18.3, 16.7, -1.7. $[M_w+H]^+$ calced for $[C_{44}H_{41}N_6OS_2Si]+$ at 761.255, MALDI-TOF observed at 760.837.

Compound **9e**: In an oven dried round bottom flask (100 mL) charged with a stirring bar was added 4,7-dibromo-15-*N,N*-dimethyl[2.2](2,6)pyridinoparacyclophane-1,9-diene (18 mg, 0.044 mmol, 1 equiv), boronate 1(25 mg, 0.066 mmol, 1.5 equiv), boronate 2(19 mg, 0.044 mmol, 1 equiv), $Pd(P^tBu_3)_2$ (3 mg, 0.0044 mmol, 0.15 equiv), $Pd_2(dba)_3$ (3mg, 0.0044 mmol, 0.15 equiv), Cs_2CO_3 (50 mg, 0.15 mmol, 3 equiv) and aliquat (1 drop). The flask was degassed by three cycles of evacuation and refill with nitrogen. K_2CO_3 (2M, aqueous solution, 0.5 mL) was degassed by bubbling N_2 through it for half an hour. Dioxane (anhydrous), toluene (anhydrous, 1 mL) and potassium carbonate solution (1 mL) were added via syringe under nitrogen. The reaction was left stirring at room temperature for 15 h. The reaction was quenched by addition of water (5 mL) and the mixture was extracted with ethyl acetate (4 mL) for three times. The organic layer was combined, dried with sodium sulfate and filtered. The filtrate was concentrated and purified by silica gel column chromatography with 20% ethyl acetate in hexanes solution to give a pale yellow solid. Yield: 4.6 mg, 14%. ^{1}H NMR (500 MHz, $CDCl_3$) δ: 9.45 (s, 2 H), 8.68 (s, 2H), 7.40 – 7.60 (m, 12 H), 6.25-6.28 (dd, 2H), 6.08-6.12 (dd, 2H), 3.24 – 3.28 (m, 2H), 3.15– 3.18 (t, 2H), 2.88 (s, 6H), 2.61 – 2.65 (t, 2H), 1.06- 1.10 (m, 2H), 0.10 (s, 9H). $[M_w+H]^+$ calced for $[C_{43}H_{38}N_7O_2S_2Si]^+$ at 774.286, MALDI-TOF observed at 774.170.

Synthesis of reference compound 10:

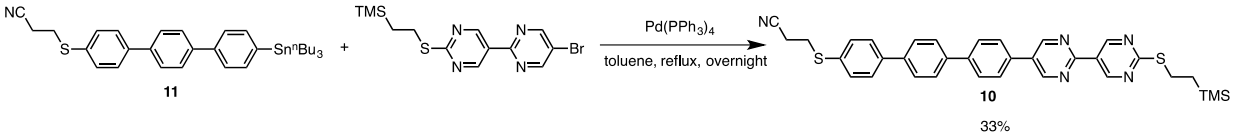

A oven-dried 25 mL round bottom flask was charged with a stirring bar, compound **11** (27 mg, 0.0744 mmol, 1 equiv), 5-bromo-2'-(2-(trimethylsilyl)ethylthio)-2,5'-bipyrimidine (45 mg, 0.0744 mmol, 1 equiv) and $Pd(PPh_3)_4$ (7 mg, 0.007 mmol, 0.1 equiv). The mixture was degassed three times by evacuation and refilled with nitrogen. Dry toluene (2 mL) was added by syringe. The flask was transferred to a preheated 100 °C oil bath and the reaction was left stirring at 100 °C for 14 h. The reaction was cooled down and the toluene was removed by vacuum. The product was purified by silica gel column chromatography with gradient dichloromethane to 20% ethyl acetate in dichloromethane (V/V). The crude product was further purified by precipitation in ethanol to give a pale yellow solid. Yield: 45 mg, 33%. ^{1}H NMR ($CDCl_3$) 9.52 (s, 2H), 9.07 (s, 2H), 7.81-7.83 (d, 2H), 7.76-7.69 (m, 6H), 7.65-7.62 (d, 2H), 7.51-7.53 (d, 2H), 3,26-3,30 (t, 2H), 3.17-3.21 (t, 2H), 2.64-2.68 (t, 2H), 1.06-1.10 (t, 2H), 0.11 (s, 9H). ^{13}C NMR ($CDCl_3$) 174.9, 160.9, 156.7, 155.2, 141.2, 140.0, 139.5, 139.3, 133.1, 132.5, 132.0, 131.8, 128.0, 127.9, 127.6, 127.5, 127.2, 125.6, 117.9, 30.3, 27.4, 18.3, 16.8, -1.7. $[M_w+H]^+$ calced for $[C_{34}H_{34}N_5S_2Si]^+$ at 604.20, MALDI-TOF observed at 603.92.

UV characterization of compounds:

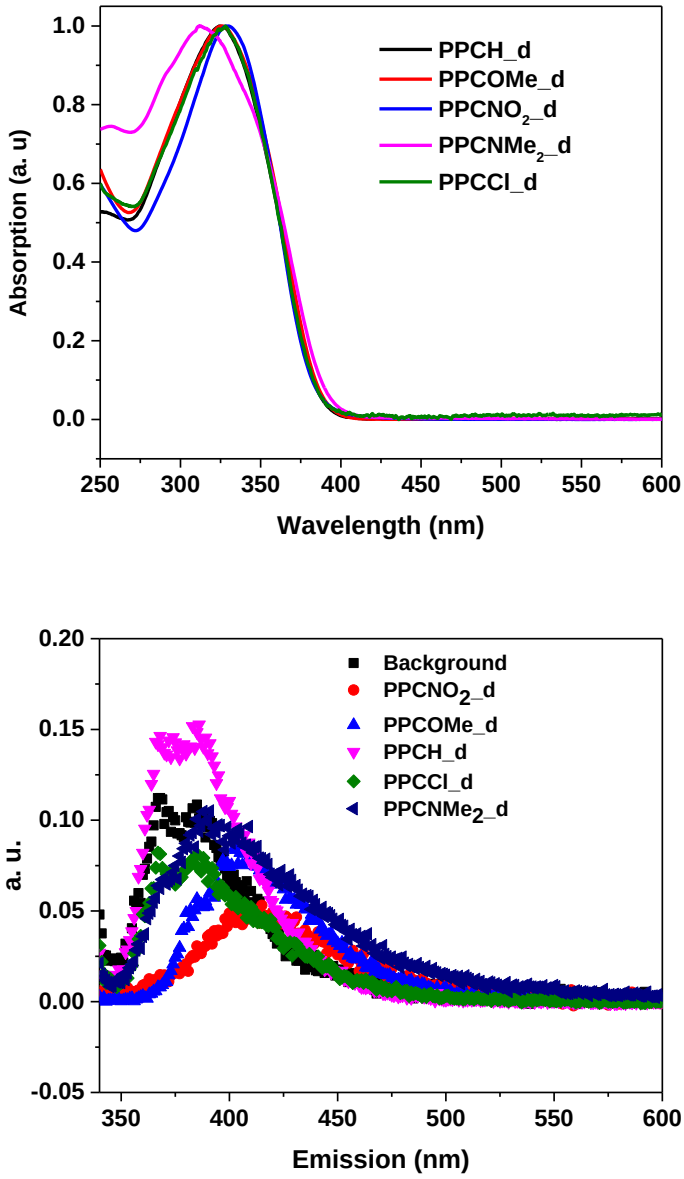

Figure 4.9 UV-vis and PL spectra of 9a-e. Excitation wavelength at 330 nm.

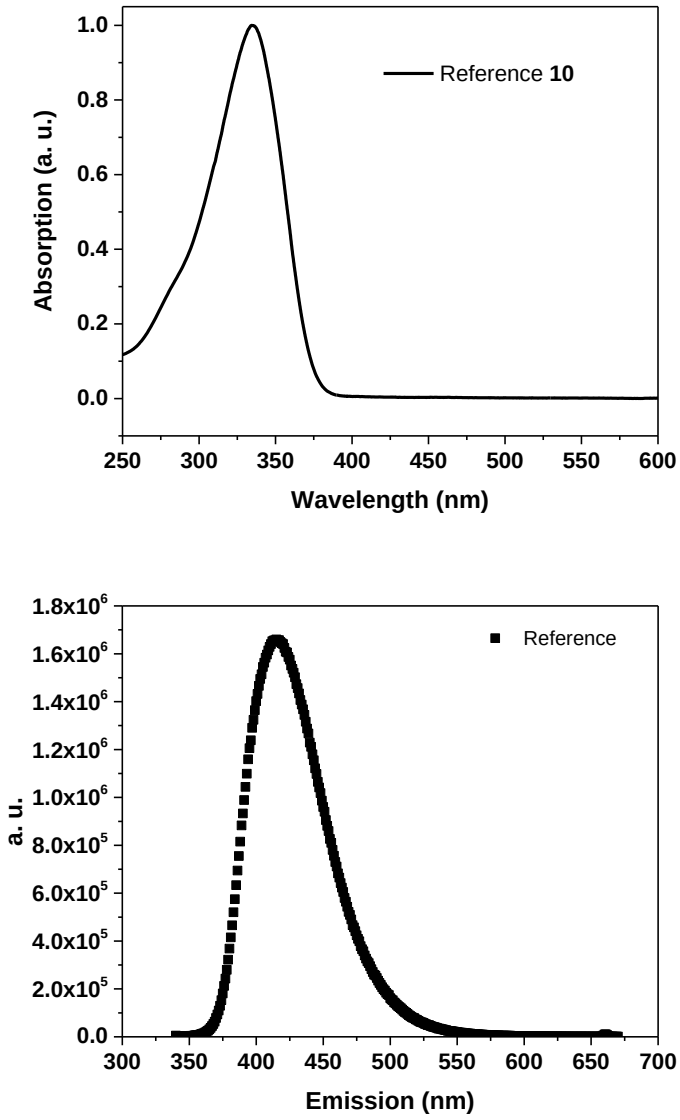

Figure 4.10 UV-vis and PL spectra of reference compound 10. Excitation wavelength at 330 nm.

Preparation of self-assembled monolayers (SAMs) and break-junction experiment for single molecule junctions:

Preparation of Self-Assembled Monolayers (SAMs). Prior to each experiment, the substrate was briefly annealed in a butane flame. The self-assembled monolayers (SAMs) of the five molecules

were prepared in a two-step procedure to allow sequential deprotection. Cesium hydroxide ($CsOH \cdot H_2O$ in EtOH), a deprotecting agent for the CNE group, was first added to an anhydrous tetrahydrofuran (THF) solution containing ca. 5×10^{-5} M of the target molecule protected under N_2. A gold substrate was immersed in the solution for 12 hours. The substrate was then washed successively with THF, water, and ethanol, dried under a stream of N_2, and immersed in anhydrous THF under N_2. Tetrabutylammonium fluoride (in THF) was added to remove the TMSE group. After 6 hours, the substrate was again washed successively with THF, and ethanol, dried under a stream of N_2, and immediately used for measurements.

Break-Junction Experiment for Single Molecule Junctions. The STM-BJ experiments were performed with a previously described STM break-junction setup. Briefly, fresh gold tips were prepared by mechanically cutting a 0.25 mm gold wire (99.998% Alfa Aesar). The experiments were carried out in degassed mesitylene (≥99.9% Sigma-Aldrich), which reduced possible surface contamination. Before use, the STM Teflon solvent holder was sonicated in acetone and dried with N_2. During measurement, the solvent holder was placed over the gold–SAM surface and filled with a couple drops of mesitylene. A typical break-junction experiment comprised thousands of current–distance traces. Of these traces, ~ 50% displayed plateaus that corresponded to the formation of a molecular bridge and were employed to build the histograms. The break-junction experiments were performed at a bias of 100 mV.

***I-V* recording for single molecule junctions.** The *I-V* recording experiments were carried out at 100 mV of bias voltage in mesitylene. The entire process consists of iterations of three steps, tapping, conductance step detection and *I-V* recording, which is in contrast to the single-step tapping procedure used in the STM break junction measurements. In the tapping step, the tip is

moved towards the substrate until the current reaches a preset threshold, and then is retracted until it reaches a lower preset current. In the present method, the conductance step detection is applied during each retraction cycle to identify conductance steps. The measured conductance range was selected according to the previously measured conductance histogram of each molecule. Once a conductance step is detected, the *I-V* recording step is activated, which involves the following sub-steps: 1) The tip is immediately held in position, 2) the current -voltage curve was recorded from + 1.8 V to – 1.8 V quickly (10 Hz), 3) upon completion of the *I-V* curve, the tip was pulled away from the substrate until the current drop to a preset value, and the measurement started over again.

Theoretical Calculations:

DFT calculations were performed using Gaussian 09 with functional and basis set b3lyp/6-31g**. Electron transport calculations for the molecular diodes were performed with the non-equilibrium Green's function-density functional theory method via the Atomistix Toolkit (ATK) package. Self-consistent calculations were performed using a double-ξ polarized basis set except for the gold atoms in the electrodes for which a single-ξ polarized basis set was used. Exchange correlation was treated using the local spin density approximation and all atoms were relaxed such that the force per atom was less than 0.05 eV/Å. K-point samplings of 3 x 3 x 50 was employed for all junction calculations with 50 being on the direction along transport.

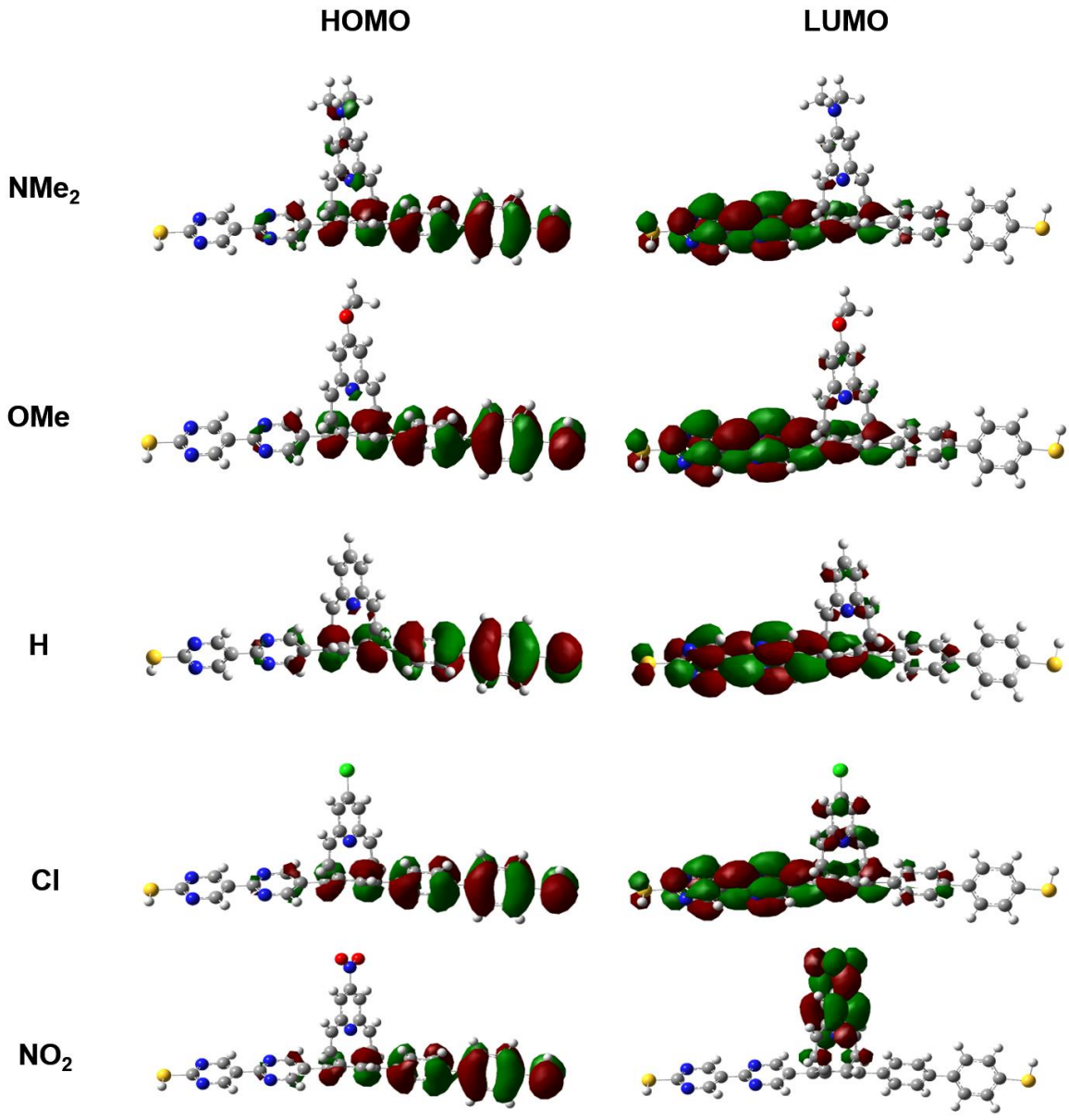

Figure 4.11 DFT calculated (b3lyp/6-31g**) ground state molecular orbitals of the five diode molecules.

4.5 References

(1) Song, H.; Reed, M. A.; Lee, T. *Adv. Mater.* **2011**, *23*, 1583-1608.
(2) Sun, L.; Diaz-Fernandez, Y. A.; Gschneidtner, T. A.; Westerlund, F.; Lara-Avila, S.; Moth-Poulsen, K. *Chem. Soc. Rev.* **2014**, *43*, 7378-7411.

(3) Xiang, D.; Wang, X.; Jia, C.; Lee, T.; Guo, X. *Chem. Rev.* **2016**, *116*, 4318-4440.
(4) Jia, C.; Migliore, A.; Xin, N.; Huang, S.; Wang, J.; Yang, Q.; Wang, S.; Chen, H.; Wang, D.; Feng, B.; Liu, Z.; Zhang, G.; Qu, D.-H.; Tian, H.; Ratner, M. A.; Xu, H. Q.; Nitzan, A.; Guo, X. *Science* **2016**, *352*, 1443-1445.
(5) Meng, F.; Hervault, Y.-M.; Shao, Q.; Hu, B.; Norel, L.; Rigaut, S.; Chen, X. *Nat. Commun.* **2014**, *5*, 3023.
(6) Katsonis, N.; Kudernac, T.; Walko, M.; van der Molen, S. J.; van Wees, B. J.; Feringa, B. L. *Adv. Mater.* **2006**, *18*, 1397-1400.
(7) Lo, W.-Y.; Zhang, N.; Cai, Z.; Li, L.; Yu, L. *Acc. Chem. Res.* **2016**, *49*, 1852-1863.
(8) Aviram, A.; Ratner, M. A. *Chem. Phys. Lett.* **1974**, *29*, 277-283.
(9) Ng, M.; Yu, L. *Angew. Chem. Int. Ed.* **2002**, *41*, 3598-3601.
(10) Jiang, P.; Morales, G. M.; You, W.; Yu, L. *Angew. Chem. Int. Ed.* **2004**, *43*, 4471-4475.
(11) Morales, G. M.; Jiang, P.; Yuan, S. W.; Lee, Y. G.; Sanchez, A.; You, W.; Yu, L. P. *J. Am. Chem. Soc.* **2005**, *127*, 10456-10457.
(12) Díez-Pérez, I.; Hihath, J.; Lee, Y.; Yu, L.; Adamska, L.; Kozhushner, M. A.; Oleynik, I. I.; Tao, N. *Nat. Chem.* **2009**, *1*, 635-641.
(13) Lee, Y.; Carsten, B.; Yu, L. *Langmuir* **2009**, *25*, 1495-1499.
(14) Capozzi, B.; Xia, J.; Adak, O.; Dell, E. J.; Liu, Z.-F.; Taylor, J. C.; Neaton, J. B.; Campos, L. M.; Venkataraman, L. *Nat Nano* **2015**, *10*, 522-527.
(15) Guo, C.; Wang, K.; Zerah-Harush, E.; Hamill, J.; Wang, B.; Dubi, Y.; Xu, B. *Nat. Chem.* **2016**, *8*, 484-490.
(16) Boxer, S. G. *Annu. Rev. Biophys. Biophys. Chem.* **1990**, *19*, 267-299.
(17) Lo, W.-Y.; Bi, W.; Li, L.; Jung, I. H.; Yu, L. *Nano Lett* **2015**, *15*, 958-962.
(18) Li, L.; Lo, W.-Y.; Cai, Z.; Zhang, N.; Yu, L. *Chem. Sci.* **2016**, *7*, 3137-3141.
(19) Beebe, J. M.; Kim, B.; Frisbie, C. D.; Kushmerick, J. G. *ACS Nano* **2008**, *2*, 827-832.
(20) Huisman, E. H.; Guédon, C. M.; van Wees, B. J.; van der Molen, S. J. *Nano Lett* **2009**, *9*, 3909-3913.
(21) Xie, Z.; Bâldea, I.; Smith, C. E.; Wu, Y.; Frisbie, C. D. *ACS Nano* **2015**, *9*, 8022-8036.
(22) Lörtscher, E.; Gotsmann, B.; Lee, Y.; Yu, L.; Rettner, C.; Riel, H. *ACS Nano* **2012**, *6*, 4931-4939.

CHAPTER 5

EXCEPTIONAL SINGLE-MOLECULE TRANSPORT PROPERTIES OF LADDER-TYPE HETEROACENE MOLECULAR WIRES

5.1 Introduction and Background

Fundamental understanding on controlling charge transport through single molecules is the central theme of molecular electronics.[1-4] In particular, how to design molecules that allow efficient charge transport over extended distance is one of the important goals in the realization of molecular electronics. As mentioned in Chapter 1, the distance dependence of the single molecule conductance is characterized by the tunneling decay constant, β. It was observed that electron conductance decreases exponentially as a function of the molecular length, $\sigma_M \propto e^{-\beta L}$, where σ_M is the single molecule conductance and L is molecular length.[5, 6] The lower the β value, the better the molecule is able to mediate long range charge transport. It was shown that π-conjugated molecules typically have lower β value than aliphatic σ-bond molecules. The delocalization of orbitals and the small energy gap between the highest occupied molecular orbitals (HOMO) and the lowest unoccupied molecular orbitals (LUMO) allow π-conjugated molecules to function as highly conductive wires. The Fermi energy level of the metal electrodes typically locates within the bandgap of these molecules with small offset relative to either the HOMO or the LUMO, resulting in efficient charge injection and transport.

Numerous molecules were investigated and the length dependence of their conductance can usually fit with the equation above. For example, oligothiophenes are among the most studied materials in molecular electronics due to their highly conjugated π-orbitals and efficient charge transport.[7] Other structural factors, such as effects of side chains and terminal groups on charge transport in oligothiophenes have been studied.[8-12] The conductance indeed showed exponential decay as a function of length. Interestingly, it was shown that simple tetrathiophene exhibits higher conductance than the terthiophene.[13, 14] The observation was attributed to the difference in the HOMO alignment relative to the Fermi level of gold electrodes by Tao et al.[13] Campos et al argue for the contribution due to the change in molecular conformation during the STM break-junction experiment.[14] Most recently Xiang et al. observed that iodide-terminated oligothiophene molecules do not follow the exponential length dependence due to transition in binding geometry to the electrodes with change in molecular length.[15]

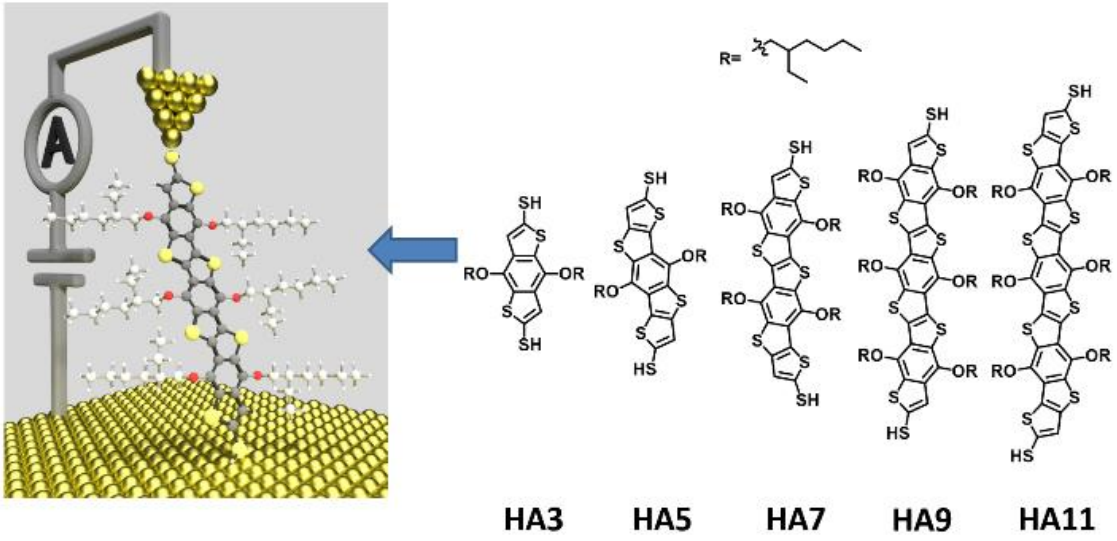

Figure 5.1 Experimental setup. Chemical structure of the heteroacene molecular wires and a representation of metal-molecule-metal junction in the STM break-junction technique.

Most recently, the Yu group have synthesized a series of new fused heteroacene molecule.[16, 17] These molecules can be easily functionalized with thiol groups, offer us opportunity to investigate the length dependence of conductance through these ladder types of molecules. The fused structure of these molecular wires locks the π system in a single planar conformation and eliminate the uncertainty caused by the conformational change typical in oligothiophene and other linear π-conjugated systems during transport through the junction.[14] In this chapter, five molecules were synthesized and the number of rings in these fused heteroacenes are 3, 5, 7, 9, and 11 with names and structures as shown in Figure 5.1. Thiol groups are installed on the two ends of these molecules and protected with acetyl groups, which can be easily deprotected with ammonium hydroxide to form the free thiols for further immobilization onto gold surface. All molecules except HA7 are symmetrical in the conducting backbone with ethylhexyl branched side chains to solubilize the molecules.

5.2 Sample Characterizations and STM Break-Junction Experiments

Synthesis and characterization of these heteroacene (HA) molecular wires can be found in the supporting information. Thiol-gold binding chemistry was utilized to prepare self-assembled monolayer (SAM) of the thiol molecules in order to measure their single-molecule conductance.[18]Successful immobilization of these molecules onto gold surfaces was confirmed by the XPS characterizations and the CV measurements (Figure 5.2 and Figure 5.3).

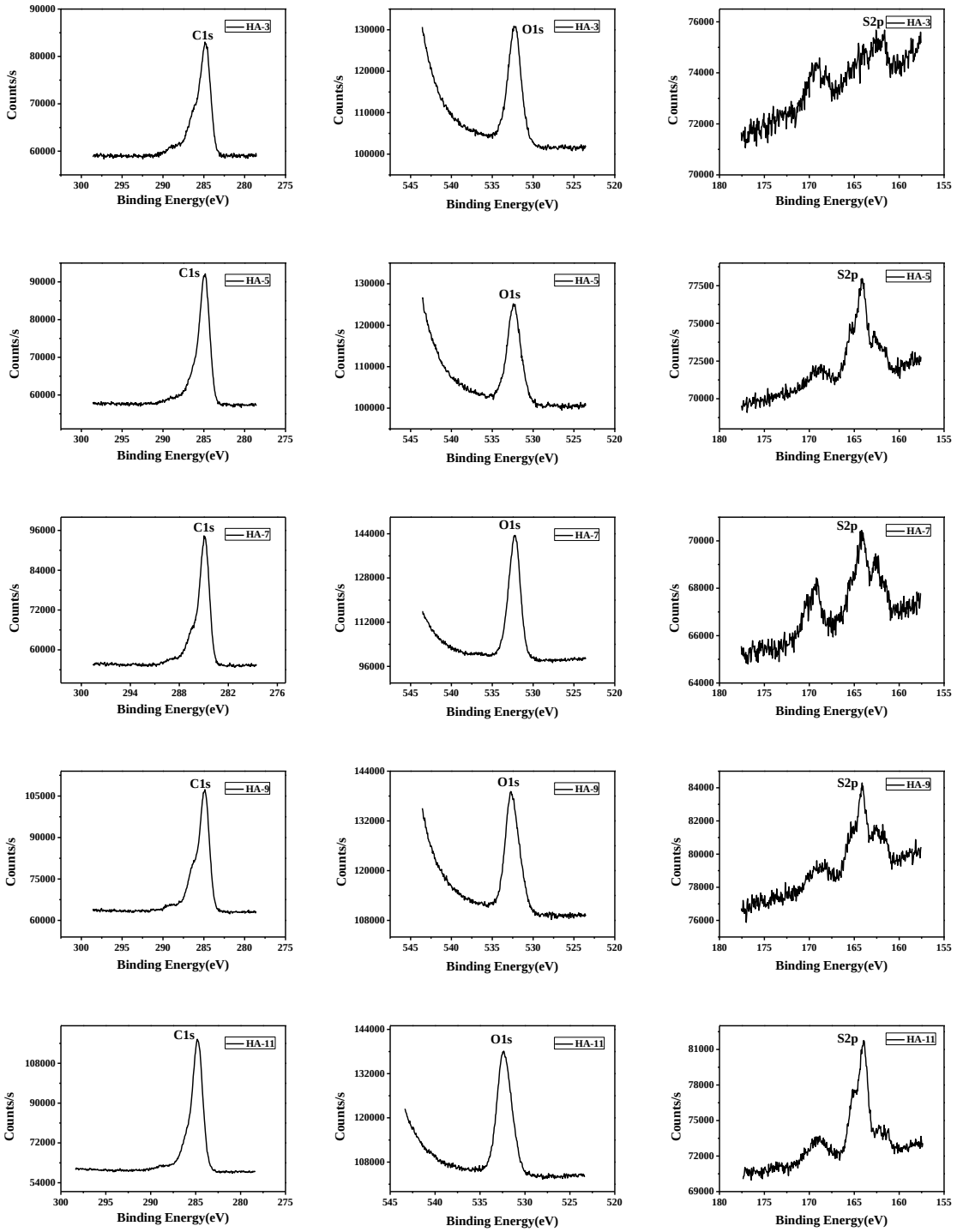

Figure 5.2 XPS carbon 1s, oxygen 1s, sulfur 2p spectra of HA3, HA5, HA7, HA9, and HA11. The extra higher energy peaks on the sulfur spectra (~169 eV) correspond to oxidized sulfur (e.g. sulfoxide).

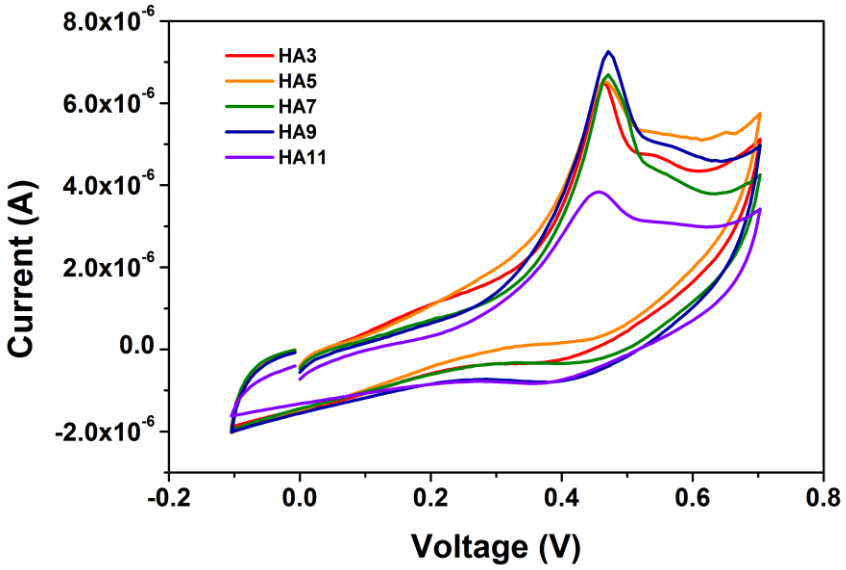

Figure 5.3 Cyclic voltammograms of ferrocene functionalized heteroacene molecular wire monolayer on gold.

5.2.1 Length Dependent Conductance of Ladder-Type Molecules

Break-junction technique with a modified STM system was utilized to measure the single-molecule transport properties.[19-21] The experiments were conducted at a bias voltage of 0.1 V in degassed mesitylene. The conductance-distance traces of the molecules with different lengths were recorded by a program written in LabVIEW. The typical conductance-distance decay curves for the heteroacene molecular junctions with different lengths are shown in Figure 5.4a. The conductance plateaus locate ca. 10^{-4} G_0 are the characteristic signatures of single-molecule junctions, where G_0 is the conductance quantum $2e^2/h$ (e is the charge of electron and h is the Planck constant). Measurements were performed repeatedly to provide a statistical analysis of the single-molecule junction. A conductance histogram can be generated by compiling the effective conductance-distance curves as shown in Figure 5.4b. A clear single peak can be observed for each of the molecules measured which was fitted by a Gaussian function to determine the corresponding

conductance values. The values of the single-molecule conductance of HA3, HA5, HA7, HA9, and HA11 under a bias voltage of 0.1 V were determined to be $8.08 \times 10^{-4}\ G_0$, $5.14 \times 10^{-4}\ G_0$, $4.05 \times 10^{-4}\ G_0$, $2.81 \times 10^{-4}\ G_0$, and $1.84 \times 10^{-4}\ G_0$ respectively. A plot of $\ln(G_0)$ vs length can be constructed with these conductance values and the corresponding lengths of the molecular wires, as shown in Figure 5.4c. The slope of the linear fitting represents the length dependent decay constant β at that particular voltage. At low bias, a β value of 0.088±0.007 $Å^{-1}$ was obtained for this series of heteroacene molecular wires. These are one of the lowest β values, significantly lower than other π-conjugated molecules such as oligophenylenes (0.43 $Å^{-1}$), oligothiophenes (0.16 $Å^{-1}$, 0.4 $Å^{-1}$), and cyclopenta-difluorenes (0.21 $Å^{-1}$) .[8, 22] The results indicate that the ladder structure with locked π system together with thiophene unit can support efficient charge transport over long distance.

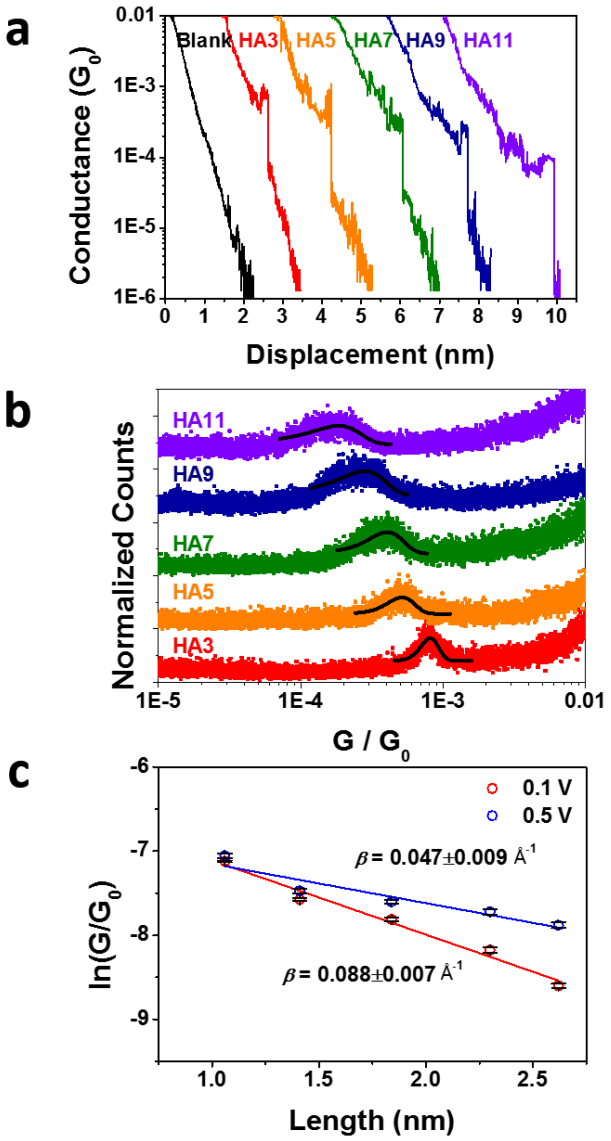

Figure 5.4 Molecular conductance of heteroacene wires. (a) Typical molecular conductance-distance traces of the five heteroacene molecular junctions. (b) Conductance histograms with Gaussian fitting. (c) A plot of ln(G_0) vs length of the junctions at 0.1 and 0.5 bias. Solid line is the linear fit with slopes corresponding to the β value.

5.2.2 Single-Molecule Current-Voltage Characteristics

To further understand the charge transport behavior of these heteroacene molecular wires, the current-voltage (I-V) characteristics of these molecular junctions were investigated. The Au tip of

the STM probe head was briefly held in the position, corresponding to the plateau in the conductance-distance curve and indicating single molecular junction, while a voltage sweeps between 1.5 V and -1.5 V. The current-voltage characteristics of molecular junctions were repeatedly measured for a statistical evaluation and are shown in Figure 5.5. Nonlinearity between the current and the bias voltage in the *I-V* curves are clearly observed, consistent with the corresponding bowl-shaped conductance-voltage (G-V) histograms (Figure 5.5b). As the molecule length of the heteroacene increases, the current is increasing more rapidly with voltage. This is more clearly observed in the G-V histogram through the increased curvature of the G-V bands from HA3 to HA11. In addition, the most probable conductance of the heteroacene wires at higher voltage can be obtained from the G-V histograms and the results are plotted alongside with the low bias conductance in Figure 5.4c, from which the decay constant of the heteroacene molecular wire system at 0.5 bias voltage was determined to be 0.047±0.009 $Å^{-1}$. This value is smaller than that obtained at 100 mV bias voltage, showing a decrease in length dependence of these heteroacene molecules at higher bias.

The single-molecule transition voltage spectroscopy (TVS) can be obtained by plotting $\ln(I/V^2)$ as a function of 1/V, also known as the Fowler Nordheim (FN) plot.[21, 23-25] The minimum of the plot corresponds to transition voltage V_t. Plot of these voltages with their corresponding conductance results in the 2D transition voltage spectra shown in Figure 5.5c, which can be converted to 1D histograms as shown in Figure 5.5d for extracting V_t data. The transition voltage histograms of the series show a decrease in V_t as the length of the molecular wire increases, from 0.73 V for HA3 to 0.21 for HA11. The peak locations of the transition voltages are fairly symmetrical in values between the forward and the reverse bias sweep. These values are quite low comparing with other π-conjugated molecules.[21, 26, 27]

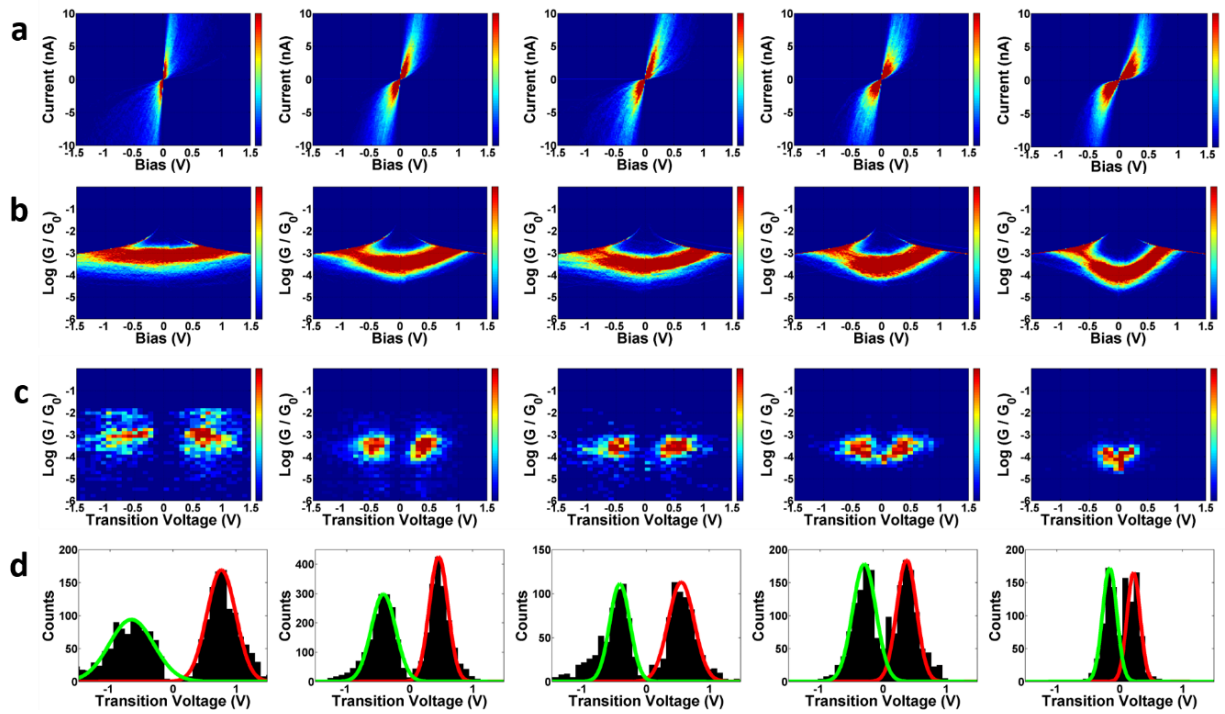

Figure 5.5 Current-Voltage Characteristics Measurements. (a) Current-voltage characteristics histogram, (b) conductance-voltage histogram, (c) transition voltage histogram, and (d) 1-D transition voltage histogram of HA3, HA5, HA7, HA9, HA11 (from left to right).

5.2.3 Transition Voltage Spectroscopy Analysis

To understand the implication of these results, the Newns-Anderson model was employed to analyze the transport data, assuming that the transport is dominated by a single orbital.[28-30] For hole-transporting material, the assumption implies that the LUMO and the HOMO-1 are sufficiently far away from the Fermi level of the electrodes. The charge transport can be described as an off-resonant coherent tunneling process with a simple energy offset $\varepsilon_h = E_F - E_{HOMO}$ where E_F is the Fermi level of the electrode. When a bias V is applied to the junction, the energy offset between the Fermi level of electrodes and the energy level of the transport orbital can be approximated as $\varepsilon_h(V) = \varepsilon_h - \gamma eV$, where voltage division factor γ was derived to account for the asymmetric I-V characteristics and consequently the transition voltages due to the polarity of the

bias. Thus, the experimentally measured transition voltages $V_{t\pm}$ for both bias polarities can be used to calculate the corrected energy offset ε_h and γ using the equations developed by Baldea[31, 30]. For junctions with symmetrical *I-V* characteristics (i.e. $\gamma = 0$), the expression for the transition voltage can be simplified as $eV_t = 2\varepsilon_h/\sqrt{3}$. The calculated values of the energy offset ε_h for the HA molecular wires are plotted against the number of fused ring in the molecule in Figure 5.6a as the red data points. The absolute values of all voltage division factor γ are < 0.01 with the exception of HA7 (0.018) due to the asymmetric feature of the molecular wire. Also shown in Figure 5.4a is a comparison of the energy offsets calculated using the transition voltages obtained from the STM break-junction experiments (red) with the energy difference between the Fermi level of gold (-5.0 eV) and the HOMO energy levels of the protected molecular wires measured by cyclic voltammetry (black). The energy offsets derived from the transition voltages follow the same trend with those obtained from CV measurements: energy offset decreases as the length of the molecule increases. As the conjugation of the molecule extends, the energy gap becomes narrower. This brings the HOMO of the molecule closer to the Fermi level of the metal electrode, resulting in smaller energy offset. In addition, the increased number of electron donating alkoxy side-chains in the longer molecules makes the molecule more electron rich contributed to the increase in HOMO energy level. The energy diagram of the molecules obtained by optical and electrical characterizations shown in Figure 5.7 clearly illustrated this point.

To further study the correlation between molecule length and transition voltage, the dependence of the parameter $\chi = |E_F - E_{HOMO}| / V_t$ on molecular length was investigated (Figure 5.6b).[32, 33] This parameter can reveal the relationship between the transition voltage and the energy offset of the transport orbital. For shorter molecules (i.e. HA3, HA5, HA7), the value of χ exhibits narrow variation. This is a reflection of the strong screening effect in conjugated molecules.[34, 35] The π

electrons delocalized throughout the conjugated molecule and can screen out the voltage, resulting in voltage drop near the contacts of the junction. The χ value is relatively well-defined in this region. However, TVS becomes increasingly inaccurate for determining the HOMO energy offset as the transport orbital locates closer to the Fermi energy of the electrode, as shown by the small χ value for HA11 in Figure 5.6b.

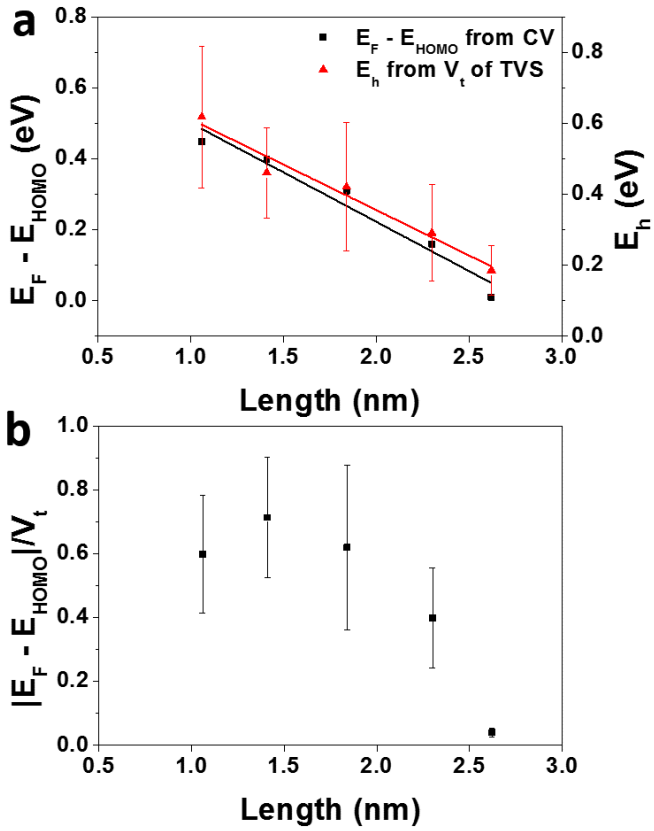

Figure 5.6 Energy Offset Comparisons. (a) The energy offsets obtained from the difference of the Fermi level of gold and the HOMO from CV measurements (black squares, left axis) are compared with those obtained from the transition voltage in the break-junction experiment using the Newns-Anderson model (red triangles, right axis). (b) A plot of $\chi = |E_F - E_{HOMO}| / V_t$ versus molecule length.

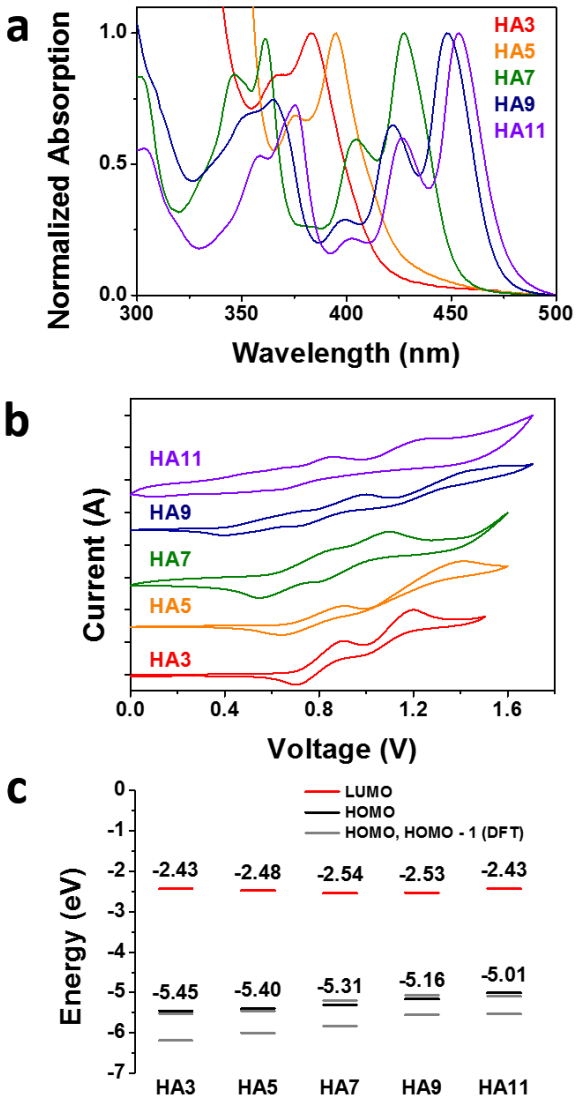

Figure 5.7 Wire Molecules Characterizations. (a) UV-vis spectra and (b) cyclic voltammograms of the five fused ring heteroacene molecular wires. (c) Energy diagram of the molecular wires showing the HOMO (black) and the LUMO (red) derived from UV-vis and CV measurements, along with the HOMO and the HOMO-1 levels obtained by DFT calculations (grey).

5.2.4 Theoretical Analysis

Transport calculations based on the non-equilibrium Green's function-density functional theory (NEGF-DFT) method offer further insight into the states involved in the transport in the HA

molecular wires. Geometries of each junction are optimized with DFT calculations before performing the transport calculation. Figure 5.6b shows the calculated low bias transmission spectra of HA3 to HA11. The main peak at ~ -1.5 eV corresponds to transport through the HOMO, while the peak at > 0.5 eV corresponds to transport through the LUMO. The shorter molecular wires (e.g. HA3) having a larger HOMO-LUMO gap exhibits higher transmission but over a narrower range, while longer molecular wires have lower transmission over a wider range. As the length of the molecular wire increases, additional high transmission states emerge close to the HOMO of the junction. Their contribution to hole transport is not included in the single-level analysis in the Newns-Anderson model. Figure 5.8c-f shows that these additional states correspond to the lower energy orbital of the molecules. The geometries of the transmission eigenstates of the junctions match up with those of the HOMO-1 and the HOMO of the molecule itself. The HOMO-1 eigenstate also shows larger electron density on the tip Au atoms in both HA9 and HA11 junctions. Bias applied on the junction brings the frontier orbitals closer to the electrode Fermi level, including the HOMO-1 orbital. This becomes significant for the longer molecules as their HOMO/HOMO-1 gaps are smaller due to extended conjugation (Figure 5.7c), which may possibly allow more efficient transport through the HOMO-1 level at higher bias. The I-V curves shown in Figure 5.9d, e indeed showed fine features in the dI/dV spectra. However, cautions must be exercised in assigning these features. More experiments, especially those at low temperature, are needed to firmly designate these features to contributions from HOMO-1 transport. Further simulation of the I-V curve of the HA11 junction indicates that the calculation is consistent with the experimental data, as shown in Figure 5.8g. The experimental I-V curve of HA11 was compiled from the average of 25 individual curves from the STM experiment. Agreement between the experimental and the theoretical data demonstrates that the calculated transmission spectra

properly depict the transmission states involved in the transport process of these molecular junctions.

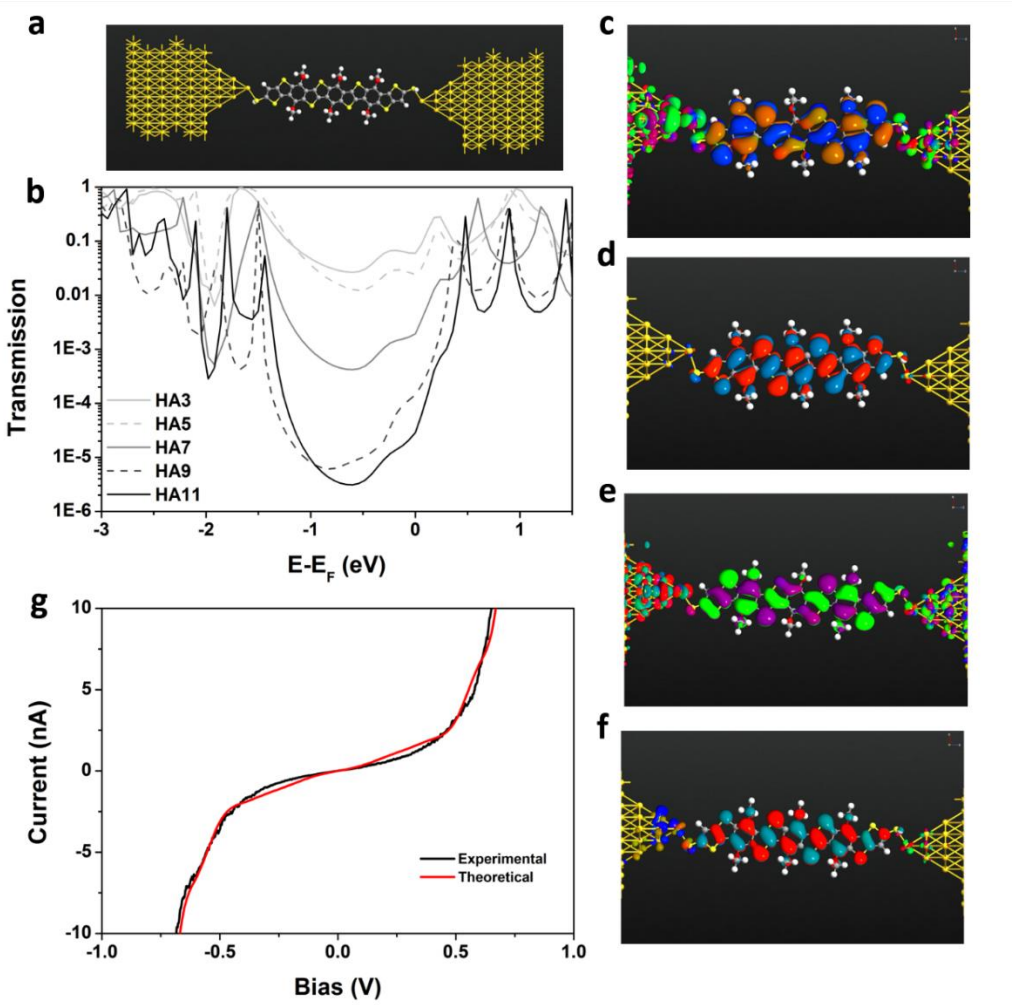

Figure 5.8 Transmission Spectra and Eigenstates Calculations. (a) Example junction geometry of HA11 after optimization used in the calculations of the transmission spectra. (b) Low bias transmission spectra of the five molecular junctions. Geometries of the transmission eigenstates for HA9 that correspond to (c) HOMO-1 and (d) HOMO, and for HA11 that correspond to (e) HOMO-1 and (f) HOMO. (g) Comparison between Experimental and Theoretical I-V Curves. The experimental I-V curve is an average of 25 individual curves of the HA11 junction. The theoretical calculation agrees well with the experimental data.

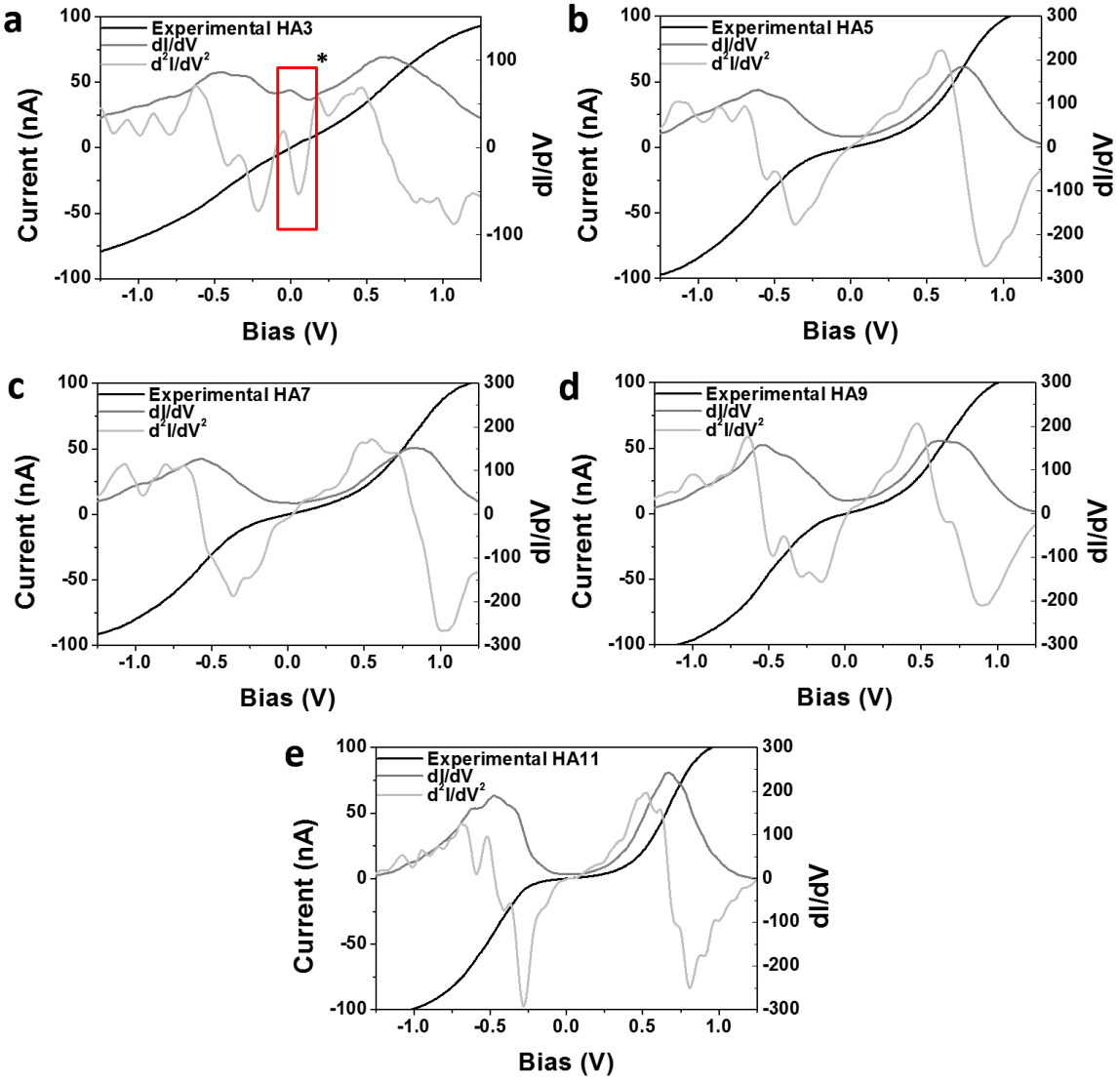

Figure 5.9 Average I-V curves, dI/dV and d^2I/dV^2 spectra of HA3 to HA11 (a to e). Average I-V curves are constructed from ca. 500 individual curves. *The peaks observed in the red box are artifacts originated from the disconnected data in the I-V curves and should not be interpreted as part of the junction transport property.

5.3 Conclusion

In summary, we have designed and synthesized a new series of ladder-type fused heteroacene molecular wires with varying lengths. The fused ring structure prevents possible conformation

change as discussed by other studies, allowing a more defined structure in the molecular core for charge transport. The length dependent decay constant β was found to be 0.088±0.007 $Å^{-1}$ under low bias and 0.047±0.009 $Å^{-1}$ under 0.5 V. These β values are significantly lower comparing with oligothiophene, resulting in reduced loss in conductance over long distance. TVS analysis indicates that energy offsets decrease as the molecule lengths increase due to extended conjugation.

5.4 Experimental Section

Synthesis of the molecular wires

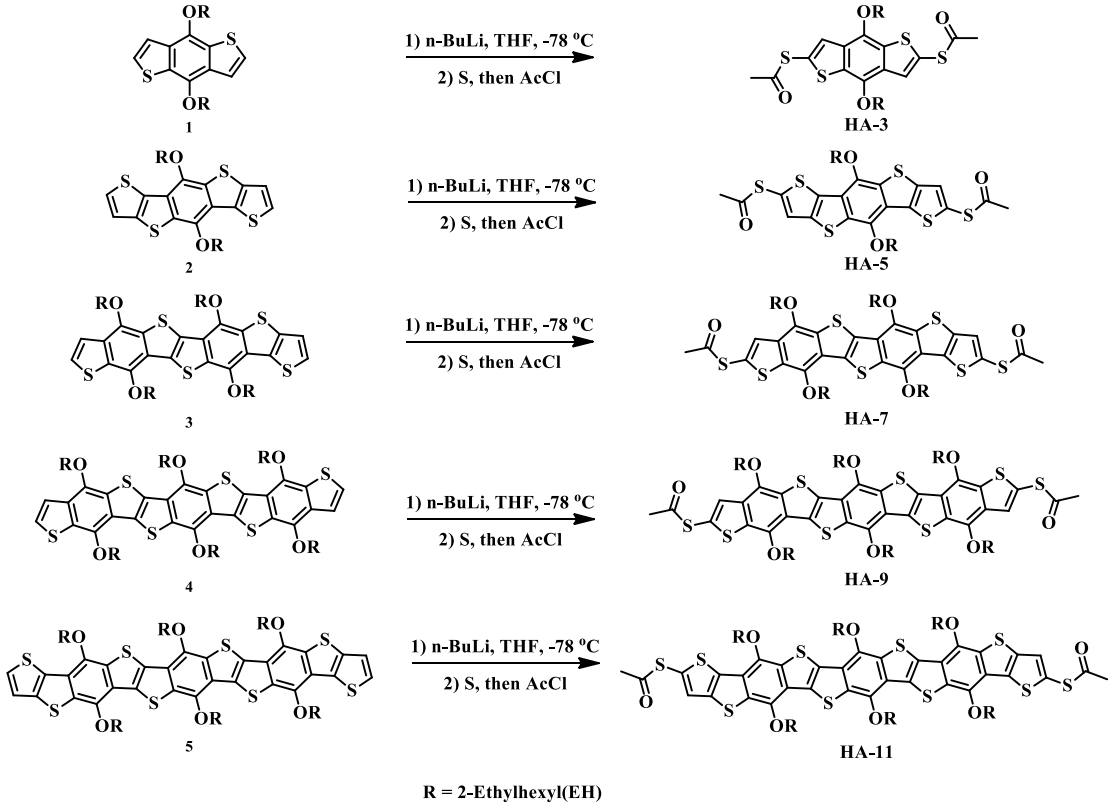

Scheme 5.1 Synthetic route of the ladder-type molecular wires

All of the chemicals were purchased from Aldrich except for tetrakis(triphenylphosphine)palladium from Strem Chemicals. All reagents purchased commercially were used without further purification except for toluene and tetrahydrofuran (THF), which were dried over sodium/benzophenone. ^{1}H NMR and ^{13}C NMR spectra were recorded on a Bruker DRX-400 spectrometer or Bruker DRX-500, with tetramethylsilane as an internal reference. Matrix-assisted laser desorption ionization time-of-flight (MALDI-TOF) mass spectra were recorded using a Bruker Ultraflextreme MALDI-TOF/TOF mass spectrometer with dithranol as the matrix. Compounds **1-4**[1], **5**[2] were prepared by our previous work.

Heteroacene(HA)-3: Benzodithiophene (**1**) (400 mg, 0.90 mmol, 1.0 equiv) was dissolved in dry THF (25 mL), and the solution was cooled to −78 °C. n-BuLi (2.5 M in hexanes, 0.79 mL, 1.97 mmol, 2.2 equiv) was added dropwise via a syringe, and the reaction was allowed to stir at −78 °C for 30 min, and 0 °C for 1 h. Dry sulfur (86 mg, 2.68 mmol, 3.0 equiv) powder was added in one portion, and the reaction was stirred at 0 °C for another hour, before AcCl (200 μL, 2.68 mmol, 3.0 equiv) was added via a syringe. The reaction was allowed to warm to RT and stirred overnight (15 h), before pouring into water (50 mL). The aqueous layer was extracted with Et_2O (30 mL × 2), and the combined organic layers were washed with brine (10 mL), dried over $MgSO_4$, filtered, and concentrated to provide yellow solid. Purification by flash chromatography with a gradient of 1:1 hexane: CH_2Cl_2 provided **HA-3** as a pale yellow solid (282 mg, 52.9 % yield). ^{1}H NMR ($CDCl_3$, ppm): δ 7.54 (s, 2H), 4.16 (q, 4H), 2.47 (s, 6H), 1.76 (m, 2H), 1.63 (m, 2H), 1.52-1.36 (m, 14H), 0.99 (t, 6H), 0.92 (t, 6H). ^{13}C NMR ($CDCl_3$, ppm): δ 192.9, 144.2, 132.3, 131.6, 128.8, 127.4, 40.6, 30.4, 29.9, 29.1, 23.8, 23.1, 14.1, 11.3. MS (MALDI-TOF/) m/z: $C_{30}H_{42}O_4S_4$, Calcd, 594.2. Found, (M^+), 594.1.

Heteroacene(HA)-5. This was prepared following the general procedure given for the preparation of **HA-3**. From **2** (80 mg, 0.14 mmol) there was obtained **HA-5** as yellow solid (52 mg, 51.4 % yield). ^{1}H NMR ($CDCl_3$, ppm): δ 7.37 (s, 2H), 4.20 (d, 4H), 2.44 (s, 6H), 1.99 (m, 2H), 1.69 (m, 2H), 1.61-1.59 (m, 6H), 1.40 (m, 8H), 1.02 (t, 6H), 0.91 (t, 6H). ^{13}C NMR ($CDCl_3$, ppm): δ 193.9, 144.1, 136.9, 136.8, 131.0, 128.9, 128.6, 125.7, 40.7, 30.2, 29.7, 29.1, 23.7, 23.1, 14.1, 11.2. MS (MALDI-TOF/) m/z: $C_{34}H_{42}O_4S_6$, Calcd,706.1. Found, (M^+), 706.0.

Heteroacene(HA)-7. This was prepared following the general procedure given for the preparation of **HA-3**. From **3** (126 mg, 0.14 mmol) there was obtained **HA-7** as yellow solid (42 mg, 28.7 % yield). ^{1}H NMR ($CDCl_3$, ppm): δ 7.59 (s, 1H), 7.41, (s, 1H), 4.27 (m, 8H), 2.49 (s, 3H), 2.47 (s, 3H), 2.08 (m, 2H), 1.77 (m, 4H), 1.64 (m, 8H), 1.40 (m, 18H), 1.24 (m, 4H), 1.05 (m, 12H), 0.93 (m, 12H). ^{13}C NMR ($CDCl_3$, ppm): δ 194.0, 193.1, 145.2, 144.3, 144.3, 143.4, 137.0, 136.8, 132.7, 132.0, 131.7, 131.3, 130.7, 130.2, 129.1, 128.7, 128.7, 126.7, 126.2, 125.6, 125.4, 40.8, 40.7, 30.4, 30.3, 30.0, 29.7, 29.2, 23.8, 23.7, 23.1, 14.1, 11.3, 11.2. MS (MALDI-TOF/) m/z: $C_{56}H_{76}O_6S_7$, Calcd, 1068.4. Found, (M^+), 1068.4.

Heteroacene(HA)-9. This was prepared following the general procedure given for the preparation of **HA-3**. From **4** (190 mg, 0.15 mmol) there was obtained **HA-9** as light orange solid (145 mg, 68.4 % yield). ^{1}H NMR (CD_2Cl_2, ppm): δ 7.53 (s, 2H), 4.32 (d, 4H), 4.26 (d, 4H), 4.20 (d, 4H), 2.42 (s, 6H), 2.12 (m, 2H), 2.08 (m, 2H), 1.70-1.35 (m, 50H), 1.05 (m, 18H), 0.92 (m, 18H). ^{13}C NMR (CD_2Cl_2, ppm): δ 192.9, 145.2, 144.4, 143.3, 132.7, 131.8, 131.6, 130.8, 130.0, 129.0, 127.0, 125.8, 125.2, 40.8, 40.8, 30.4, 30.4, 30.3, 30.0, 29.8, 29.3, 29.3, 23.8, 23.8, 23.7, 23.2, 23.2, 23.2, 14.0, 14.0, 11.2, 11.2, 11.1, 11.1, 11.0, 11.0. MS (MALDI-TOF/) m/z: $C_{78}H_{110}O_8S_8$, Calcd, 1430.6. Found, (M^+), 1430.5.

Heteroacene(HA)-11. This was prepared following the general procedure given for the preparation of **HA-3**. From **5** (30 mg, 0.02 mmol) there was obtained **HA-11** as orange solid (13.2 mg, 39.8 % yield). ^{1}H NMR ($CDCl_3$, ppm): δ 7.39 (s, 2H), 4.35 (d, 4H), 4.32 (d, 4H), 4.27 (d, 4H), 2.46 (s, 6H), 2.07 (m, 6H), 1.80 (m, 6H), 1.70-1.58 (m, 38H), 1.23 (m, 4H), 1.06 (m, 18H), 0.93 (m, 18H). ^{13}C NMR ($CDCl_3$, ppm): δ 194.0, 144.4, 143.3, 137.0, 138.8, 132.1, 132.0, 131.2, 130.9, 130.5, 130.2, 128.8, 128.7, 126.2, 125.9, 125.4, 40.8, 40.8, 30.4, 30.4, 30.3, 29.7, 29.7, 29.3, 29.3, 29.2, 29.2, 23.8, 23.2, 23.2, 14.2, 14.2, 14.2, 11.2, 11.2. MS (MALDI-TOF/) m/z: $C_{142}H_{110}O_8S_{10}$, Calcd, 1542.5. Found, (M+H), 1543.8.

Synthesis and Characterization: The synthesis of all the heteroacene compounds were shown in Scheme 5.1. The synthesis started from compounds **1-5**, which was prepared according to our reported procedures. Thiol group was introduced into the heteroacenes, respectively, by a general method. Treatment of **1-5** with n-butyl lithium at -78 °C, followed by the addition of dry sulfur powder led to thiol groups. Finally, AcCl was added to protect thiol groups afforded yellow or orange solids heteroacenes (**HA-3, 5, 7, 9** and **11**), respectively, after purification. The chemical structures of **HA-3, 5, 7, 9** and **11** were characterized with NMR and MS data.

Surface characterizations (XPS and CV):

X-ray photoelectron spectroscopy (XPS) was performed on the Thermo Scientific ESCALab 250Xi using 200 W monochromated Al Kα radiation. The 500 μm X-ray spot was used for XPS analysis. The base pressure in the analysis chamber was about 3×10^{-10} mbar. Typically, the hydrocarbon C1s line at 284.8 eV from adventitious carbon is used for energy referencing.

Surface coverage of the molecule on the gold substrate were determined from the voltammograms recorded according to the equation:

$$\Gamma = \frac{Q_{Fe}}{nFAr}$$

where Q_{Fe} is the charge consumed for the oxidation-reduction process of the ferrocene groups, n is the number of electrons involved in the electron transfer process (n = 1 for ferrocene), A is the geometric surface area of the electrode (0.6362 cm^2), r is the scan rate, and F is the faraday constant. Values of Q_{Fe} were obtained by the integration of the faradaic current peaks from the voltammograms.

Preparation of self-assembled monolayers (SAMs). Prior to each experiment, the substrate was briefly annealed in a propane flame. The self-assembled monolayers (SAMs) of the five molecules were prepared in a single step using ammonium hydroxide (28% NH_3 in H_2O) as the deprotecting agent under a N_2 protected environment in a tetrahydrofuran (THF) solution containing ca. 5×10^{-5} M of the target molecule. A gold substrate was immersed in the solution for 12 hours. The substrate was then washed successively with THF and ethanol, dried under a stream of N_2, and immediately used for experiment.

Break-junction experiment for single molecule junctions. The STM-BJ experiments were conducted with a published modified STM break-junction setup. Fresh gold tips were prepared by mechanically cutting a 0.25 mm diameter gold wire (99.998% Alfa Aesar). The experiments were carried out in degassed mesitylene (≥99.9% Sigma-Aldrich). The STM Teflon solvent holder was sonicated in acetone and dried with N_2 before use. During measurement, the solvent holder was secured above the gold–SAM surface and filled with a couple drops of mesitylene. A typical break-

junction experiment consisted of ca. 2000 current–distance traces. Of these traces, ~ 50% displayed the conductance plateaus signifying the formation of a molecular junction and were used for the construction of the histograms. The break-junction experiments were conducted at a bias of 100 mV.

***I-V* recording for single molecule junctions.** The *I-V* recording experiments were carried out at 100 mV of bias voltage in mesitylene. The entire process consists of iterations of three steps, tapping, conductance step detection and *I-V* recording, which is in contrast to the single-step tapping procedure used in the STM break junction measurements. In the tapping step, the tip is moved towards the substrate until the current reaches a preset threshold, and then is retracted until it reaches a lower preset current. In the present method, the conductance step detection is applied during each retraction cycle to identify conductance steps. The measured conductance range was selected according to the previously measured conductance histogram of each molecule. Once a conductance step is detected, the *I-V* recording step is activated, which involves the following sub-steps: 1) The tip is immediately held in position, 2) the current -voltage curve was recorded from + 1.8 V to – 1.8 V quickly (10 Hz), 3) upon completion of the *I-V* curve, the tip was pulled away from the substrate until the current drop to a preset value, and the measurement started over again.

Theoretical calculations:

Electron transport calculations for HA3 to HA11 were performed with the non-equilibrium Green's function-density functional theory method via the Atomistix Toolkit (ATK) package. Self-consistent calculations were performed using a double-ξ polarized basis set except for the gold atoms in the electrodes for which a single-ξ polarized basis set was used. Exchange correlation was treated using the local spin density approximation and all atoms were relaxed such that the

force per atom was less than 0.05 eV/Å. K-point samplings of 3 x 3 x 50 was employed for all junction calculations with 50 being on the direction along transport.

The geometries of molecules were optimized, and their orbital energies and charge distributions calculated using the B3LYP DFT function with basis set 6-31G** as implemented in Gaussian 09.

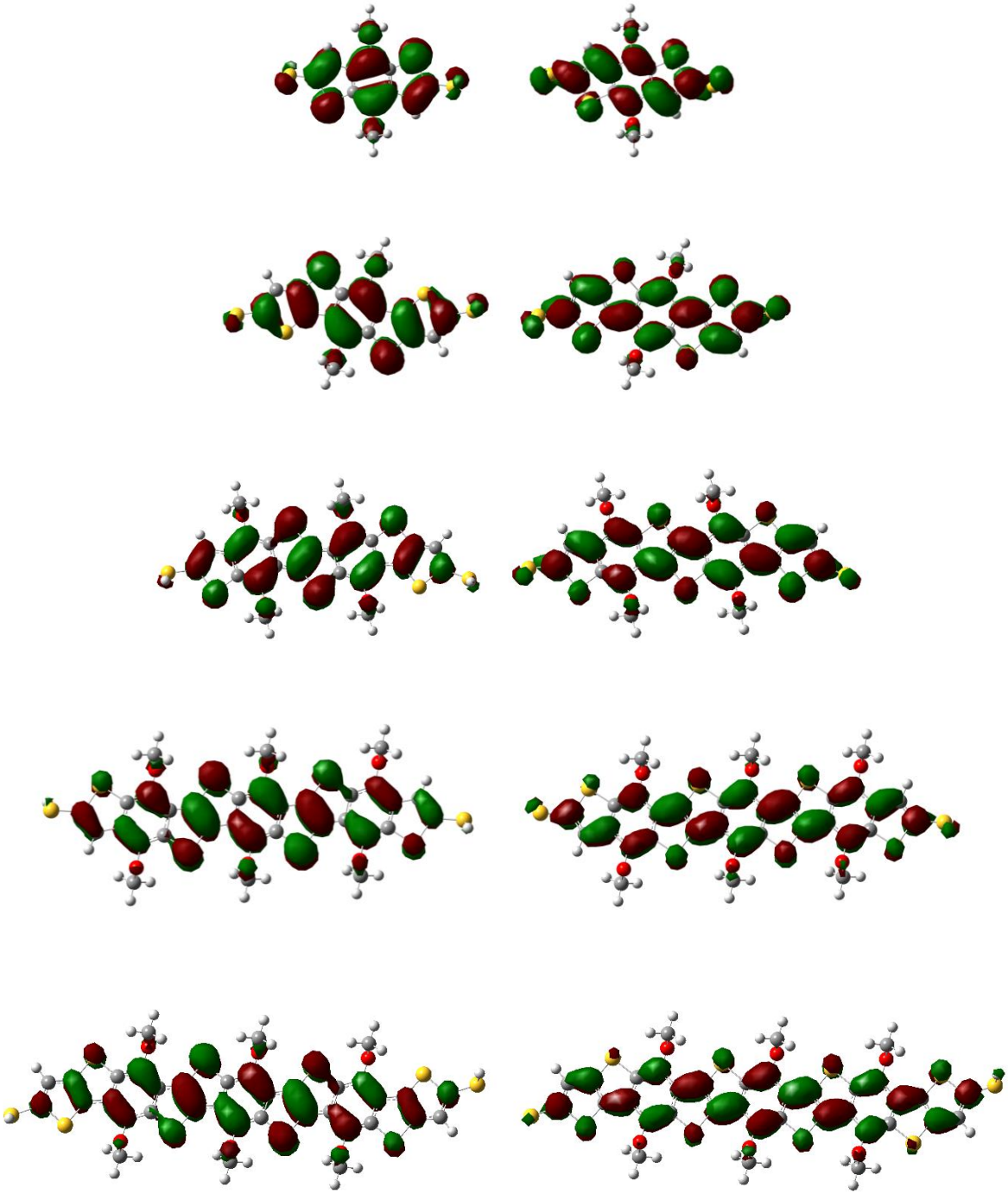

Figure 5.10 Geometries of the frontier molecular orbitals of HA3 to HA11 (top to bottom, HOMO left, LUMO right).

5.5 References

(1) Aviram, A.; Ratner, M. A. *Chem. Phys. Lett.* **1974**, *29*, 277-283.
(2) Nitzan, A. *Annu. Rev. Phys. Chem.* **2001**, *52*, 681-750.
(3) Ng, M.; Lee, D.; Yu, L. *J. Am. Chem. Soc.* **2002**, *124*, 11862-11863.
(4) Lo, W.-Y.; Bi, W.; Li, L.; Jung, I. H.; Yu, L. *Nano Lett* **2015**, *15*, 958-962.
(5) Simmons, J. G. *J. Appl. Phys.* **1963**, *34*, 1793-1803.
(6) Metzger, R. M. *Chem. Rev.* **2015**, *115*, 5056-5115.
(7) Zhang, L.; Colella, N. S.; Cherniawski, B. P.; Mannsfeld, S. C. B.; Briseno, A. L. *ACS Appl. Mater. Interfaces* **2014**, *6*, 5327-5343.
(8) Yamada, R.; Kumazawa, H.; Noutoshi, T.; Tanaka, S.; Tada, H. *Nano Lett* **2008**, *8*, 1237-1240.
(9) Leary, E.; Hobenreich, H.; Higgins, S. J.; van Zalinge, H.; Haiss, W.; Nichols, R. J.; Finch, C. M.; Grace, I.; Lambert, C. J.; McGrath, R.; Smerdon, J. *Phys. Rev. Lett.* **2009**, *102*, 086801.
(10) Lörtscher, E.; Gotsmann, B.; Lee, Y.; Yu, L.; Rettner, C.; Riel, H. *ACS Nano* **2012**, *6*, 4931-4939.
(11) Ie, Y.; Endou, M.; Lee, S. K.; Yamada, R.; Tada, H.; Aso, Y. *Angew. Chem., Int. Ed.* **2011**, *50*, 11980-11984.
(12) Zhitenev, N. B.; Meng, H.; Bao, Z. *Phys. Rev. Lett.* **2002**, *88*, 226801.
(13) Xu, B. Q.; Li, X. L.; Xiao, X. Y.; Sakaguchi, H.; Tao, N. J. *Nano Lett* **2005**, *5*, 1491-1495.
(14) Capozzi, B.; Dell, E. J.; Berkelbach, T. C.; Reichman, D. R.; Venkataraman, L.; Campos, L. M. *J. Am. Chem. Soc.* **2014**, *136*, 10486-10492.
(15) Xiang, L.; Hines, T.; Palma, J. L.; Lu, X.; Mujica, V.; Ratner, M. A.; Zhou, G.; Tao, N. *J. Am. Chem. Soc.* **2016**, *138*, 679-687.
(16) Zheng, T.; Lu, L.; Jackson, N. E.; Lou, S. J.; Chen, L. X.; Yu, L. *Macromolecules* **2014**, *47*, 6252-6259.
(17) Zheng, T.; Cai, Z.; Ho-Wu, R.; Yau, S. H.; Shaparov, V.; GoodsonIII, T.; Yu, L. *J. Am. Chem. Soc.* **2016**, *138*, 868-875.
(18) Love, J. C.; Estroff, L. A.; Kriebel, J. K.; Nuzzo, R. G.; Whitesides, G. M. *Chem. Rev.* **2005**, *105*, 1103-1169.
(19) Díez-Pérez, I.; Hihath, J.; Lee, Y.; Yu, L.; Adamska, L.; Kozhushner, M. A.; Oleynik, I. I.; Tao, N. *Nat. Chem.* **2009**, *1*, 635-641.
(20) Xu, B.; Tao, N. J. *Science* **2003**, *301*, 1221-1223.
(21) Guo, S. Y.; Hihath, J.; Diez-Perez, I.; Tao, N. J. *J. Am. Chem. Soc.* **2011**, *133*, 19189-19197.
(22) Su, T. A.; Neupane, M.; Steigerwald, M. L.; Venkataraman, L.; Nuckolls, C. *Nat. Rev. Mats.* **2016**, *1*, 1-15.
(23) Beebe, J. M.; Kim, B.; Gadzuk, J. W.; Daniel Frisbie, C.; Kushmerick, J. G. *Phys. Rev. Lett.* **2006**, *97*, 026801.
(24) Huisman, E. H.; Guédon, C. M.; van Wees, B. J.; van der Molen, S. J. *Nano Lett* **2009**, *9*, 3909-3913.
(25) Stern, T. E.; Gossling, B. S.; Fowler, R. H. *Proc. R. Soc. Lon. Ser-A.* **1929**, *124*, 699-723.
(26) Guo, S.; Zhou, G.; Tao, N. *Nano Lett* **2013**, *13*, 4326-4332.
(27) Xie, Z.; Bâldea, I.; Smith, C. E.; Wu, Y.; Frisbie, C. D. *ACS Nano* **2015**, *9*, 8022-8036.
(28) Muscat, J. P.; Newns, D. M. *Prog. Surf. Sci.* **1978**, *9*, 1-43.
(29) Schmickler, W. *J. Electroanal. Chem.* **1986**, *204*, 31-43.

(30) Bâldea, I. *Phys. Rev. B* **2012**, *85*, 035442.
(31) Bâldea, I. *Chem. Phys.* **2012**, *400*, 65-71.
(32) Chen, J.; Markussen, T.; Thygesen, K. S. *Phys. Rev. B* **2010**, *82*, 121412.
(33) Mirjani, F.; Thijssen, J. M.; van der Molen, S. J. *Phys. Rev. B* **2011**, *84*, 115402.
(34) Liang, G. C.; Ghosh, A. W.; Paulsson, M.; Datta, S. *Phys. Rev. B* **2004**, *69*, 115302.
(35) Liu, R.; Ke, S. H.; Yang, W.; Baranger, H. U. *J. Chem. Phys.* **2006**, *124*, 024718.